THE EUROPEAN
PHYSICAL JOURNAL A

PUMA, antiProton unstable matter annihilation

T. Aumann[15], W. Bartmann[3], O. Boine-Frankenheim[16], A. Bouvard[3], A. Broche[3], F. Butin[3], D. Calvet[2],
J. Carbonell[14], P. Chiggiato[3], H. De Gersem[16], R. De Oliveira[3], T. Dobers[3], F. Ehm[3], J. Ferreira Somoza[3],
J. Fischer[15], M. Fraser[3], E. Friedrich[15], A. Frotscher[15], M. Gomez-Ramos[15], J.-L. Grenard[3], A. Hobl[1], G. Hupin[14],
A. Husson[15], P. Indelicato[8], K. Johnston[3], C. Klink[15], Y. Kubota[15], R. Lazauskas[5], S. Malbrunot-Ettenauer[3,17],
N. Marsic[16], W. F. O Müller[16], S. Naimi[11], N. Nakatsuka[15], R. Necca[3], D. Neidherr[4], G. Neyens[5,7], A. Obertelli[15,a],
Y. Ono[12], S. Pasinelli[3], N. Paul[8], E. C. Pollacco[2], D. Rossi[15], H. Scheit[15], M. Schlaich[15], A. Schmidt[15],
L. Schweikhard[13], R. Seki[10], S. Sels[3,7], E. Siesling[3], T. Uesaka[11], M. Vilén[3], M. Wada[6], F. Wienholtz[15], S. Wycech[9],
S. Zacarias[15]

[1] Bilfinger Noell GmbH, Würzburg, Germany
[2] CEA, IRFU, Gif-sur-Yvette, France
[3] CERN, Meyrin, Switzerland
[4] GSI Helmholtzzentrum für Schwerionenforschung GmbH, Darmstadt, Germany
[5] Institut Pluridisciplinaire Hubert Curien, CNRS/IN2P3, Université Louis Pasteur, Strasbourg, France
[6] KEK, Tsukuba, Japan
[7] Instituut voor Kern- en Stralingsfysica, KU Leuven, Leuven, Belgium
[8] Laboratoire Kastler Brossel, Sorbonne Université, CNRS, ENS-PSL Research University, Collège de France, Paris, France
[9] National Centre for Nuclear Research, Otwock, Poland
[10] RCNP, Osaka, Japan
[11] RIKEN Nishina Center, Saitama, Japan
[12] The Open University of Japan, Chiba, Japan
[13] Université Paris-Saclay, CNRS/IN2P3, IJCLab, 91405 Orsay, France
[14] University of Greifswald, Greifswald, Germany
[15] Technische Universität Darmstadt, IKP, Darmstadt, Germany
[16] Technische Universität Darmstadt, TEMF, Darmstadt, Germany
[17] TRIUMF, Vancouver, Canada

Abstract PUMA, antiProton Unstable Matter Annihilation, is a nuclear-physics experiment at CERN aiming at probing the surface properties of stable and rare isotopes by use of low-energy antiprotons. Low-energy antiprotons offer a very unique sensitivity to the neutron and proton densities at the annihilation site, i.e. in the tail of the nuclear density. Today, no facility provides a collider of low-energy radioactive ions and low-energy antiprotons: while not being a collider experiment, PUMA aims at transporting one billion antiprotons from ELENA, the Extra-Low-ENergy Antiproton ring, to ISOLDE, the rare-isotope beam facility of CERN. PUMA will enable the capture of low-energy antiprotons by short-lived nuclei and the measurement of the emitted radiations. In this way, PUMA will give access to the so-far largely unexplored isospin composition of the nuclear-radial-density tail of radioactive nuclei. The motivations, concept and current status of the PUMA experiment are presented.

[a] e-mail: aobertelli@ikp.tu-darmstadt.de

1 Introduction

The occurrence of neutron halos was discovered in light-mass nuclei at the limit of nuclear existence, i.e. at the neutron drip line [1]. Historically ^{11}Li was the first halo nucleus discovered[1], whose structure is understood as a ^{9}Li core surrounded by two neutrons with a large radial extension. Halos are a truly fascinating manifestation of quantum physics. They belong to a subset of clustering [4] for which the probability region of the halo neutrons ranges into a region of space that is classically forbidden. In other words, the neutrons are found well beyond the range of the neutron-core potential [5–9] and owe their existence to genuine quantum effects. Their properties show universal aspects of few-body systems such as scaling laws [10,11], i.e. they do not encode details of the strong force. This makes atomic nuclei, and more particularly exotic neutron-rich systems, a unique laboratory to study universal few-body phenomena. That said, universal features do not prevent physicists from reaching a true understanding of nuclear halos. This requires both a precise description of nuclear correlations and an accurate accounting of large-distance behavior. Thus, this coincides with one of the greatest challenges of contemporary physics: the treatment of multiple scales. While nuclear modeling efforts are being deployed in this direction, our understanding will only improve by challenging theory with a more complete representation of halo systems from new experimental probes.

Several halos have been identified and characterized from complementary observables, when possible, such as reaction cross sections, neutron transfer, charge and matter radii, elastic and inelastic scattering, Coulomb excitation, delayed beta decay and femtoscopy measurements [12,13]. An overview of the so-far observed (or claimed) halo nuclei is given in Fig. 1. Today, only light halo nuclei up to mass number A = 8 (^{8}He) can be calculated via ab initio techniques where the Schrödinger equation is solved in full with realistic nucleon-nucleon interactions. While only s-wave halos have been observed so far, p-wave neutron halos have also been claimed to appear in very neutron-rich Ne and Mg isotopes from breakup cross section measurements [14,15]. A more direct measurement is needed to confirm the latter conclusions. Although the existence of single-particle halos requires a small centrifugal barrier, their s or p wave dominance might not be a prerequisite as believed so far: a recent study of ^{17}B [16] showed a large d wave component in the halo, and estimated the s-wave contribution to less than 10%.

Fig. 1 Low-mass region of the nuclear chart. Isotopes marked with a circle correspond to nuclei which show indications of a proton or a neutron halo. While few of the highlighted nuclei have been extensively studied, several of them have been claimed to be halo candidates based on limited experimental evidence

Fig. 2 Theoretical matter, proton, and neutron density distributions for the ground state for ^{17}Ne. The Fermionic Molecular Dynamics (FMD) approach reproduces well the large charge radius of ^{17}Ne, whose description is consistent with a two-proton halo bound to a ^{15}O core. Figure reprinted with permission from Ref. [20] ©2021 by the American Physical Society

Proton halos are expected to exist and some candidates have been explored experimentally. On the other hand, the protons of the core induce a Coulomb barrier for the proton halo. The tail of the halo wave function is then expected to be suppressed at larger distances, making the halo formation more difficult and preventing it altogether for nuclear charges above Z∼10–20. The most prominent cases are the one-proton halo ^{8}B [17–19] and the two-proton halo ^{17}Ne [20,21]. Theoretical proton and neutron radial densities ρ for ^{17}Ne are shown in Fig. 2.

For medium-mass nuclei, the appearance of halos is predicted by several effective models with outcomes varying from one to another [22–26]. As an illustration, predictions from [22] of neutron halos in medium-mass neutron-rich nuclei quantified through a halo factor N_{halo} are shown in Fig. 3. N_{halo} is defined as the amount of neutrons in a nucleus where the one-body matter density of the core nucleus, composed of A-1 nucleons, is less than 10% of the halo density, following the definition $N_{halo} = \int_{r_0}^{\infty} \rho(r)r^2 dr$ where r_0

---

[1] The simplest case of halo is the deuteron, a stable binary halo, which exhibits a large central depletion and an anomalously large radius. The term *halo* was first used to qualify the excess of neutrons at the nuclear surface, now addressed as the *neutron skin* (see e.g. [2]). It was also employed to characterise the composition of the nuclear surface from low-energy antiprotons by Bugg et al. [3].
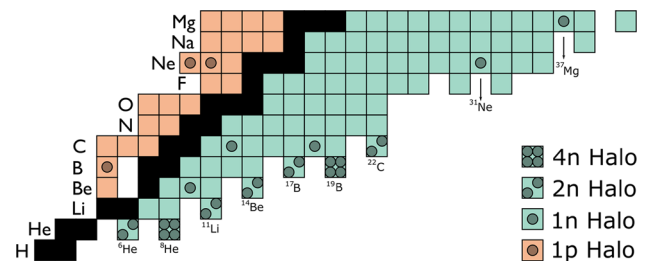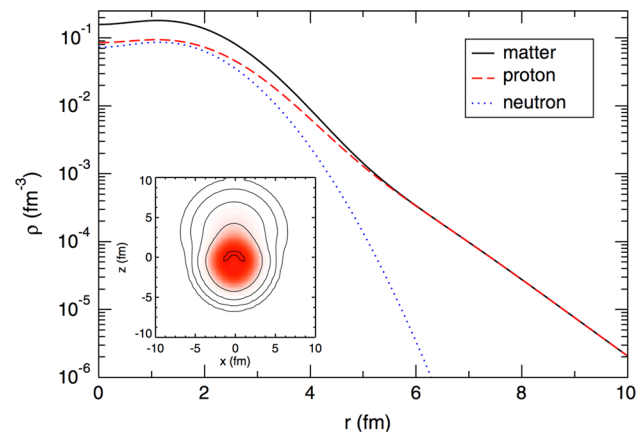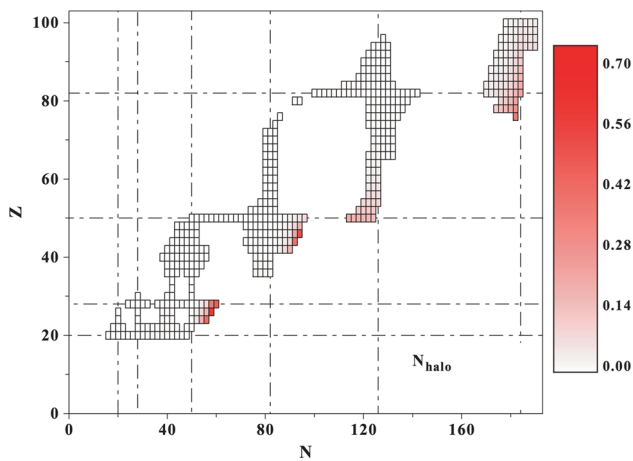
Fig. 3 Halo factor N_{halo} characterizing the amount of neutron halo in medium-mass neutron-rich nuclei (see text). Calculations were performed at the mean-field level in the Hartree-Fock-Bogolyubov framework with the Sly4 effective interaction. Figure preprinted with permission from [22] ©2021 by the American Physical Society

Fig. 4 Neutron-skin thickness Δr_{np} calculated for tin isotopes with twenty-three different Skyrme interactions. Figure reprinted with permission from Ref. [38] ©2021 by the American Physical Society

is the radius of the core. Calculations were performed for spherical nuclei, near shell closures, with the Sly4 Skyrme effective nucleon-nucleon interaction [27].

Except for a few works within the Nilsson-model framework [28–30], the role of deformation has been barely studied so far and no data support in a firm way the existence of deformed halos.

A large neutron excess at the nuclear surface is not necessarily a halo and can take the form of a neutron skin. Neutron skins, corresponding to a neutron density higher than the proton density at the surface of the nucleus, have been evidenced in stable nuclei. Neutron skins are so far mostly quantified via their thickness defined as the difference between the neutron and proton distribution rms radius

$$\Delta r_{np} = \langle r_n^2 \rangle^{1/2} - \langle r_p^2 \rangle^{1/2}. \tag{1}$$

Thick neutron skins, i.e. thicker than $\sim$0.3 fm, were observed in light neutron-rich nuclei. Microscopic models predict the development of thick neutron skins in very neutron-rich medium-mass nuclei [31–39] but no experimental evidence exists so far. An illustration of the spread of predictions by using different Skyrme nucleon-nucleon functionals is shown in Fig. 4. Such thick neutron skins would represent a unique occurrence of low-density pure neutron matter in the laboratory. Using all experimental techniques presently available, it has not yet been possible to determine the neutron skin accurately enough in order to discern the best microscopic theories for proton and neutron distributions. Characterizing the evolution of the neutron skin along isotopic chains towards large neutron excess will represent a new constraint for nuclear structure theories.
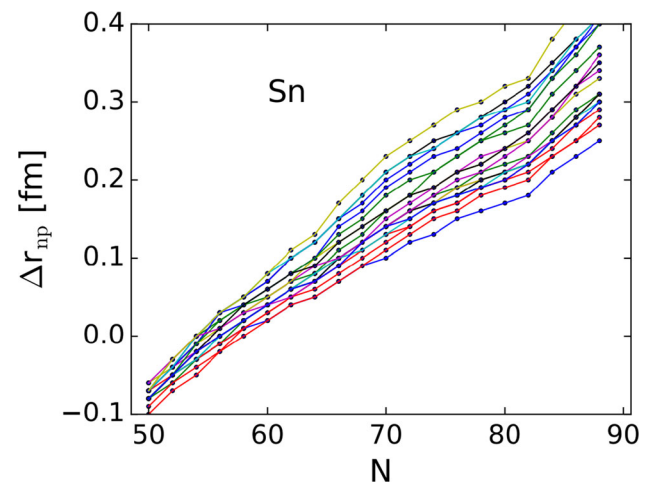
In addition to the many-body problem, the study of neutron skins has been motivated by the nuclear equation of state, a driving component of the structure of neutron stars. In heavy stable nuclei, the difference between the neutron and proton radii is of the order of a few percent [40]. The determination of the neutron skin thickness is indeed precious to learn about the equation of state at low density ($\rho < \rho_0$), to give information on the isospin dependence of the nuclear force and to constrain our description of neutron stars [41,42]. The larger the pressure of neutron matter, the thicker is the skin as neutrons are pushed out against surface tension. The same nuclear pressure supports neutron stars against gravity, therefore correlations between neutron skins of neutron-rich nuclei and various neutron star properties are naturally expected. The density dependent symmetry term $\varepsilon(\rho)$ of the equation of state gives the cost in energy to separate neutrons and protons. A strong correlation between the so-called slope coefficient of the symmetry energy $L = 3\rho_0 \partial\varepsilon/\partial\rho|_{\rho_0}$ and the neutron-skin thickness has already been shown [35] and is illustrated in Fig. 5. According to this correlation, one can constrain the symmetry-energy term of the equation of state. The recent parity-violation electron scattering measurement on ^{208}Pb from the PREX2 experiment at Jlab gives a neutron skin thickness of 0.283(0.071) fm [43], leading to conclusions on the nuclear equation of state at tension with previous works [44]. Neutrino-nucleus scattering measurements are expected to also give valuable information on the matter radius [45,46]. In addition, the magnitude of neutron skins gives insight into the nature of three-body forces in nuclei, the position of nuclear drip lines, and collective nuclear excitations related to the isospin degree of freedom. The best constraint on nuclear forces would come from a systematic study of neutron skins along isotopic chains and for very neutron-rich systems.

The nature of neutron skins in nuclei may not be as simple as described by mean-field approaches. Parity-violating electron scattering analysis [40] as well as predictions from a data-constrained dispersive optical model analysis [47] favor thicker neutron skins than other *ab initio* predictions and than most microscopic predictions, as well as compared to strong-probe extracted values [48,49]. Spatial correlations including alpha clustering are predicted to take place at sub-saturation densities and therefore at the nuclear surface. It is expected that clustering and the formation of inhomogeneous matter at low densities modifies the tail of the proton density [50]. If such correlations are confirmed experimentally, it would modify our understanding of the symmetry energy of the nuclear equation of state, as compared to calculations assuming a uniform uncorrelated spatial distribution of constituents [51]. Recently, *ab initio* calculations have been extended to medium-mass nuclei (see [52] for an overview). Calculated binding energies and matter radii of stable nuclei show a systematic discrepancy compared to experiment when the coupling constants of the input two- and three-body interactions are fixed to scattering data and three-body nuclei only. These discrepancies indicate limitations of the most recent ab initio theories, i.e. they fail to grasp enough of the relevant many-body effects in the current power counting schemes of the perturbative expansion [53].

In Sect. 2, we summarize the current knowledge of the formation and decay of antiprotonic atoms and the use of resulting radiations as a probe for nuclear structure. The objectives and the current status of the PUMA main device are described in Sects. 3 and 4, respectively. The installation and optics for PUMA at ELENA and ISOLDE are introduced in Sects. 5 and 7, while details on the transportation of antiprotons from
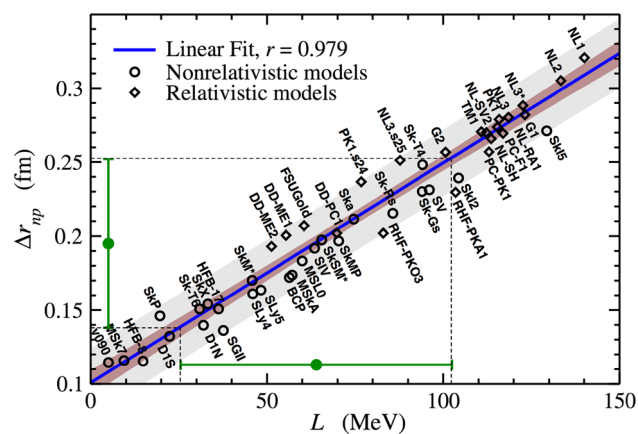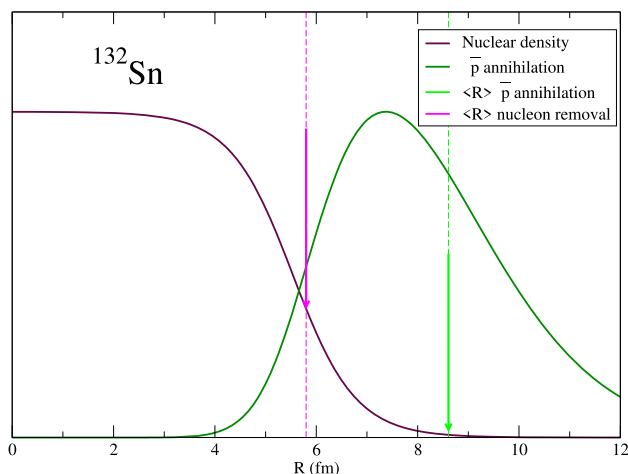

Fig. 6 Matter density distribution of ^{132}Sn (black), obtained from extrapolation of optical model. The theoretical mean radius for nucleon stripping from quasifree scattering (pink arrow) and the expected site of annihilation after antiproton capture (green arrow) are shown. For this estimate, the annihilation profile corresponding to a mixture of antiprotonic orbitals with quantum numbers ($n = 8$, $\ell = 7$) at 90% and ($n = 9$, $\ell = 7$) at 10% (green curve) is considered

ELENA to ISOLDE are given in Sect. 6. A summary and perspectives are given in Sect. 8. The material of this article is taken from the PUMA proposal to CERN [54] and from the unpublished PUMA Technical Design Report.

2 Antiprotons as a probe for nuclear structure

2.1 Previous work and context

For the above reasons, the outer part of the nuclear density in neutron-rich isotopes is of capital interest, although difficult to access experimentally. Indeed, all current techniques to investigate neutron skins and halos are sensitive to the entire density or, in the case of hadronic probes, to the nuclear surface where $\rho \sim \rho_0/2$. In the case of neutron skins and halos, the relevant region of neutron excess takes place in the *tail* of the nuclear density, i.e. beyond the surface where $\rho \sim \rho_0/2$, a region unexplored so far. The use of low-energy antiprotons as a probe should remedy this lack of experimental information, as further detailed below. As an illustration of the difference between the radial sensitivity of annihilation following antiproton capture and direct nuclear reactions such as nucleon knockout at high beam energies, we illustrate in Fig. 6 the theoretical mean radial position for both processes. While the nuclear reaction is sensitive to the surface of the nucleus, the annihilation is sensitive to its tail, where the skin and halo phenomena prevail. These studies with radioactive ions were first proposed by Wada and Yamazaki [55].

The first nuclear structure experiment with antiprotons was performed at Brookhaven National Laboratory, USA in

Fig. 5 Calculated neutron-skin thickness of ^{208}Pb against the slope L of the symmetry energy for different effective nucleon-nucleon interactions at the mean-field level. Figure reprinted with permission from [35] ©2021 by the American Physical Society

the 1970s [3]. Low-energy antiprotons were sent onto targets made of different solid materials (C, Ti, Ta, Pb) and charged pions from annihilation were measured in a bubble chamber where the targets were inserted. Since the electric charge is conserved during the annihilation process, the measurement of the ratio of positive and negative pions should be related to the annihilated neutron-to-proton ratio. Detection efficiency was considered in the analysis, as well as the difference of annihilation probability with protons and neutrons. The later correction term was estimated with ^{12}C as reference. The obtained normalised neutron-to-proton annihilation ratios show values significantly larger than N/Z for all cases, where N is the number of neutrons and Z is the number of protons. The relative excess compared to N/Z was interpreted as an excess of neutrons in the tail of the nuclear density and quantified as a so-called *halo factor*, as defined in Sect. 1. In the case of ^{208}Pb, 2.3(5) times more neutron annihilations were observed compared to what one could expect from N/Z. Since this pioneer study, antiprotons have been used to investigate the nature of the tail of the nuclear density in stable nuclei.

The initial interpretation of this first work suffered from the lack of a detailed treatment of final-state interactions, as well as the lack of theoretical understanding for the site of the annihilation. These points were partly addressed in the interpretation of later works at the Low Energy Antiproton Ring (LEAR) and the Antiproton Decelerator (AD) at CERN, where the annihilation process from nucleon- and nucleus-antiproton collisions were studied. The sensitivity of low-energy antiprotons to the nuclear density tail of nuclei was demonstrated [56], although a fully microscopic and consistent treatment of the antiproton-nucleus many-body problem still remains to be developed. The major part of nuclear structure studies with antiprotons relied on the detection of X-rays from the decay of antiprotonic atoms [57–59] and γ-rays from the residual nuclei [60,61]. Several of these works aimed at determining the neutron skin thickness of stable nuclei in a model dependent way. In contrast, PUMA aims at characterizing the tail of the nuclear density of radioactive nuclei from the measurement of low-energy-annihilation products.

As of today, no accelerator complex provides low-energy antiprotons to be used as probes for unstable nuclei. Indeed, the use of antiprotons with unstable nuclei requires two large-scale facilities, one for the antiproton production and one for radioactive-ion beams (RIB), or a way to bring antiprotons to a RIB facility. This was proposed for FAIR as the FLAIR project [62] but has not been included in the start version of FAIR. The PUMA project aims at bringing stored antiprotons from ELENA [63] to the ISOLDE facility [64,65] at CERN as illustrated in Fig. 7). Its results are expected to provide the necessary inputs to advocate for a low-energy antiproton-

Fig. 7 Itinerary of PUMA from ELENA to ISOLDE at the CERN campus

radioactive ion collider at CERN or FAIR which, in return, may open new perspectives to study nuclear systems.

The physics potential of antiprotonic atoms formed from stable and radioactive ions is larger than the above-mentioned first motivations of PUMA. Ideas about hypernuclei studies and short-range correlations are under investigation [66], while beyond the scope of the present article.

2.2 Antiprotonic atoms in a nutshell: from capture to annihilation

Antiprotonic atoms are especially suited to probe the nuclear density at the nuclear periphery, since the antiproton-nucleus annihilation is estimated to take place at about 2–2.5 fm outside the half-density radius, as deduced from the LEAR/CERN PS209 X-ray experiment [58].

The annihilation of the antiprotons is followed by meson emission, dominated by the emission of pions. The reconstruction of the total charge of the emitted pions allows for the determination of the charge of the annihilated particles, 0 in the case of antiproton-proton annihilation and -1 in the case of antiproton-neutron annihilation. Thus, the distribution of protons and neutrons in the nuclear periphery can be explored through the charge distribution of the emitted pions.

In order to obtain the neutron-to-proton annihilation ratio from the emitted pions, the whole process leading to and after antiproton annihilation must be considered. This process follows three differentiated steps:

– Capture of the antiproton by the atom in an orbital with high energy, after which the antiproton follows a decay cascade until it reaches the nuclear surface.

– Annihilation of the antiproton with one of the nucleons in the nuclear surface, resulting in the emission of mesons, mostly pions.
– Final-state interactions of the emitted pions with the nucleus, which may modify the detected pion distribution.

These steps and their current understanding are described in the following.

2.2.1 Atomic capture

Atomic capture of negatively charged mesons and baryons is known to be a non-trivial many-body process involving the long-range Coulomb interaction at low energies. Therefore it has a highly quantum-mechanical nature. Numerous works have explored the capture process, which is similar for all heavy negatively charged particles (μ, K^-, $\bar{p}$, ...), starting with the early works of Fermi and Teller [67], up to recent semiclassical [68], quantum-mechanical [69] and hybrid calculations [70]. A recent report on capture of exotic particles can be found in [71].

The capture process can be summarized as follows: an antiproton with an energy close to the ionization energy of an atom interacts strongly via Coulomb interaction with the most weakly-bound (valence) electron of the atom, resulting the ejection of the valence electron from the atom, due to the large mass difference between the electron and the antiproton. The antiproton is left in a bound state with a binding energy similar to that of the ejected electron, which corresponds to a principal quantum number of $n_c \sim n_0 = \sqrt{M^*/m_e} n_e$, where M^* is the reduced mass of the antiproton-nucleus system and n_e is the principal quantum number of the valence electron. The angular momentum of the captured antiproton l is in general assumed to follow an almost statistical distribution ($P(l) = (2l + 1)e^{\alpha l}$, $\alpha \leq 0.2$) [72]. This shows a qualitative agreement with recent theoretical calculations, as shown in the top panel of Fig. 8, which corresponds to the capture of muons by Ne.

State-of-the-art theoretical calculations [73] (shown in the bottom panel of Fig. 8) predict non-negligible capture cross sections for energies above the ionization potential of the colliding atom, the cross section increasing with the number of protons. This process can be understood as the antiproton colliding with multiple electrons before capture and losing more energy than with only one collision. Unfortunately, the dependence of the capture cross section on the collision energy has not been experimentally determined. Given the expected energies of the ion beams to be used with PUMA, the capture cross section energy dependence may introduce some uncertainties in the yields obtained. As a first approximation to address the capture cross section energy dependence, a parametrization of the results in [68] for radioactive
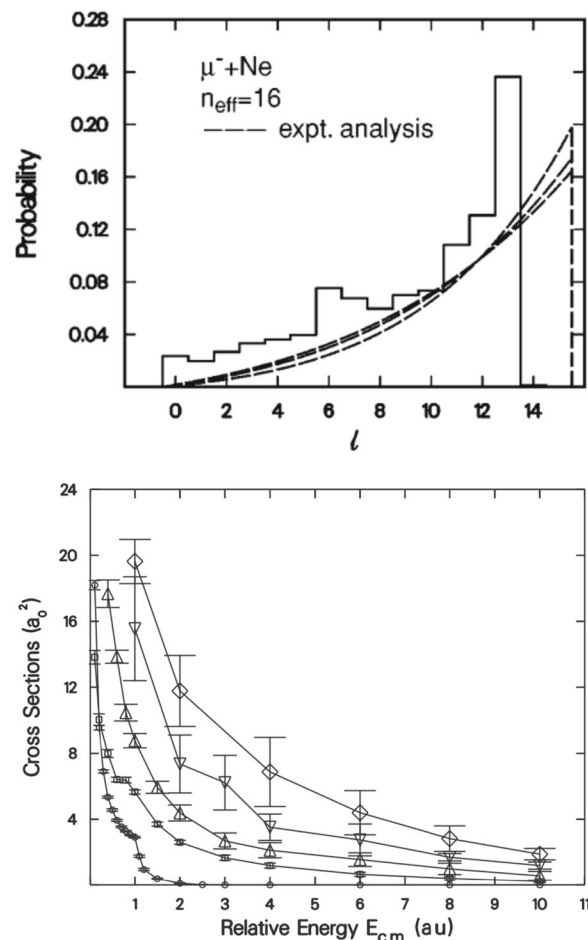
Fig. 8 (Top) $P(l)$ distribution from semiclassical calculation (bins) and phenomenological fit (dashed line). Figures reprinted with permission from [74] @2022 by the American Physical Society. (Bottom) Antiprotonic capture cross sections as function of center of mass energy for He (circles), Ne (squares), Ar (up triangles), Kr (down triangles), Xe (diamonds). Figures reprinted with permission from [73] @2022 by the American Physical Society

ions as a function of energy E and atomic number Z will be employed. This parametrized energy-dependent cross section will be convoluted with the expected energy distribution between antiprotons and ions in order to obtain the optimal energy range for the ion beams, within the limitations of the beam settings. Conversely, the yields from PUMA may provide missing experimental data about the energy dependence of the capture process in the range of 10–100 s of eV.

2.2.2 Atomic cascade through the electron cloud

After capture, the antiproton cascades to lower levels through the electron cloud by successive Auger and radiative transitions. The value of n_c at this stage is large ($n_c \sim 100$), so annihilation of the antiproton by the nucleus is negligible. Due to the large value of n_c, the most likely transitions
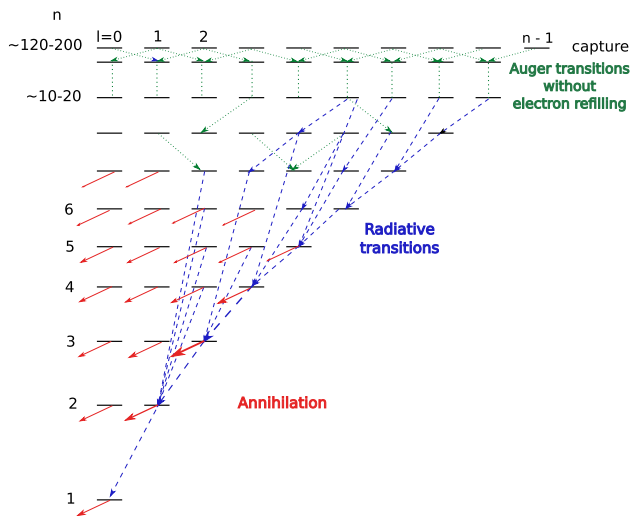
Fig. 9 Scheme of the antiprotonic decay in a light Z atom in PUMA. Figure inspired from that in [77]

$n_c \to n_c - 1$ are Auger transitions, which result in the emission of low-energy electrons, difficult to measure, so this step of the cascade is difficult to characterize experimentally, and there are extremely few experimental publications on the Auger spectra at this stage of the cascade [75].

The LEAR/CERN PS175 experiment has been able to measure the intensity of various X-ray spectra of three noble gases: Ar, Kr and Xe, in the energy region corresponding to this stage of the cascade [76]. The occurrence of Auger transitions could be observed indirectly by the variation of the intensity of the peaks, while the peaks were found to correspond to transitions between orbits embedded in the electronic cloud via comparison with multiconfiguration Dirac-Fock (MCDF) calculations.

The findings in this experiment are relevant for the PUMA project, as both consider low-density environments, where the refilling (capture of electrons from surrounding atoms and "refill" of vacancies left by ejected Auger electrons) can be neglected. Refilling is known to play an important role in the population of the different antiprotonic orbitals so experimental data in a similar electron refilling regime would set a useful benchmark for the calculations to be performed for PUMA.

2.2.3 Atomic cascade after the electron cloud

After going through the electron cloud ejecting most electrons from the atom, the antiproton continues to cascade down, through radiative transitions. Radiative transitions with $\Delta n_c > 1$ lead to an increase in population of the so called "circular states" $(n_c, l = n_c - 1)$ [77], which reduces the sensitivity to the previous distribution of states $P(n_c, l)$ populated through capture and the previous steps

of the cascade. This stage of the cascade is dominated by high-energy X-rays which can be measured very precisely, so a robust understanding of this stage has been developed, with codes able to reproduce it with significant precision [78,79]. A member of PUMA was involved in the development of [78], which was used in the analysis of the experiment LEAR/CERN PS209 [58]. For this analysis, the initial population distribution was assumed to have the quasi-statistical shape $P(n_c, l) = (2l+1)e^{\alpha l}$. n_c was taken to be 20, far from the K-shell electron orbitals. The parameter α was established to be 0.1–0.2 for the studied nuclei, with a 10% statistical uncertainty. As mentioned above, PS209 showed that antiproton annihilation explores mainly distances 2–2.5 fm beyond the nuclear surface, with a systematic difference between proton and neutron radii across the nuclear chart. A schematic of the overall cascade process is presented in Fig. 9.

Based on the previous analysis, we plan to perform cascade calculations using the recently constructed cascade code by Koike [80] together with the code [78].

We will first use the conventional local form for the antiproton-nucleus potential V_{opt} [81]:

$$2\mu V_{\text{opt}} = -4\pi \left(1 + \frac{\mu}{M} \frac{A-1}{A}\right) \times \left[b_0(\rho_n + \rho_p) + b_1(\rho_n - \rho_p)\right], \quad (2)$$

where μ is the reduced mass of antiproton and nucleus, A the nuclear mass number and M the nucleon mass. ρ_n and ρ_p are the neutron and proton densities, normalized to the neutron N and proton Z numbers respectively. The same parameters b_0 and b_1 from PS209 [58], used to study the "halo factor" [72]

$$f_{\text{halo}} = \frac{N(\bar{p}n)}{N(\bar{p}p)} \frac{Z}{N} \frac{\text{Im}(a_{\bar{p}p})}{\text{Im}(a_{\bar{p}n})}, \quad (3)$$

can be used. The first term of the right-hand-side of Eq. (3) is the ratio of annihilation events for neutrons divided by the annihilation events for protons, while the third one is the ratio of the imaginary part of the scattering lengths for antiproton-proton and antiproton-neutron interaction, corresponding to $b_0 - b_1$ and $b_0 + b_1$ respectively. We expect this parameterization of the annihilation process to be insensitive to the nature of the nuclear cascade, so the parameters from PS209 should be applicable for PUMA.

Other inputs in the cascade calculation are:

1. $P(n_c, l)$: the initial distribution of the antiproton,
2. the Auger transition rates,
3. the refilling rate which is zero in the case of PUMA.

Table 1 Pion final states for antiproton-proton [83] and antiproton-neutron [84] annihilation. Not all decay channels are shown and, thus, the below branching ratios do not sum up to 100%

Antiproton-proton		Antiproton-neutron	
Pion final state	Branching	Pion final state	Branching
$\pi^0\pi^0$	0.00028	$\pi^-\pi^0$	0.0075
$\pi^0\pi^0\pi^0$	0.0076	$\pi^- k\pi^0 (k > 1)$	0.169
$\pi^0\pi^0\pi^0\pi^0$	0.03	$\pi^-\pi^-\pi^+$	0.0023
$\pi^+\pi^-$	0.0032	$\pi^-\pi^-\pi^+\pi^0$	0.17
$\pi^+\pi^-\pi^0$	0.069	$\pi^-\pi^-\pi^+ k\pi^0 (k > 1)$	0.397
$\pi^+\pi^-\pi^0\pi^0$	0.093	$\pi^-\pi^-\pi^-\pi^+\pi^+$	0.042
$\pi^+\pi^-\pi^0\pi^0\pi^0$	0.233	$\pi^-\pi^-\pi^-\pi^+\pi^+\pi^0$	0.12
$\pi^+\pi^-\pi^0\pi^0\pi^0\pi^0$	0.028	$\pi^-\pi^-\pi^-\pi^+\pi^+ k\pi^0 (k > 1)$	0.066
$\pi^+\pi^-\pi^+\pi^-$	0.069	$\pi^-\pi^-\pi^-\pi^-\pi^+\pi^+\pi^+ k\pi^0 (k \geq 0)$	0.0035
$\pi^+\pi^-\pi^+\pi^-\pi^0$	0.196		
$\pi^+\pi^-\pi^+\pi^-\pi^0\pi^0$	0.166		
$\pi^+\pi^-\pi^+\pi^-\pi^0\pi^0\pi^0$	0.042		
$\pi^+\pi^-\pi^+\pi^-\pi^+\pi^-$	0.021		
$\pi^+\pi^-\pi^+\pi^-\pi^+\pi^-\pi^0$	0.019		

2.2.4 Annihilation

The antiproton nucleon annihilation is a complex QCD process [82]. The final state results mostly in the production of pions. Branching values of final states after antiproton-nucleon annihilation have been measured [83,84]. The main decay channels are listed in Table 1.

2.2.5 Final-state interactions

Since the annihilation takes place in the vicinity of the nucleus, pions produced after the annihilation may re-interact with the residual nucleus with a variety of processes including absorption and charge exchange, generally labelled as Final-State Interactions (FSI) [85]. The interaction probability of the pions in the final state with the residual nucleus follows a geometrical solid-angle dependence [86].

As a phenomenological model of the FSI, the so-called four-parameter model was proposed by Wycech [87]. This model introduces parameters $\lambda^\pm$ and $\omega^\pm$, which represent the reaction probabilities of following FSIs: π^0 reacts with a residual nucleus and exchanges charge to become $\pi^\pm$ ($\lambda^\pm$), and $\pi^\pm$ loses its charge by absorption or charge exchange ($\omega^\pm$). The emitted pions have an average kinetic energy of about 500 MeV. In this energy region, pions can be considered to react with the residual nucleus at most once. Analyses of previous experimental data for stable nuclei have shown that the model parameters ($\lambda^\pm$ and $\omega^\pm$) are in the range of 0.1–0.2.

Since the electric charge of the primary pions is distorted by the effect of the FSI, it is not possible to determine the annihilation partner of the antiproton for each annihilation event. Wada and Yamazaki [88] proposed a method to determine the neutron-to-proton annihilation ratio by applying statistical analysis to multiple annihilation events. However, this method assumes knowledge of the strength of the FSI, which depends on the annihilation radius and the neutron and proton distribution on the surface of the nucleus, resulting in model dependence. We are developing a method using deep learning to determine the neutron-to-proton annihilation ratio from experimental data without a priori knowledge of the FSI [89]. The objective of PUMA is to reach a sensitivity better than 10% in the neutron-to-proton annihilation ratio.

2.3 Theoretical challenges and foreseen developments

With respect to a microscopic description of the antiprotonic atoms with halo nuclei and the subsequent annihilation, the challenges are twofold. First, one must achieve a precise description of exotic halo-nuclei and, in particular, of the tail of the nuclear-halo density distribution. The second concerns the precise determination of the complex energy shifts of the low-lying $\bar{p}$-A Coulomb-like resonant states with energies $E_\alpha = E_R - i\Gamma/2$ from where the annihilation of the captured antiproton takes place. These differences with respect to pure Coulomb states are a consequence of the strong and annihilation N$\bar{N}$ forces which shift and broaden the Coulomb orbits. They are defined as

$$\Delta E_\alpha = E_\alpha - E_C = \Delta E_R - i\frac{\Gamma}{2}, \tag{4}$$

where E_C is the Coulomb energy of the two-body p̄-A atom assuming a pointlike nuclear target. It is given by

$$E_C = -\frac{R_y}{n^2}, \qquad R_y = \frac{1}{2}\mu_{pA}c^2 Z\alpha^2, \qquad (5)$$

where Z is the nuclear atomic number and $\mu_{\bar{p}A}$ the antiproton-nucleus reduced mass. These level shifts represent a small fraction of the Coulomb energies (10^{-2} for S-waves, 10^{-6} for P-waves) and thus require an accurate solution of the A+1 many-body problem. It is worth pointing out that despite the smallness of the strong corrections ($\Delta E/E \ll 1$), the quantum mechanical problem is non-perturbative.

During the first stage of the program we have considered and compared the existing NN̄ interaction models. They might be classified into two groups depending on the way they model the annihilation process, i.e. Optical Models (OM) or Unitary Coupled-Channels Method (UCCM). From the optical models side, these are: Dover-Richard [90], Khono-Weise [91], Paris potential [92] and the recently developed chiral effective field theory inspired Jülich potential by Haidenbauer and collaborators [93]. Alternatively to optical potentials used to simulate the absorption towards the annihilation channels, one can use physical meson channels in the UCCM. The latter can lead to substantial differences with the former concerning the short range part of wave function.

Our interest is first to understand the stability of the theoretical predictions with respect to the model used for the annihilation process for the simplest antiprotonic systems, e.g. the protonium [94]. To do so, we have computed the lower p̄-p orbits with the different potentials as well as the corresponding annihilation densities $\gamma_\alpha(r)$ for the lowest states. This quantity is the spatial probability distribution of the annihilation process and its integral provide the total width of the sate. They can computed from wave function Ψ_α of the p̄-A resonant state and from the annihilation potential. In the OM case, it reads

$$\Gamma_\alpha = \int_0^\infty \gamma_\alpha(r)dr \quad \gamma_\alpha(r) = 2 \, \text{Im}\left[V_{N\bar{N}}(r))\right] \, |r\Psi_\alpha(r)|^2. \qquad (6)$$

In [95], it is shown that noticeable differences exist in the annihilation densities as well as in the short range part of the p̄-p wave functions between the OM and the UCCM. They are illustrated in Figs. 4, 11, 12 and 13 of that reference.

Secondly, the p̄-A Coulomb orbits are computed in a few light-nuclei for which an *ab initio* solution is accessible to study the influence of the influence of NN̄ potentials away from the fitting region. The Faddeev-Yakubovsky [96,97] equations in configuration space can be solved for solve A = 2, 3, 4 and 5 problems [97] accounting for the different asymptotic channels empowering us with quasi-exact solu-

tions of high-precision. First results for the $\bar{p}-^2$H (p̄-d) system have been obtained in [98] with N̄N OM. The p̄-d level shifts and widths were computed for the Kohno-Weise and Jülich potentials. They are compared to data, where discrepancies are observed in the P-waves. The p̄-d annihilation densities are found to match the deuteron nuclear density (see Fig. 3 from [98]). A sizeable fraction of the antiproton annihilation with nucleons inside the nucleus happens in the peripherical region, thus supporting the main intuition of PUMA project. This is a major outcome of the study. It was however found that the direct calculations of the tiny levels shifts ΔE_α are numerically involved and it is not clear today that the *ab initio* program could be extended beyond A=3 using this direct approach. To circumvent this difficult, the scattering p̄-d lengths are computed, which is much less demanding, and from which the complex level shifts ΔE_α can be computed by the means of the Trueman relation [99,100]. The results were satisfactory for a large family of states and this paves the way of an alternative approach based on the scattering solutions which can reach larger nuclear targets.

After obtaining the exact solution in a few test nuclei, we will make use of another *ab initio* method that computes bound and scattering states alike [101], based on the No-Core Shell Model. This method has been very successful in describing reactions of a nucleon, deuteron or alpha particle impinging on light- to medium-mass nuclei, up to $A \sim 12$ [102–105] as well as two-neutron halo continuum [106]. This will allow us to study the evolution towards heavier and exotic systems targeted by the PUMA experiment. This program will provide us with set of nuclei for which the widths of the antiprotonic Coulomb orbits can be directly computed with no other approximations than the ones included when developing fundamental models of the N̄N interaction.

Having at our disposal the exact solution for the simplest systems, the last step consists in validating the results of the p̄-nucleus (p̄-A) optical potential approach and, if needed, refining the theoretical framework for instance using halo Effective Field Theory. This approach is indeed based on the assumption that the p̄-A optical potential is directly related to the nuclear density $\rho(r)$ by the means of expressions alike

$$V(r) = \frac{2\pi}{\mu_{pA}} a_{\bar{p}p} \, \rho(r), \qquad (7)$$

where $a_{\bar{p}p}$ is the scattering length and the μ_{pA} denotes the reduced mass of the p̄-A system. It is worth to emphasize that this ansatz has never been compared to an *ab initio* calculation where all nucleonic degrees of freedom are accounted for. A first attempt to obtain a p̄d optical potential based on the folding approximation was obtained in . It is found that this approximation works reasonably well for S-states but

is unable to reproduce the P-waves level shifts. To confirm or infirm the validity of (7) or similar antiproton - nucleus potentials, and eventually determine what kind of corrections would be required, constitutes an milestone of the theory developments within the PUMA experiment.

3 The PUMA experiment

The first objectives of the PUMA experiment are

– to provide a new observable for radioactive nuclei that characterises the neutron-to-proton asymmetry of their density tail, namely the neutron-to-proton annihilation ratio,
– to characterize the density tail of known halos and neutron skins with this new method,
– to evidence new proton and neutron halos,
– to understand the development of neutron skins in medium-mass nuclei along isotopic chains.

The proposed method is indeed first an unambiguous discovery tool for halos: annihilation from a neutron halo nucleus should lead to a neutron-to-proton annihilation ratio exceeding by an order of magnitude the N/Z ratio of the nucleus (following qualitatively the halo definition proposed in [26]), annihilation from a proton halo, on the contrary, should lead to a neutron-to-proton annihilation ratio significantly smaller than unity. Neutron skins could be characterized by a neutron-to-proton annihilation ratio larger than N/Z. To illustrate the sensitivity of the n/p-annihilation ratio to neutron skins, we calculated the expected value for three tin isotopes with realistic proton and neutron densities: in the case of the stable ^{124}Sn, the expected neutron-to-proton annihilation ratio is 2.13, while it is close to unity for the neutron-deficient ^{104}Sn and 2.35 for the neutron-rich ^{132}Sn. These values are to be compared to $N/Z = 1.48$, 1.08 and 1.64, respectively. This example illustrates that a relative accuracy of 10% or better for the neutron-to-proton annihilation ratio is sufficient to provide first quantitative information on the neutron-skin growth as a function of the neutron number. The expected range of neutron-to-proton annihilations are summarized in Table 2.

The foreseen studies are expected to provide new information on the nuclear many-body problem, which may eventually shed light on our understanding of neutron(-rich) matter at low density. Note that the observable provided by PUMA is the ratio of neutron-antiproton annihilations and proton-antiproton annihilations after antiproton capture. This quantity is to be connected to the neutron-over-proton density ratio integrated over the region of annihilation sites, i.e. in the tail on the nuclear radial density. PUMA is then complementary to measurements aiming at neutron-skin thickness

Table 2 Expected neutron-to-proton annihilation ratios in the case of a neutron halo, a proton halo or a neutron skin in a nucleus composed of N neutrons and Z protons. $R = \sigma_{\bar{p}n}/\sigma_{\bar{p}n}$ is the ratio of the antiproton annihilation cross section at low energy with a neutron and a proton. Experiment gives $R = 0.63$ [3]

	n/p-annihilation ratio
Neutron halo	$\geq 10 \times N/Z \times R$
Proton halo	$\ll R$
Neutron skin	$> N/Z \times R$

determination and is sensitive to the tail of the radial density distribution, so far unexplored.

Several physics cases have been identified as suitable for the investigation of the neutron and proton composition of the nuclear density tail in stable and radioactive nuclei, ranging from He to Pb isotopes. They will all be measured under the same experimental conditions. It is important to note that (i) reference measurements with stable nuclei will first be done at ELENA and will provide benchmark data for the response function of the device (detection and tracking efficiencies, signal-to-background determination), as well as benchmarks for theory and the foreseen interpretation method, (ii) the analysis of high statistics reference measurements at ELENA might lead to new prospects for PUMA (see below), (iii) measurements along isotopic chains are believed to be important since they will allow studies which may provide more (relative) accuracy than individual measurements. Note that at both ELENA and ISOLDE ion beams with an isotopic purity better than 99% are needed. This requirement will be fulfilled by the use of multi-reflection time-of-flight (MR-ToF) devices (see Sects. 5.4 and 7.3).

In practice, PUMA aims to transport one billion antiprotons from ELENA to ISOLDE to perform experiments on short-lived nuclei with antiprotons. Figure 10 shows a sketch of the PUMA Penning-Malmberg trap which will consist of a storage zone (S trap) dedicated to the storage of a large amount of antiprotons, and a collision zone (C trap) dedicated to the interaction of antiprotons with unstable ions. 10^9 antiprotons will be stored at ELENA in the S trap. The entire system will be transported on a truck to ISOLDE. There, typically, 10^7 to 10^8 antiprotons will be transferred from the S trap to the C trap were the actual experiment with the radioactive ions will take place. Both zones will be located in a 4 T magnetic field provided by a superconducting solenoid. Pions issued from annihilations will be detected by a cylindrical Time Projection Chamber (TPC) surrounding the C trap. The curvature of the charged pions in the magnetic field of the trap will allow identification of the charge of the measured pions. After including the corrections from final-state interactions, we will determine the ratio of neutron-antiproton annihilations and proton-antiproton annihilations following
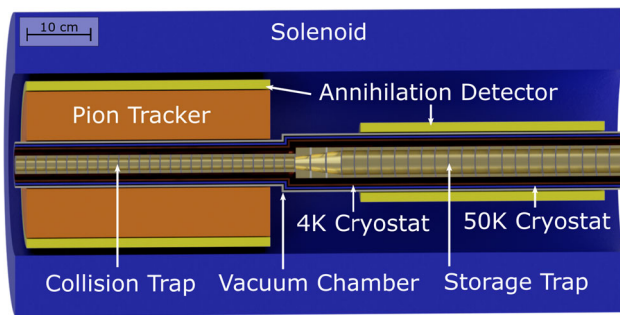
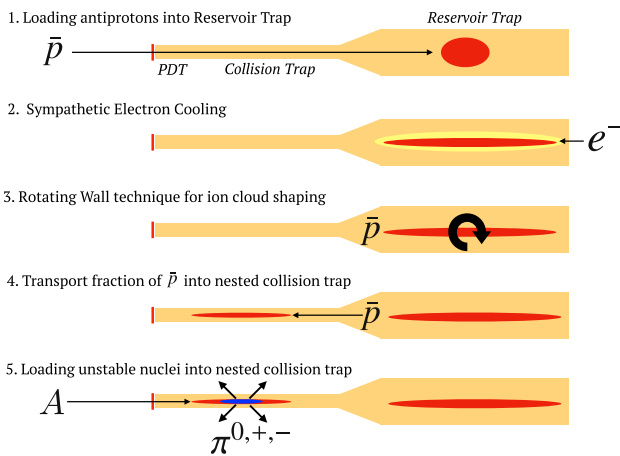**Fig. 10** Schematic view of the PUMA pion detection and trap setup

Fig. 11 Conceptional operation scheme of PUMA. The trap entrance is equipped with a pulsed drift tube (PDT) to adjust the energy of the ions when injected into the trap. Dimensions are not at scale

the antiproton capture. This is the core observable provided by PUMA.

A proposed operation scheme of the system is presented in Fig. 11. The scheme will consist of five key techniques: a pulsed drift tube (PDT) to slow down antiprotons and ions at the entrance of the two traps, sympathetic electron cooling, a rotating wall drive for the antiproton cloud shaping, fractional extraction of antiprotons from the reservoir, and nested potential to trap positively-charged ions in the same region. Details on the devices are given in Sect. 4.

Although the details of each experimental campaign at ISOLDE should be described in later individual proposals to the physics advisory committee of the ISOLDE facility, an estimate of the counting rate expected from annihilations in PUMA is given in the following to illustrate the orders of magnitude. The annihilation cross section of an individual nucleus with stored antiprotons is estimated to reach 10^6 barns at 100 eV relative energy [68]. Antiprotons annihilate with both protons and neutrons. The respective decay channels are composed of energetic pions with conservation of the initial charge and momentum of the antiproton-nucleon system (see Table 1).

Assuming an antiproton capture cross section of 10^{-16} cm^{-2}, and an antiproton plasma of thickness 10^8 cm^{-2}, every ion at 100 eV will fly through the antiproton cloud 2×10^6 times when trapped for a 1 s total duration. In the case of a stable or long-lived nucleus introduced in a bunch of 10^4 ions into the antiproton plasma, the corresponding annihilation rate will be 100 Hz. A high-statistics measurement with stable ions will therefore last a few minutes, the limiting factor being the acquisition rate of the detector readout which is about 1 kHz with the considered electronics, see Sec. 4.5.7.

In the case of the most exotic short-lived nuclei such as ^{11}Li, the number of nuclei introduced per cycle is smaller and the time the nuclei spend in the antiproton plasma is limited by their half life. We assume that ^{11}Li nuclei are produced at $1000 \, s^{-1}$. Every ion at 100 eV will fly through the antiproton cloud 2×10^4 times when trapped for a 10 ms total duration. In this extreme case, the corresponding annihilation rate will be 10 per minute. To achieve this sensitivity, the design and conception of PUMA requires an extreme-high vacuum inside the trap to minimize the background from residual-gas-induced annihilations (see Sect. 4.7).

4 Status of PUMA

4.1 Overview

PUMA will integrate several functions in one transportable experiment frame: solenoid including the ion traps, vacuum systems, electronics for the trap operation and ion and antiproton plasma diagnostics, annihilation detection and its electronics, compressors and cold heads for cooling the solenoid and the trap and a uninterruptible power supply (UPS) and a water chiller system for the transport phase. All these functions are integrated into two separable frames: (i) a main frame containing the solenoid, trap and all functions necessary for the operation of PUMA, and (ii) an annex frame for the UPS, batteries and chiller. The full system is 5.4 m long, 2.7 m high and 1.9 m wide. The main frame is 3.5 m long, while the annex frame is 1.9 m long. The dimensions are fixed by external constraints: the 5.4 m length is limited by the delivery zones of ELENA and ISOLDE. The 2.7 m height is the standard height of containers. It is limited by the crane operations at ELENA. The total weight of PUMA is estimated to 9.9 tons decomposed as follows: 6.33(3) tons for the solenoid and main frame, 2.92(2) tons for the annex frame (with water-filled chiller) and 0.6 ton for physics instruments. The total electrical power consumption of the device is estimated to 45 kW with a maximum consumption of 71 kW when the chiller is on. The system as defined today is shown in Fig. 12.

The heart of the PUMA setup consists of a solenoid and a double Penning trap inside a single 4-K cryostat. In the
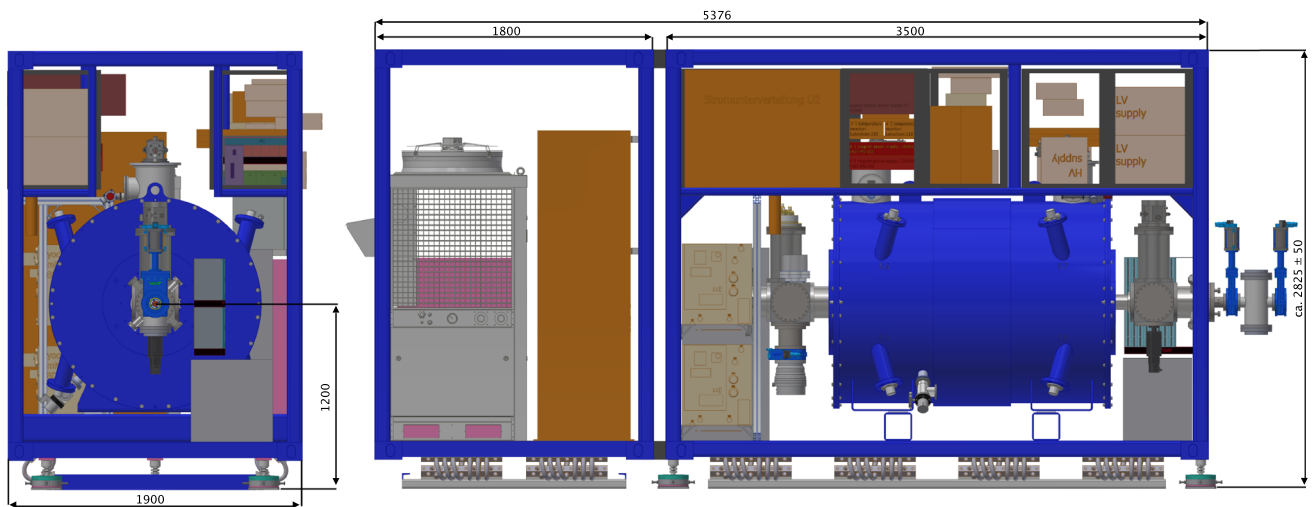
Fig. 12 Conceptual view of PUMA. See text for details

early design phase, a two-solenoid option, one for the transport and one for the physics measurements, was investigated but quickly abandoned after considering the advantages of the single-solenoid alternative. (i) Both the antiproton storage and the annihilation measurement require a vacuum of 10^{-17} mbar. A single 4-K cryostat separated by a conductance reduction pipe guarantees the best experimental conditions for PUMA. (ii) The use of two solenoids would require an additional XHV transfer line between them, additional XHV efforts to create two separate regions at 10^{-17} mbar for transport and collisions, as well as additional alignment efforts between the two traps. (iii) Two separate solenoids implies that the antiproton, while being transferred from one to the other, will go through a high-low-high magnetic field sequence, impacting the size of the antiproton spill. (iv) First physics measurements will be performed with stable nuclei at ELENA. A one-solenoid setup with an identical setup at both ELENA and ISOLDE guarantees complete consistency of measurements at both facilities. (v) To ensure safety during the transport and flexibility of operation, we chose a cryogen-free option for the cooling of the magnet coils. This implies that the transport frame hosts, in addition to the solenoid, compressors and electronics, a UPS, batteries and a water chiller. The gain of switching from one large solenoid to a smaller one dedicated to transport only would not have simplified but rather complicated the experimental procedures.

4.2 Solenoid

4.2.1 Introduction

The cylindrical Penning trap is a key component for PUMA to trap antiprotons and ions. Charged particles in the trap are confined axially by electrostatic potentials, and radially by a strong magnetic field which is provided by the superconducting solenoid. The solenoid provides a homogeneous magnetic field of 4 Tesla over a length of 900 mm along the symmetry axis of the solenoid (z axis in the following) in a 280-mm-diameter horizontal warm bore with active shielding to reduce the stray magnetic field surrounding the magnet. The dimensions are dictated by the requirements for a good tracking efficiency for pions and the two-trap geometry. Both passive and active shields are implemented to reduce the magnetic stray field. The solenoid was built by the company Bilfinger Noell.

Requirements on the magnetic field provided by the solenoid are summarized in Table 3. The field inhomogeneity is required to be less than 0.2% in each trapping region to minimize the effect on the non-neutral-plasma lifetime. Also, the inhomogeneity in the overall volume relevant for the pion tracking is requested to be less than 5% to avoid significant distortions on the electron drift in the time-projection chamber (see Sect. 4.5). The constraint on the stray field was set to be below 3×10^{-4} T at three meters away from the center both axially and radially to satisfy the safety regulations during transportation and handling of the magnet and not to interfere with surrounding devices and other experiments in the experimental area.

4.2.2 Design

The PUMA magnet system was first optimized without the passive shield to determine the coil layout and to estimate the coil parameters to create the trapping volumes according to the requirements. Important physical parameters such as homogeneity of the magnetic field, load lines, conductor type and length, stray field, inductance and stored energy were considered during the optimization. Subsequently, the

Table 3 Requirements for the solenoid. $\delta B = |\mathbf{B} - \mathbf{B}_0|$ is defined as the norm of the magnetic field difference relative to the nominal value $\mathbf{B}_0$

Requirements	Values
Nominal strength inside the magnet	4.0 T
Relative stability over one day	$< 10^{-4}$
Homogeneity in storage region	$\delta B/B_0 < 0.2\%$
Homogeneity in collision region	$\delta B/B_0 < 0.2\%$
Homogeneity in tracking region	$\delta B/B_0 < 5\%$
Strength 3 m from center along axis	< 0.3 mT
Strength 3 m from center $\perp$ to axis	< 0.3 mT

Fig. 13 The stray field of the magnet arrangement including both the active and passive shield. The blue line indicates the 0.3 mT (3 Gauss) limit and the pink line indicates the 5 mT limit. Distances are given in mm

dimensions of the passive shield were optimized to minimize the total weight, while avoiding saturation and keeping the shielding effect. The parameters such as shielding length, thicknesses of the cylinder and end plates were considered. Finally the coil configurations are optimized again together with the passive shield to meet all the requirements.

The solenoid consists of seven coils made of NbTi superconducting wire: a main coil, a pair of booster coils, a pair of active shielding coils and a pair of shim coils. All the coils have the same operation current to share a single power supply and to share one pair of current leads. According to simulations the homogeneity $|B - B_0|/B_0$ within the trapping volumes is 0.087% which is less than half of the required 0.2%. The homogeneity $|B - B_0|/B_0$ within the tracking volume is 2.37% which is also less than half of the required 5%.

The passive shields are made of AISI 1010 steel and consist of a cylinder and two end plates with 20 mm thickness. A ring with 20 mm thickness and 500 mm length is arranged outside the middle surface of the outer cylinder. A ring with 30 mm thickness and 200 mm width is added to each end plate to avoid saturation. The total weight of the presented passive shield is 1950 kg. The magnetization over most of the shield is lower than 1.5 T. The magnetization of the shield at the step between the ring and the cylinder is between 1.5 T and 1.6 T. Only the corner between the end plate and the warm bore is saturated.

4.2.3 Stray fields

The stray field of PUMA including the passive shield is shown in Fig. 13. The 0.3-mT line is about 1.8 m away from the center of the solenoid along the z-axis and about 1.1 m along the radial direction, as indicated by a blue line on the figure. The 5-mT line is just outside the cryostat along the radial direction, and about 1.25 m away from the center of the solenoid along the axial direction, as indicated in pink.
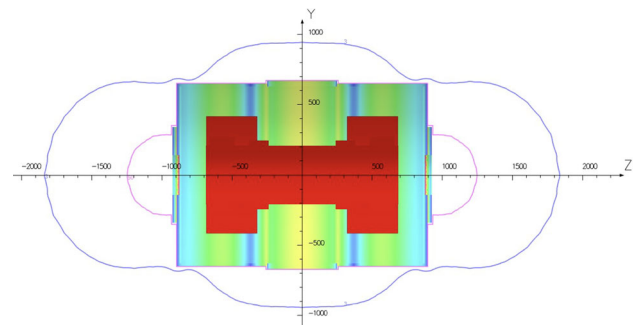
Table 4 Details of the calculated heat loads on the 60 K and 4 K stages of the solenoid cryostat

Source	Losses 60 K (W)	Losses 4 K (W)
Radiation	20.7	0.37
Instrumentation	0.1	0.03
Support, rods	5.3	0.28
Current leads	19.0	0.09
Total	45.1	0.77

4.2.4 Quench computations

Various quench cases have been simulated within the OPERA quench software [107]. In summary, the hot-spot temperature stays below 110 K.

The stray field during a PUMA quench process without iron shield has been computed. The following conclusions can be drawn: (i) B at point (3 m, 0, 0) is always lower than the original value 0.16 mT. (ii) B at point (0, 0, 3 m) has a peak value of 0.35 mT at 2.17 s.

4.2.5 Cryogenic design

The magnet system is cryogen-free. Established design concepts have been used for the cryogenic design throughout. The total heat losses are summarised in Table 4.

Two Gifford-McMahon (GM) coolers, Sumitomo RDK-408D2 are used. At the heat load as given in Table 4, the first and second stage loading of 23 W and 0.4 W leads to an estimated temperature of the coolers of 38 K and 3.8 K, respectively.

The total cold mass of PUMA has a weight of about 1750 kg. The cool down time is computed to be 760 hours (31 days).
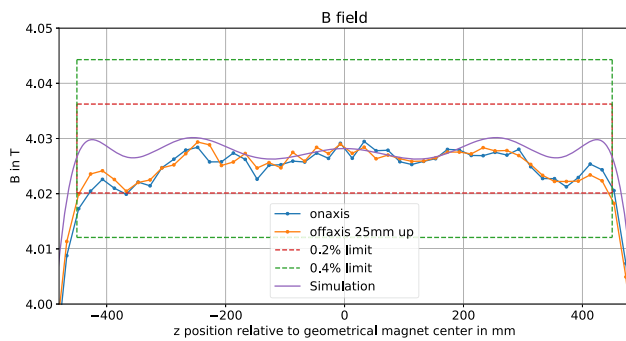
Fig. 14 Comparison of the simulated and measured magnetic field. For the comparison, the simulated values were shifted to match the measured values at $z = 0$ mm

4.2.6 Measured performances

The measured cool-down time is 25 days. The temperature of the cold mass has been measured at 3.3 K. As a test of the thermal inertia, the cryocoolers have been stopped for 60 s: the temperature rose up to 3.5 K, demonstrating an excellent thermal isolation and a resistance of the system against short power shortages.

During quenching most of the stored energy is deposited in the cold mass. The cold mass will heat up and reach about 40 K in thermal equilibrium. The subsequent cool down with two cryocoolers will take less than 24 h.

During the first powering of the solenoid, up to a magnetic field of 4.04 T, the nominal values were reached without quenching.

To confirm the specifications of the solenoid, the magnetic field was measured with a Nuclear Magnetic Resonance (NMR) probe (PT2025, Metrolabs) and a 3D Hall probe (THM1176, Metrolabs). The magnetic field, measured with the NMR probe, is compared to the simulated on-axis magnetic field, corrected for an offset. The measurement shows that, further away from the center, the magnetic field is lower than simulated, but still within the limits of 0.2%. At the edge of the solenoid bore where the field magnitude drops, the variations over the probe dimensions were too large to perform a reliable measurement. To cover the total volume, the 3D Hall probe was used. The measurement of the magnetic field with the 3D Hall probe (see Fig. 14) shows, that only at the edge of the storage and collision regions, the deviation from the central magnetic field is close to the 0.2% limit. This is true for the on-axis field as well as the field at the edge of the volume 25 mm from the center. The field at the edge of the tracking volume is well within the 5% limit and the time stability is better than $4 \cdot 10^{-6}$ over 1 h. Furthermore, we confirmed that the stray magnetic field falls below 0.3 mT well within 3 m, axially as well as radially, in agreement with computations.

4.2.7 Positioning in frame and alignment

The cryostat, the cooling systems, the magnet control system, and the trap with all ancillary electronics are mounted into the main frame. The UPS and the water chiller are mounted into the annex frame. The ensemble composed of the solenoid, its ancillaries, and the UPS inside the frame were delivered to TU Darmstadt.

The alignment of the PUMA system with respect to the beamline at ELENA and at ISOLDE will be guaranteed by three alignment feet, which can sustain a load of 3.4 tons each. Each foot has adjustment pins to correct the horizontal and vertical position. The foot positions will be adjustable up to ± 10 mm in both horizontal directions, and ± 15 mm in the vertical direction. This vertical range is suited to compensate the measured maximum fluctuations of floor flatness measured at the PUMA experimental location at ELENA. A conical pin at the center bolt allows smooth coupling with the hole prepared on the frame. The feet can be bolted directly into the ground of the experimental area and thus the frame can be put back into the aligned position, in a reproducible way, after the PUMA frame was moved.

The magnet cryostat has holes dedicated to target markers in view of laser alignment. The targets will be installed at both end caps and at all eight turrets of the cold mass suspension. The dimensions are compliant with the LEICA standard used at CERN (diameter 8H7 and a clearance hole of diameter 27 mm).

4.2.8 Damping system

The main and annex frames have a damping system to reduce the acceleration of the main frame with all equipment installed. The damping system has appropriate damping properties to avoid oscillations. It will be used

(a) when shipping the system in warm conditions,
(b) when transporting the running system, with magnetic field switched on, over short distance and under controlled conditions from one experimental site to the other.

The damping system is composed of wire rope isolators composed of stainless steel stranded cable threaded through aluminum alloy retaining bars that are mounted for effective shock and vibration isolation. For PUMA, 12 identical six-loop isolators are used: 8 below the main frame, and 4 below the external frame. The damping was sized so that the solenoid does not experience accelerations exceeding 6 m·s^{-2} in realistic scenarios of normal operation.

In addition to the damping system of the frame, the solenoid coils are not rigidly attached to the solenoid cryostat. The spring constants of the cold mass suspension within the cryostat are 8000 N/mm in horizontal, 30300 N/mm in verti-

cal, and 9500 N/mm in axial direction. The cold mass weight is about 1400 kg. This is to be taken into account when a detailed estimate of the magnetic field variations at the location of the plasma during transportation will be performed. Such simulations have not been undertaken yet.

4.3 Penning traps

4.3.1 Overview

The aim of PUMA is to combine the storage and transportation of antiprotons with the investigation of short-lived ions by antiproton annihilations in a single setup. For this purpose, a portable Penning trap setup will be used which consists of two trapping regions: (i) a large-diameter cylindrical multi-ring Penning trap is used for the trapping and storage of the antiprotons during the transportation (storage trap), (ii) a small-diameter cylindrical multi-ring Penning trap with a nested potential for the combined storage of positively charged short-lived ions and negatively charged antiprotons is used for the investigation of antiproton annihilations on the nuclear surface (collision trap). Cylindrical Penning traps have already been used at different ELENA experiments for the trapping of antiprotons and the production of antihydrogen [108–110]. Within both trapping regions, the ring electrodes shape the electrostatic potential which confines the trapped particles in axial direction, while the radial confinement is ensured by the 4-T magnetic field of the solenoid.

The main goals of PUMA are the storage of up to 10^9 antiprotons within the storage trap, the transportation from the ELENA to the ISOLDE facility and the investigation of short-lived ions by surface annihilations with antiprotons. At the first stage of the project, the physics measurements at ISOLDE will be performed with a few 10^7 antiprotons. Within the storage trap, the effective trapping volume for the antiprotons can be tuned between about 10 cm^3 up to 30 cm^3 by defining potential wells of different lengths with the ring electrodes of the trap. Considering the aim of up to 10^9 stored antiprotons, this would correspond to an antiproton density of up to $n_{\bar{p}} = 1 \cdot 10^8$ cm^{-3}, or to about 0.25% of the Brillouin density limit of $n_B = \epsilon_0 B^2 / 2m_{\bar{p}} = 4.23 \cdot 10^{10}$ cm^{-3}. Due to field imperfections in a real trap the achievable densities are significantly lower. The maximum densities that have been achieved for ion trapping are at about 20% of the Brillouin limit for up to 10^9 Mg$^+$ ions [111], which are much higher than the densities that PUMA requires, and about 10^7 antiprotons have already been trapped by AEgIS [112].

The Brillouin density limit represents the density limit arising from the limited magnetic field providing the radial confinement of the trapped antiprotons. At the same time, the maximum density of particles is limited by the axial electric field provided by the trap electrodes. In the case of PUMA, the potential well will have a depth of up to 500 V, which

has to be deep enough to overcome the (axial) space charge potential of the trapped antiproton ensemble. Assuming an ensemble length of about 10 cm and radius of about 1 cm for 10^9 antiprotons, the space charge potential is in the order of 70 V, well below the considered maximum voltage.

4.3.2 Electrodes

This section summarizes the design of the collision and storage traps, while focusing on the material and geometry of the traps as well as the related electronics.

Due to the different purposes and foreseen particle numbers, the ring electrodes of the two traps have two specific geometries as shown in Fig. 15. This translates to a larger inner electrode radius r_{st} in the storage trap with $r_{st} = 20$ mm compared to the smaller radius of the collision trap electrodes $r_{col} = 10$ mm. The lengths of the two different electrode types were chosen to comply with a length-to-radius ratio of $l_{st}/r_{st} = 0.85$ and $l_{col}/r_{col} = 0.7$, respectively, leading to a storage trap electrode length of $l_{st} = 17$ mm and a collision trap electrode length of $l_{col} = 7$ mm. The length-to-radius ratios were chosen based on the design values of other MRT experiments, which are typically in the range of 0.7 to about 1.0 [113,114], while the absolute values of the diameters are chosen to provide a sufficiently large trapping volume in the order of tens of cubic centimeters. Besides the basic cylindrical trap electrodes we also use azimuthally segmented electrodes. For both traps four-fold as well as eight-fold segmented electrodes are implemented (see Fig. 15), which will be used for applying the rotating-wall compression on the stored antiprotons [115,116].

For the storage trap a total of 24 electrodes will be used for shaping the harmonic potential well, while two segmented electrodes and two additional electrodes directly next to the segmented electrodes will be kept at ground potential for excitation and for picking up the induced charge of the plasma in the trap. The voltages that can be applied to the electrodes range from −500 V to + 500 V. For the storage trap a harmonic axial potential well will be used, since it provides a good confinement for small particle numbers up to high density ensembles. In the storage trap this harmonic potential will be provided by the 14 inner electrodes including one central segmented electrode. Additionally, the trap center will be surrounded by the pick-up and two more segmented electrodes as well as four electrodes for catching the incoming particles (two at each end of the storage trap).

The potential shape of the collision trap, in contrast, will not have a constant shape, as it has to be adjusted to each individual ion species and the related beam energies. A nested potential is necessary to store both positively charged ions and negatively charged antiprotons in the same volume of the trap simultaneously. To be able to transport, manipulate and store the p̄ as well as the negative or positive ions first inde-
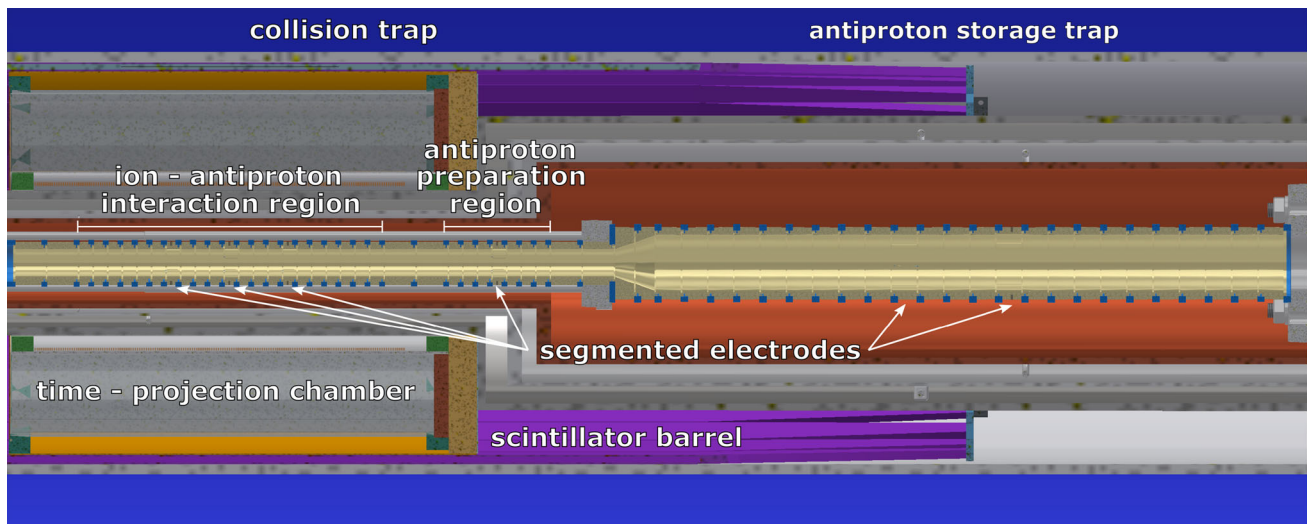
Fig. 15 Half-cut CAD view of the storage as well as the collision region of the PUMA trap tower. The different volumes in which the p̄ and ions are stored prior to the central interaction trap are indicated. Furthermore, the position of the segmented electrodes for plasma manipulation are shown

pendently, the collision trap consists of 59 electrodes. With this number of electrodes, different potential arrangements as well as trapping wells can be formed. A trapping region in which the annihilation reactions are supposed to take place, is foreseen to be located central to the time-projection chamber (TPC), so that the pion signal can be detected with highest efficiency. This trapping region, as well as an upstream region for the initial p̄ tracking before interaction is equipped with a central and two laterally placed segmented electrodes for plasma manipulation. Dedicated potential shapes will be investigated with the test setup at the TU Darmstadt, where the storage of electrons and light positive and negative ions will be tested.

High-purity oxygen-free electronic (OFE) copper (UNS 10100, 99.999%) was chosen for the electrodes and pure sapphire (Al_2O_3) for the insulator rings due to their high thermal conductivity and low outgassing rates in vacuum [117,118].

To avoid large asymmetries over the full stack of electrodes, all electrodes and copper rings have to be machined within a deviation of at maximum $20\,\mu m$ from the nominal values. This precision is most important for the fitting of the electrodes with the insulator rings, because loose fittings might lead to a bending of the trap main axis, making a highly precise alignment of the trap with the magnetic field difficult. In addition, the precision is crucial for a successful operation of the segmented electrodes, whose segments are separated by sapphire balls of 1.5 mm diameter. The first set of 22 copper electrodes was manufactured by the fine mechanics workshop at TU Darmstadt from OFE copper. An additional step to reduce the impact of patch potentials on the electrodes is to plate the electrodes first with a thin layer of silver ($5\,\mu m$)

and secondly with a thicker layer of gold ($25\,\mu m$). Before the electrodes can be galvanically plated, the surfaces of the copper electrodes have to be high-gloss polished, so that the silver and the gold layer are evenly applied to all surfaces. The thin silver layer is necessary to avoid an immigration of the gold molecules into the copper, which tends to occur at high temperatures during baking. An overview over the different production stages is given in Fig. 16.

To connect the electrodes to a power supply via cables, each full ring electrode has a set of four M2 threaded holes equally distributed on the outer surface. In case of the azimuthally segmented electrodes, each individual segment has M2 threaded holes. Each cable is wrapped around a non-magnetic A4 stainless steel M2 screw, which is then threaded into the electrodes.

After the polishing and plating, the full set of electrodes can be assembled together with the sapphire insulator rings to form the base body of the cylindrical Penning trap (compare Fig. 17).

For a proper operation of the setup, alignment of the magnetic field lines of the solenoid and the center axis of the cylindrical electrode stack is necessary. A misalignment of both axes gives rise to azimuthal asymmetries in the electric field, which distort the particle motion within the trap [119]. In case of an ensemble with high particle number, as it will be the case of the storage trap, the effect of these asymmetries is usually modelled by an azimuthal drag which decreases the total angular momentum of the plasma, leading to a radial expansion over time [120]. Thus, to reduce the impact of these asymmetries an alignment in the order of 0.1 mrad is necessary for successful long term storage [118].
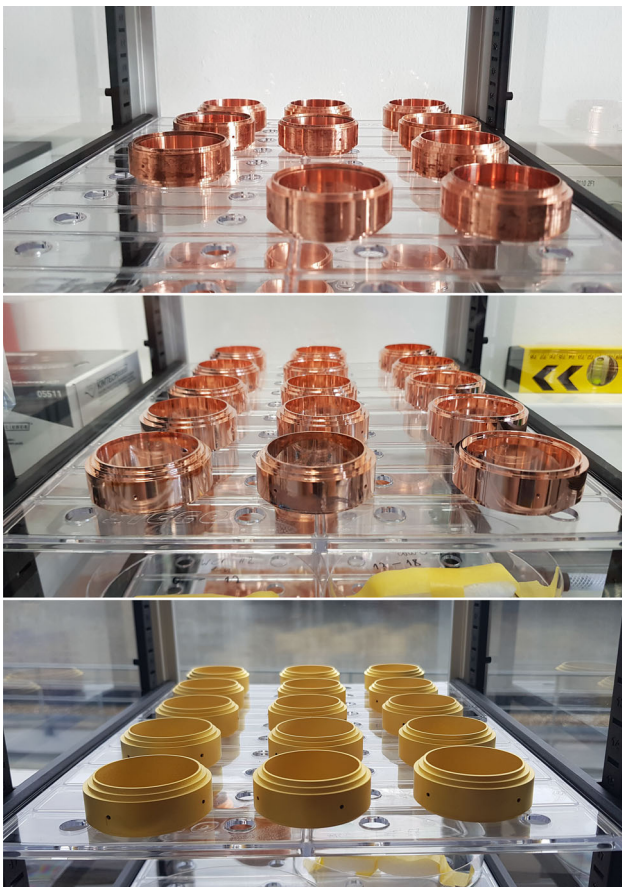
Fig. 16 Photos of electrodes at different stages of the production: after the lathing from the copper tube (top), after the electro-chemical polishing (center) and after the plating with silver and gold (bottom)
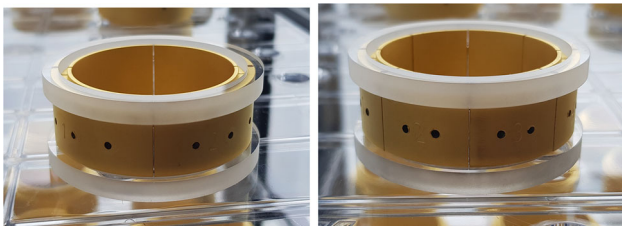

Fig. 17 Photos of the fully assembled and plated 4-fold segmented electrode (left) and 8-fold segmented electrode (right)

To decrease the misalignment and the resulting plasma expansion as much as possible, a dedicated alignment system will be built, which allows to adjust the angle between the geometrical and magnetic field axes with sub-milliradian precision. This system is based on an electron emission filament, a small aperture of $100\,\mu$m and segmented pick-up plates, which allow a position-sensitive detection of the electrons transmitted through the aperture. Due to the small radial expansion of the electron beam behind the aperture this method allows for a position detection within sub-millimeter range. As the electrons tightly follow the magnetic field lines

due to their small mass, this method gives a precise depiction of the location of the magnetic field axis. By the use of two support sleeves on both end caps of the solenoid, which are equipped with micrometer screws, the position of the vacuum chamber within the bore of the solenoid can be adjusted with micrometer precision.

4.3.3 Cables and feedthroughs

The cabling of the trap electrodes is done from the 4.2 K region to the 45 K region via an intermediate flange that decouples both regions thermally from each other. The design of this flange is currently under discussion. The cables that are to be used between the electrodes and the intermediate connection flange are made out of kapton insulated manganin (Cu-Mn-Ni alloy) which offers a high electrical conductivity while still ensuring a low thermal conductivity.

The intermediate stage of the cable feedthrough will also contain appropriate filters for those elements which will require such. In total 58 electrodes in the Penning trap stack will be connected electrically. To assess the impact that the cable connections to the electrodes will have on the thermal load of the assembly, a simplified representation of the cables has been included in simulations made with COMSOL to optimize the temperature distribution and determine the required cooling power of the system. For the connection from the vacuum to the room-temperature side, compact high density multi-pin feedthroughs will be used.

4.3.4 Voltage supply and control

The Penning trap has 24 electrodes in the storage region (Sect. 4.3.2). As described in detail in Sect. 4.4, the voltages of these electrodes need to controlled with high precision for the antiproton trapping and cooling procedure. The typical applied voltage is ± 500 V. In order to perform complicated operation modes described in Sect. 4.4.2, the voltage applied to each electrode must be synchronized. Conventional high-density high-voltage power supplies do not meet these requirements. Thus, PUMA uses a combination of a high voltage amplifier and a digital to analog converter (DAC) that outputs a programmed arbitrary waveform. Some electrodes require highly synchronized operation (rotating wall technique in Sect. 4.4). The signal waveform to these electrodes is generated by a rotating wall drive manufactured by Stahl Electronics[2]. When the ions are injected or ejected, the electrodes located at the edge of the potential well need to change the voltage instantaneously, with a jitter of typically less than 50 ns. Since the response speed of the high voltage amplifier is not sufficient for this, a fast switch is used to change the voltage within ~ 10 ns.

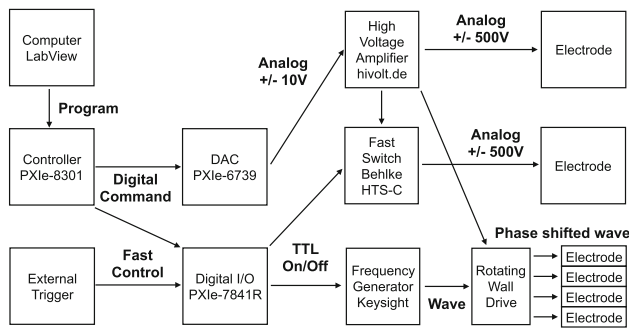[2] https://www.stahl-electronics.com.

Fig. 18 Overview of the PUMA ion trap electronics and control

The electronics of the Penning trap are controlled by a PXI express (PXIe) system from National Instruments as widely used in trap control. A schematic view of the trap electronics is shown in Fig. 18. A command sequence programmed by LabVIEW is first processed by the host computer, and then distributed via the digital analog converter (DAC) and other input/output (I/O) modules to all electronics devices. For operations that require fast synchronization to an external trigger, such as capturing of antiprotons and ions where switching with a precision of at least 50 ns is necessary, an PXIe-7841R FPGA card from NI is used [121].

As described in Sect. 4.4, the PUMA experiment include, in general, various steps, such as antiproton accumulation/cooling, transport of some of the stored antiprotons from the storage zone to the collision zone, and introduction of unstable nuclei. During each of these steps, the voltage of each electrode needs to be controlled by a combination of modules described below. For this purpose, a software control system is used based on the CS++ framework [122] developed at GSI. CS++ is the successor of the control system CS [123], which is nowadays widely in operation in mass measurement penning trap experiments like SHIPTRAP [124], ISOLTRAP [125], or LEBIT [126]. The open-source CS++ libraries extend the Actor Framework implementation in National Instruments' LabVIEW and add needed flexibility and network-wide communication for often modified experiments. Since it relies solely on libraries developed by National Instruments, it is much easier to maintain.

A high voltage amplifier (HAR-8X8A from hivolt.de GmbH & Co. KG) is used to supply a trapping potential to each electrode. It has a fixed gain of $50 \pm 0.3\%$, and amplifies input voltage of ± 10 V, and thus provides ± 500 V to each electrode. The slew rate is 20 V/μs, and the noise level is 3 mV$_{RMS}$, at capacitive load of 500 pF. The specification is comparable to similar devices used at AD experiments, AEgIS for example [113]. The amplifier chassis has high density design ideal for transportation, and directly controllable via National Instruments PXIe-6739 DAC.

Frequency generators are used to provide sine waves for the rotating wall and to drive the stored particles. PUMA employs the Keysight 33500B series. They are widely used among the ion trap community, and satisfy our requirement of a frequency range up to GHz, an accuracy of $\pm 1\%$, and a controlability through an external trigger.

A customized rotating wall drive from Stahl electronics provides phase-shifted sine waves to the segmented electrodes. The device will provide eight $45°$-phase shifted sine waves on top of the DC offset voltage. The covered frequency range is 0.8 to 10 MHz with maximum wave amplitude of 2 V$_{pp}$.

Fast switches are used to turn on and off trapping voltages to load and unload particles from the trap. In the case of loading and unloading the electrons, for example, the voltage should be lowered for a very short period of time, typically in the order of 50 ns. This operation is performed by a push-pull transistor switch HTS series made by Behlke electronic GmbH. The switch has a minimum output pulse rise time of 50 ns depending on capacitive load. The electrode circuit with the switch will be tuned to suppress transmitted noise and transition time. Other options, which fulfill the requirements of the low rise and fall time, are (i) the NIM-AMX500-3 triple analog switch produced by CGC instruments with a rising edge of < 50 ns and a falling edge of ~ 20 ns for voltages up to 500 V, (ii) the LS-30 low-noise switch by Stahl Electronics with a rising and falling edge of about 22 ns, but a limited range of ± 15 V, so that it has to be combined with an amplifier, or (iii) the MS-F 10 fast HV switch by Stahl Electronics, with a high range of ± 2 kV and a wider rising and falling edge of 200 ns for small capacitive loads and 800 ns for high loads.

4.3.5 Cryostat

To be able to reach the desired vacuum conditions, the Penning trap system will be housed in a two-stage cryostat that will allow to cool down the trap electrodes to ~ 4 K. The 4-K cold parts will be surrounded by a shield at ~ 50 K that isolates the assembly from the room-temperature environment. The trap cryostat will be connected to two pulse tube cryocoolers to be able to achieve the desired temperatures, as illustrated in Fig. 20. Mechanical design details are given in the next section.

The cryostat will be housed and mounted in a vacuum vessel made out of AISI 316L (1.4404) stainless steel while aluminium [127] is also considered because of its lower density and thus smaller weight. Initial pump down of the vacuum system will be done with a turbomolecular pump from which the vacuum vessel can be isolated as soon as the cool down of the cryostat starts and the cold surfaces act as a cryosorption pump.
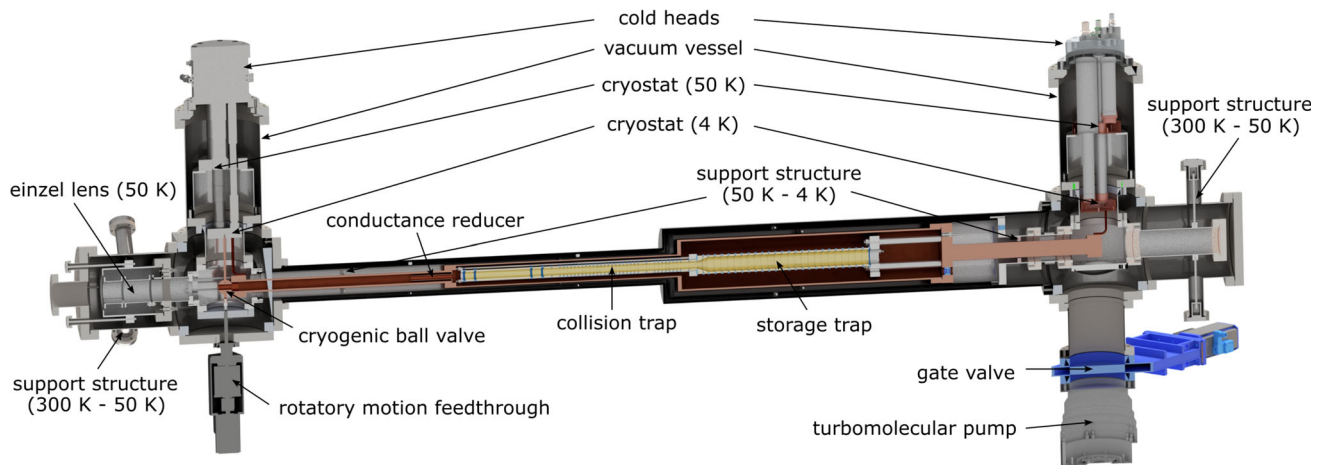
Fig. 19 Half section view of the CAD representation of the vacuum vessel, cryostat and trap arrangement of PUMA

The 45-K cryostat will consist of a cylindrical structure made of aluminium alloy [128] enclosing the entire 4-K part of the assembly to shield it from the room-temperature environment. The 45-K cryostat will be connected to both cold heads and will be supported via rods and disks (magenta and green colored pieces in Fig. 19) made of glass reinforced epoxy (G-10) [129].

Both the 45-K as well as the 4-K stage of the cold head are connected to the different parts of the cryostat using cooper braids [130]. The support of the two cryostats are designed such that, during cool down and warm up, the cylinders can expand and contract in axial direction freely, while the cryostat is rigidly fixed on the left hand side, defining the entrance position towards the Penning traps and the position of the cold shutter. The trap and 4-K cryostat are expected to contract 6 millimeters along the z axis compared to the room-temperature dimension.

The thermal calculations were carried out using COMSOL Multiphysics 5.5. A simplified version of the cryostat has been used. It includes the 4-K stage with the electrodes, the 50-K stage, and the 300-K stage. The wires connecting the 50-K stage to the electrodes have been included as 5 bundles of 20 wires of 1.14-mm radius each.

All stages are assumed to consist of Oxygen-free Copper (Cu - OFE), except for the insulating 10-mm thick G-10 half disks, the G-10 support rods and the Manganin wires connecting the electrodes at the 4-K stage to the 300 K stage via the 50-K stage. The temperature at the surface of the cryocooler cold heads (whose contact surface is included in the simulation) has been fixed to 50 K for the 50-K stage and 4 K to the 4-K stage respectively, with a total cooling power of 76 W at 50-K and 2.5 W at 4-K. The outside of the vacuum vessel is fixed to 25 °C. All touching surfaces which are screwed together will be highly polished with a mean asperity of 0.25 µm. The contact pressure is uniformly 0.2 bar. The surfaces between the G-10 support and the stages

are rougher (2 µm), and sustain a higher pressure (1 bar) due to the weight of the stages themselves. The exchange of heat in the simulation is comprised of the conduction of heat through the G-10 support and the manganin wires as well as radiation of heat caused by the large temperature difference between the 4-K, the 50-K and the 300-K stages. The radiation was modelled with the surface-to-surface radiation between the main tubes of the 300-K and 50-K stage. The emissivity of the material as well as the ambient emissivity was taken to be 0.045. All other parts of the 50-K stage are modelled with the surface-to-ambient radiation, exposed to a temperature of 293 K. Similarly, all parts of the 4-K stage are using the same module, but face a temperature of 70 K. The resulting temperature profiles for the 50-K stage, the outside of the 4-K stage and the inside of the 4-K stage, i.e. the traps, can be seen in Fig. 20. The electrodes reach a temperature of 5.11 K, the shield of the 4-K stage 5.16 K and the 50-K stage 73.6 K.

Copper braids with a cross section of 211 mm^2 connect the cold heads to the 4-K apparatus. They show a temperature gradient of 0.45 K along their length. To quantify the change of temperature of the 4-K stage, the thermal conductivity of the copper braid has been varied between its default value and three times that value, as seen in Fig. 21. The temperature of the trap can be further reduced by 0.23 K if the cross section of the copper braid connection is tripled.

The total power drawn by the 50-K stage is estimated to be 26.8 W. The power drawn by the 4-K stage is estimated at 0.46 W, thus providing enough margin with respect to the available cooling power. The predicted heat load is comparable to other setups in the literature, namely [131] which uses 6 W at the 50-K stage and 0.35 W at the 4-K stage. The 50-K stage (2917 mm) and the 4-K stage (2245 mm) contract during cooling ($\alpha_{Cu} = 1.65 \cdot 10^{-5}$/K) by 11.7 mm and 10.7 mm. Both are rigidly fixed at the upstream side by thin G-10 rods, so that they will slide on the G-10 supporting disks. The G-10 disks
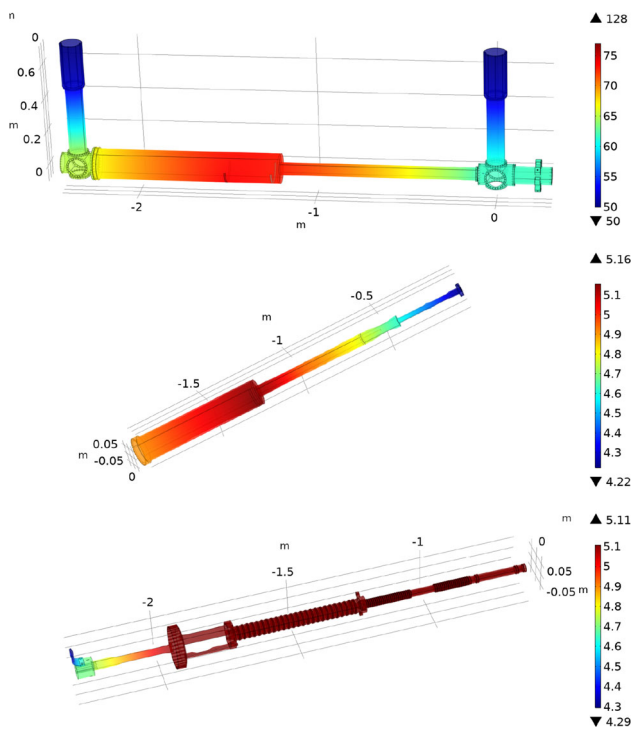
Fig. 20 (From top to bottom) Thermal profile of the 50-K cryostat, the 4-K cryostat and the inside of the 4-K stage
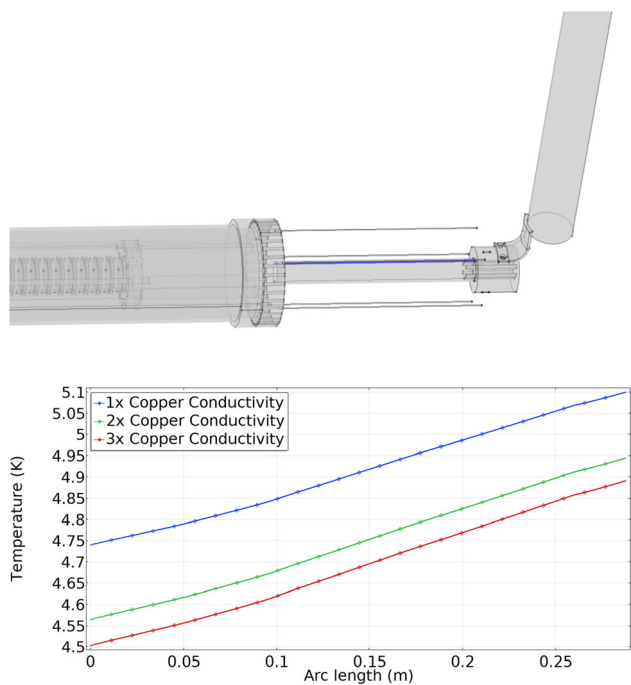

Fig. 21 (Top) Zoom on the downstream region of the 4-K stage. (Bottom) Temperature profile along the line highlighted in blue on the left panel for different conductivities of the copper used in the braids, mimicking different copper sections for the connection

($\alpha_{\text{G-10}} = 2.3 \cdot 10^{-5}/\text{K}$) between the 300-K and 50-K stage contract by 28 μm and between the 50-K and the 4-K stage by 61 μm. The system is somewhat dependent on the G-10 heat conduction. As a sensitivity test, we doubled the volume of the G-10 support: the 50-K stage reaches 79.7 K, the 4-K shield reaches 6.53 K and the electrodes warm up to 6.1 K. The power consumption then rises to 29.3 W at the 50-K stage and 0.94 W at the 4-K stage.

4.3.6 Cold shutter

To reduce the incoming flux of particles in the area around the center axis of the cryostat, a movable conductance reducer, later on called "cold shutter", will be used. This shutter has a spherical shape that can be rotated into three designated settings with a magnetically coupled rotary feedthrough. However, a cylinder-like shape or a thin tube (coated inside) will be considered as alternative geometries since, due to the thermal contraction of the shaft of the shutter, the ball-like design could require rather large tolerances at the junction to the horizontal tube. To avoid friction during rotation of the cold shutter, there will be no direct contact with the 4-K beam pipe. Unavoidably, any rotation will release some gas at the shaft base [132]. The released molecules can be efficiently intercepted by an arrangement with coaxial cold baffles around the shaft. The design of the cold shutter is ongoing and dedicated tests are planned.

4.3.7 Plasma diagnostics

To analyze the properties of the antiproton plasma without losing it, a non-destructive detection circuit will be implemented. The circuit is designed to detect the charge from the plasma induced on a pick-up electrode. It has been demonstrated that the induced signal from certain excited modes of the plasma contains useful information [133–136]. Using this diagnostics, shape, relative temperature, and number of charged particles contained in the plasma can be measured. The antiproton annihilation rate with residual gas molecules and atoms can be used to extract the number of trapped antiprotons [137]. A plastic scintillator barrel surrounding the storage trap will be used to measure the antiproton annihilation rate, and to cross-check the number of trapped antiprotons.

The non-destructive circuit is based on the following principle. The axial frequency ω_z is related to the density n and the aspect ratio α by

$$\frac{\omega_z^2}{\omega_p^2} = \frac{1}{\alpha^2 - 1} Q_1^0 \left(\frac{\alpha}{\sqrt{\alpha^2 - 1}} \right) \tag{8}$$

with the plasma frequency $\omega_p = \sqrt{\frac{nq^2}{\epsilon_0 m}}$, Q_1^0 is the (associated) Legendre function of second kind, m is the mass and q the charge of the particle.

Following [134] one can extract the plasma density n and the aspect ratio α by measuring the frequencies ω_l of the $(1, 0)$ dipole and the $(2, 0)$ quadrupole plasma mode.

In a harmonic trap, the frequency ω_1 is that of a single particle motion along the z axis

$$\omega_1 = \omega_z. \tag{9}$$

For a plasma with cyclotron frequency much higher than the plasma frequency (highly magnetised), the frequency of the dipole mode is given by the dispersion relation [138]

$$1 - \frac{\omega_p^2}{\omega_2^2} = \frac{k_2}{k_1} \frac{P_2(k_1) Q_2^{0\prime}(k_2)}{P_2'(k_1) Q_2^0(k_2)}. \tag{10}$$

P_l and Q_l^m are the (associated) Legendre functions of first and second kind, primes denote the differentiation with respect to the argument. Also

$$k_1 = \frac{\alpha}{\sqrt{\alpha^2 - 1 + \omega_p^2/\omega_2^2}} \tag{11}$$

$$k_2 = \frac{\alpha}{\sqrt{\alpha^2 - 1}}. \tag{12}$$

By measuring ω_1 and ω_2 and combining Eqs. 8, 9 and 10 one can extract the plasma density n and the aspect ratio α. The $(1, 0)$ and $(2, 0)$ frequencies (and also higher orders) do not depend on the total number of particles, but only the density n and the aspect ratio α.

To get the total number of charges N, another parameter is needed, since N satisfies the following relationship:

$$N = 4\pi n z_p^3 / 3\alpha^2. \tag{13}$$

The ATHENA collaboration developed a model for determining the total number of charged particles N in the trap [134]. A radio frequency is applied to the plasma near resonance and the response of the plasma is analysed (see Fig. 22). The width of the resonance peak, which corresponds to a quality factor of equivalent RLC circuit, is connected to the plasma properties such as the plasma length z_p.

The non-destructive diagnostics for PUMA use resonant plasma modes. To measure the plasma density n and the aspect ratio α, one has to find the frequencies ω_l of the plasma modes. A way to do this is to sweep the frequency range around the expected resonance frequency and record the response of the system.

This will be done by connecting a vector network analyzer to two of the 20 non-segmented electrodes. The network analyzer supplies a driving signal to one electrode and records the amplitude and phase of the signal induced on another
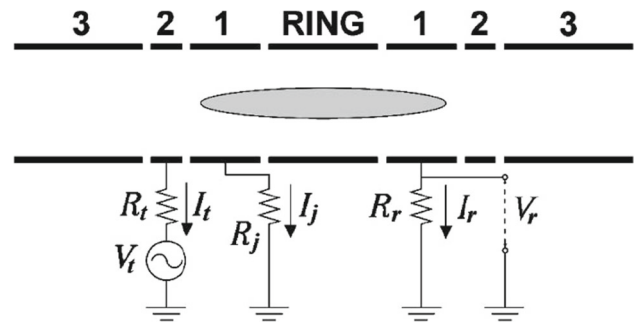

Fig. 22 The radio frequency source signal is applied to the transmission electrode and the plasma signal is picked up by the receiver electrode. R_j denotes the resistance of electrodes not used for detection. Reprinted with permission from [134] @2021 by AIP Publishing
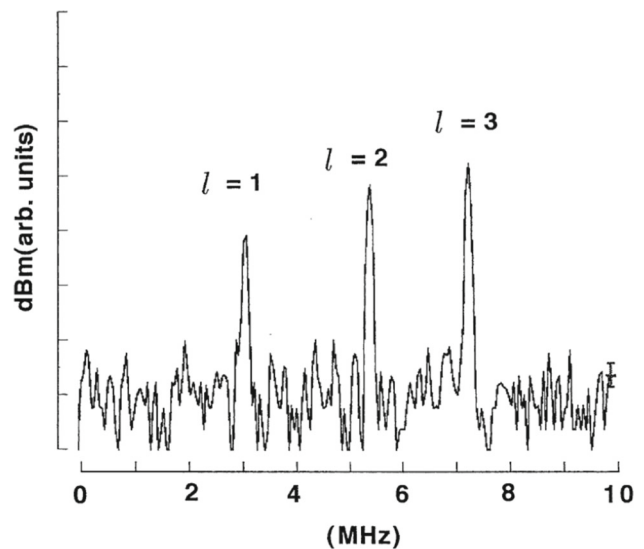

Fig. 23 The spectrum of several plasma modes. Here, three plasma modes are excited simultaneously from different electrodes. The peaks correspond to the indicated modes. Figure from [139], ©1997 The Physical Society of Japan and The Japan Society of Applied Physics

electrode relative to the driving signal. This leads to a spectrum like the one shown in Fig. 23. From the peaks one can deduce the resonance frequency.

We will use a Rohde & Schwarz Vektor Network Analyzer ZNB4 (2 ports, 9 kHz–4.5 GHz) with an extended power range down to − 80 dBm (ZNB4-B22). If needed, a 30 dBm amplifier can be connected to the pick up electrode.

The driving voltages are low ($\sim$ 100 μV) compared to the trap potential ($\sim$ 100 V). The excited motion of the plasma will therefore be small compared to the trap dimensions, and the effect of the non-destructive diagnostics on the overall evolution of the plasma can be neglected [133]. Table 5 gives frequencies for the $(1,0)$ dipole mode for particles in the PUMA trap. The values are estimated via

$$\omega_1 = \omega_z = \sqrt{\frac{qU}{md^2}} \tag{14}$$

Table 5 Estimates of the expected (1,0) dipole and (2,0) quadrupole mode frequencies for different particles

Particle	(1,0) dipole, f_1	(2,0) quadrupole, f_2
e^-	29 MHz	44 MHz
p, $\bar{\text{p}}$	670 kHz	1 MHz
He^+	335 kHz	500 kHz

with the on-axis potential $U = 250$ V and characteristic trap size $d^2 = 1.35 \times 10^{-3}$ m^2. Rough values for the (2,0) quadrupole mode can be obtained by looking at the solution of the dispersion relation (Eq. 10). The ATRAP collaboration developed a similar approach to measure the total number of charges with resonant plasma modes [135].

To benchmark the non-destructive diagnostics and to characterized the cooling and trapping techniques, a MCP will be used in the test set-up at TU Darmstadt.

4.3.8 Cold field-emission electron source

An electron source is needed for PUMA to cool the antiprotons. Electrons can also be used to test the basic operations of the trap offline without using antiprotons.

To produce the electrons, a cold field-emission electron source will be used. Such an electron source was first proposed by Crewe et al. in 1968 [140]. In contrast to conventional electron sources that produce electrons via a hot filament, a field emission electron source does not introduce a heat source into the cryogenic environment. This is important as the PUMA trap will be cooled to 4.2 K. In return, the cold field emission requires ultra high vacuum in the order of 10^{-9} mbar, already provided in the PUMA design. To emit an electron out of a metal surface, the electron has to be given energy at least equal to the corresponding work function ϕ of the metal. In an electron source with a hot filament this is provided via thermal energy. To use field emission, a sufficient voltage is applied between a sharp point of the metal and an extraction electrode, so that the potential drops outside the metal. This makes it possible for the electrons to tunnel out of the material.

The sharp point is called a field emission point. We produce field emission points by electrochemical etching with a method adapted from [141]. For this, a 0.25 mm diameter tungsten wire is threaded through a pin hole in a copper cathode. The basic solution used for the electrochemical etching is a 1.5 mol/L NaOH solution. When we apply a current of 150 mA, tungsten is removed at the position of the pin hole until the tungsten wire drops down. This leads to a very fine point at the end of the tungsten wire. Figure 24 shows an example. Field emission points produced this way were tested by applying a voltage between the tip and a plate acting as a Faraday cup 10 mm away.
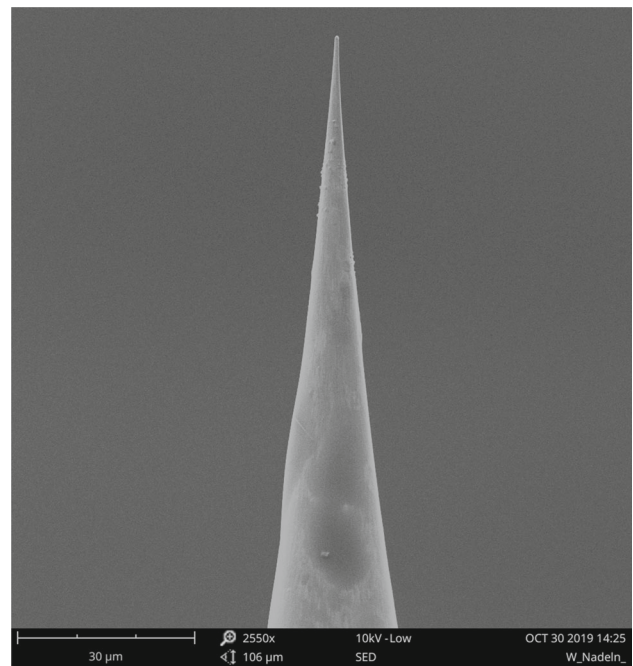

Fig. 24 A field emission point imaged with a scanning electron microscope. Note the scale in the bottom left corner

We were able to fabricate field emission points from which we extracted up to 2 μA with a voltage as low as 1.5 kV. The current was externally limited as not to damage the tip by drawing too much current. A current of 1 μA corresponds to roughly $6 \cdot 10^{12}$ electrons per second. This is sufficient to fill the trap with electrons for sympathetic cooling (see Sect. 4.4). First long-term tests show that a current of around 0.1 μA can be extracted for several hours without degradation of the field emission point [142].

4.4 Plasma manipulation

To trap and to store up to 10^9 antiprotons at ELENA and perform experiments with them together with radioactive ions at ISOLDE, a dedicated scheme for the manipulation of the incoming and already confined antiproton ensemble is to be developed. This scheme is divided into an antiproton trapping and manipulation cycle at ELENA and a cycle for the mixing of ions with a fraction of the stored antiprotons at both ELENA (stable) and ISOLDE (radioactive) optimized for annihilation. A large number of charged particles confined in a Penning trap bears properties of a non-neutral plasma [143]. PUMA will rely on the well-established rotating-wall technique to control the plasmas [111,115,144–146]. This technique uses a sine wave applied to a radially segmented electrode, which is seen from trapped particles as a rotating multipole field, to compress the particle cloud. The rotating-wall technique has been successfully extended to a multi-species non-neutral plasma containing antiprotons and elec-

trons [112,147]. In case of a multispecies non-neutral plasma, additional difficulty of centrifugal separation [112,148] and, for large particle numbers, diocotron instabilities must be dealt with. Simulation studies are in progress to estimate plasma instability thresholds and to control or avoid any limiting plasma instabilities.

The rotating-wall technique is used to compress radially the antiproton cloud. Still, it cannot avoid a temperature rise from contributions such as interaction with residual-gas molecules and non-harmonic field components. Sympathetic cooling of the antiprotons with self-cooling electrons will compensate radial expansion over time. The selection of a subpart of a non-neutral plasma and its adiabatic transfer in another part of the trap has been developed and benchmarked [149]. Trapping oppositely charged antiprotons and ions will be realized by use of a nested potential. Such scheme has been developed to trap particle and antiparticle simultaneously [150,151]. A design of the storage trap will be discussed to perform the series of operations with sufficient degree of freedom. Most methods considered here have been developed in the context of former or existing AD experiments, such as ASACUSA, BASE, AEḡIS, ALPHA and ATRAP and PUMA will immensely benefit from these earlier developments.

4.4.1 Antiproton capture and storage at ELENA

The trapping and manipulation cycle of the antiprotons in PUMA is constrained by the time interval of about 110 s [63] between two consecutive antiproton bunches. That is the time which ELENA needs to provide a cooled, 100 keV antiproton bunch. Within this time interval, the incoming bunch of several $10^6 - 10^7$ antiprotons (depending on the spill sharing at ELENA) has to be captured, cooled and shaped in the storage region of the PUMA trap setup. The typical energy of the particles behind the two pulsed drift tubes will be in the order of about 200 eV or less, which translates, together with the rms bunch length of 75 ns, to a total geometrical bunch length l_{bunch} of about 8.8 cm (3σ-) and maximum antiproton velocity v_{bunch} of about 200,000 m/s. Considering an effective capture volume with a length l_{cap} of ~ 15 cm, the switching time for the downstream potential has to be shorter than

$$t_{max} = 500 \, \text{ns}.$$

Consequently, the required switching time should be below 200 ns with a sufficient safety margin, to be provided by solid state switches.

Prior to the first capture of antiprotons, the trap is filled with electrons, which will act as a cold buffer for the incoming antiproton bunch. As the electrons emit cyclotron radiation based on the Larmor formula in the strong 4 T magnetic field, they cool down exponentially to ambient temperature

[151], i.e. the cryogenic trap temperature of about 4.2 K, with a time constant τ_s given by:

$$\tau_s = \frac{6\pi\epsilon_0 mc^3}{e^2\omega_c^2} = \frac{6\pi\epsilon_0 m^3 c^3}{e^4 B^2} \approx 0.3 \, \text{s} \quad \text{for} \quad B = 4 \, \text{T.} \quad (15)$$

If a bunch of antiprotons is then captured within the cold electron buffer, the antiprotons will be cooled indirectly by sympathetic cooling, as they lose energy by Coulomb collisions with electrons. The electrons heat up in these collisions, but due to the emission of cyclotron radiation they rapidly cool down again. Within a timescale of a few seconds [112], depending on the relative density of antiprotons and electrons, the antiprotons and the electrons thermalize and reach a temperature close to the ambient temperature in absence of heating mechanisms. However, after the first bunch is trapped and cooled by the electrons, the second incoming bunch will not only heat the electron fraction of the stored particles, but also the previously cooled antiprotons [108]. This re-heating of the stored antiprotons has to be taken into account for the definition of the required number of electrons for sufficient cooling, as the total cooling time down to 4.2 K is assumed to increase slightly with each incoming bunch. Due to internal heating mechanisms in the real setup compared to the ideal case, the actual number of electrons has to be even higher. These sources of heating originate from a misalignment of the electric and magnetic field, giving rise to higher order field components. To compensate for the induced heating, based on the experience of other antiproton experiments at ELENA, a number of about $5 \cdot 10^8$ electrons is foreseen for the first tests.

One type of intentional particle excitation that is required for the PUMA is the rotating wall technique [111,112,115, 144–147]. This technique is based on a rotating dipole- or quadrupole-field, which is applied by using the 4- or 8-fold segmented electrode, respectively. It requires a sufficiently dense ensemble of trapped particles, so that this can be described as a non-neutral plasma with a Debye length $\lambda_D = \sqrt{\epsilon_0 k_B T / nq^2}$ as a function of the ensemble temperature T and the density n that is small compared to the typical dimensions of the particle ensemble [152]. In contrast to the single particle framework, where such rotating multipole fields are used for the excitation of the radial eigenmodes, the rotating wall technique allows to regulate the radial expansion of the trapped non-neutral plasma. This is necessary for the long term storage of trapped particles, because the higher order field components of the misaligned electric and magnetic field tend to increase the ensemble radius over time.

The control of the radial expansion of the trapped antiprotons is necessary to avoid annihilations on the trap electrodes, which lead to the production of energetic particles that could interact with the remaining trapped particles, causing a cas-

cade that eventually leads to a loss of all antiprotons within seconds.

To summarize the above, the full scheme for the accumulation of 10^9 antiprotons can be divided into the following steps:

– fill the storage region with about $5 \cdot 10^8$ electrons provided by the cold field emission source and let them cool down for several seconds,
– turn on the rotating potential on the segmented electrodes for the application of the rotating wall field,
– trap the decelerated antiproton bunch by fast switching of the upstream electrode of the storage region within the cold electron buffer,
– let the antiprotons cool down by sympathetic cooling with the electrons,
– keep the trapped antiprotons within the reservoir of electrons which continuously compensates the heating induced by the rotating field.

After all bunches of antiprotons are captured within the storage region of PUMA at ELENA, the long term storage of the antiprotons is ensured by a continuous application of the rotating wall technique and of sympathetic electron cooling. This state is also kept during the transport of the PUMA setup to ISOLDE and during the operation at ISOLDE as well. Note that the power of the rotating wall, frequencies and number of electrons mixed with the antiprotons can be modified during transport to counterbalance the eventual excitations due to vibrations during handling. As detailed in Sect. 4.3.7, the plasma will be continuously and non-destructively diagnosed, allowing a real-time feedback on the trapping parameters.

4.4.2 Formation of antiprotonic atoms

In the following, the possible options foreseen to mix antiprotons and low-energy ions at ELENA (stable ions) and ISOLDE (radioactive ions) are presented. The challenges to be overcome by a dedicated R&D are highlighted. The strategy to address these aspects of the PUMA experiment is given in Sect. 6.

To perform annihilation experiments with nuclei, a fraction of the stored antiprotons is extracted adiabatically from the storage region into the collision region of the PUMA setup [149]. During the extraction of the antiprotons from the storage trap to the collision trap all electrons will also be extracted, as their axial frequency is much higher. The extracted fraction of antiprotons and electrons are then stored within the collision region of the trap. The loss of electrons from the storage region has to be compensated by re-filling electrons into it either from inserting back the previously removed electrons or from the cold field emission source.

The arrangement of electrodes is chosen to maximize flexibility. A preparation zone is foreseen between the collision and storage trap. This zone could be in principle used for an extraction of electrons from the collision zone or for the preparation and cooling of additional antiprotons or electrons to be introduced to the collision zone.

At this stage of the project, we are considering two ways to produce antiprotonic ions by mixing the antiprotons either with negatively-charged ions or positively-charged ions. Thanks to the second pulsed drift tube integrated in the trap tower, the ions will be inserted with a kinetic energy of few tens of eV in the collision zone.

The capture rate of trapped ions can be defined as

$$R = n_{\bar{p}} \sigma_{\text{capt}} v N_i \tau, \tag{16}$$

where $n_{\bar{p}}$ is the antiproton density in the plasma, σ_{capt} is the capture cross section at the relative velocity between ions and antiprotons, v is the velocity of ions in the antiproton plasma, N_i the number of trapped ions and τ the overlap of trapped ions with antiprotons (in space and time). In PUMA the density of ions is expected to be 10^{-4}-10^{-2} of the density of the antiprotons. To some extent, the ions can be considered as single particles interacting with the antiproton plasma.

At low energy, the capture cross section evolves as a function of $1/v$. Assuming, for a first estimate, that the antiprotons are cooled down and that the relative velocity is given by the laboratory velocity of the ions, it is interesting to notice that the rate of Eq. (16) does not depend on the ion velocity: the velocity dependence of the cross section is compensated by the effective number of antiprotons "seen" by the ion. If one considers the case of ^{132}Sn at a kinetic energy of 20 eV and 10^5 trapped ions, overlapping at 20% with an antiproton cloud of density 10^7 cm^{-3}, and a cross section of 100 a_0^2, a conservative value compared to the predictions of Cohen (see Fig. 25), one gets a rate of R = 160 Hz.

Introducing negative ions (see Sect. 7.3.2) into the $\bar{p}$-plasma has the advantage of simplifying the mixing scheme of the ions with antiprotons in the collision zone. Antiprotons will be kept cooled via sympathetic cooling and compressed by applying the rotating wall technique. The modification of the rotating wall parameters will allow to adjust the size of the antiproton cloud to the initial ion spatial distribution if necessary. An increased rotating-wall (RW) power while ions and antiprotons are mixed should increase the overall density and therefore the integrated capture rate.

One may wonder if the Coulomb repulsion between antiprotons and negative ions can hinder the capture probability. The minimum distance approach $d_{\bar{p}A}$ of an antiproton of velocity v from a negatively-charged ion is given by

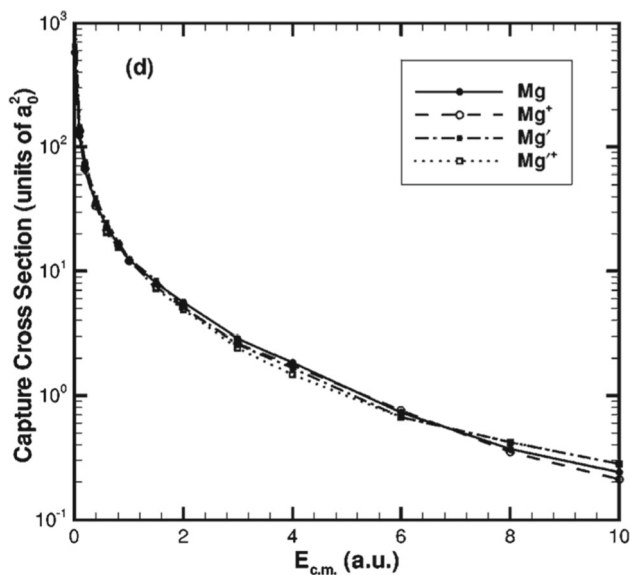$$d_{\bar{p}A} = \frac{e^2}{4\pi\epsilon_0} = 1.44 \times 10^{-9} \text{ eV m.} \tag{17}$$

Fig. 25 Predictions of antiproton capture cross section on ^{21}Mg (neutral and in $q = +1$ ion state) as a function of center-of-mass energy at low energy. Reprinted with permission from [68], ©2004 by the American Physical Society

The radii of most atoms are from a few 10^{-11} to $2 \cdot 10^{-10}$ m, meaning that a few 10 to 100 eV relative kinetic energy needs to be maintained in order to authorize a sufficient penetration of the antiprotons inside the electron cloud of a negatively-charged ion. After entering the electron cloud, the antiproton would experience a net positive electric charge from the nucleus, allowing a capture process to occur.

It is expected that the ions and the antiprotons equilibrate in temperature when mixed together. The exact timescale of this cooling depends on several parameters: (i) the electron and antiproton densities involved, (ii) the initial kinetic energy of the trapped ions and (iii) the initial temperature of the electron and antiproton cloud, but the time constant for the sympathetic cooling based on electrons is typically in the order of seconds or tens of seconds [153–156]. In the case of the most short-lived nuclei, this cooling time will exceed the half life of the radioactive isotopes (RI) and the radioactive decay products will exit the trap, or be removed, before an equilibrium temperature is reached. In the case of longer-lived isotopes, the relative energy of antiprotons and negative ions will be maintained by an axial RF excitation of the plasma. The frequencies of the excitation will be chosen to (i) optimize the annihilation rate, (ii) minimize the antiproton loss. A dedicated series of tests will be performed at ELENA for that purpose.

The full scheme of overlapping the negative ions with the antiprotons in the collision trap can be divided into six steps, as depicted in Fig. 26. The center of the z-axis, i.e. the location where the antiprotons and negative ions will overlap, corresponds to the axial center of the TPC, corresponding to

a maximum geometrical acceptance of the detector. All these steps will be benchmarked with antiprotons and stable ions within the first months of PUMA at ELENA.

1. **Transfer and capture of p̄**: A fraction of the antiproton cloud is adiabatically transferred from the storage trap into the collision trap. In addition to the $\sim 10^7$ antiprotons, all electrons from the storage trap will be transferred. The potential well to trap the mixed antiproton-electron ensemble is located at the center of the collision trap.

2. **Cooling of p̄**: After the antiprotons entered the trap a second potential well is pulsed to trap the ensemble within the downstream half of the collision trap. This location of temporary storage minimizes the impact of the capture process of the short-lived ions on the stability of the p̄ ensemble. Within seconds after the trapping, the self-cooling electrons cool down sympathetically the antiprotons while continuously applying a RW drive.

3. **Capture of negative RI**: After the deceleration of the negative ions in the pulsed drift tube upstream of the collision trap to energies of about 20–100 eV, the ions are then stopped with a sufficiently high potential well in the upstream half of the collision trap.

4. **Trapping of negative ions and p̄**: To trap the negative ions in the upstream half of the collision trap, a second potential well is pulsed at the upstream end of the trap. By this, both the ion bunch and the antiproton ensemble are trapped within the collision zone without spatial overlap.

5. **Overlapping negative ions and p̄**: The ions are adiabatically transferred to the antiproton cloud by ramping down the separation potential, until both species are trapped in a unique potential well, leading to an efficient spatial overlap. At this stage, the electrons cool down the heat induced by the hot ions, reducing the relative velocity of ions, antiprotons and electrons. The number of electrons in the mixed plasma is a parameter to be optimized during the first measurements at ELENA.

6. **Interaction of negative ions and p̄**: As a sufficiently high relative velocity of the ions and antiprotons is required for the antiproton capture process, an optional axial auto-resonant RF excitation of the ions is foreseen [157]. This excitation optimizes the relative velocity to maximize the capture cross section while aiming at minimizing the impact on the antiprotons, thus avoiding losses of antiprotons. A dedicated series of tests to identify suitable frequencies and amplitudes of the drive is part of the R&D program. Furthermore, the lifetime of the negative ions is limited by electron detachment processes which would lead to the formation of neutral atoms, leading to a loss. A quantification of the detachment rate will be performed. Associated measurements with negative ions inserted in a proton plasma or an electron plasma will be performed at TU Darmstadt.
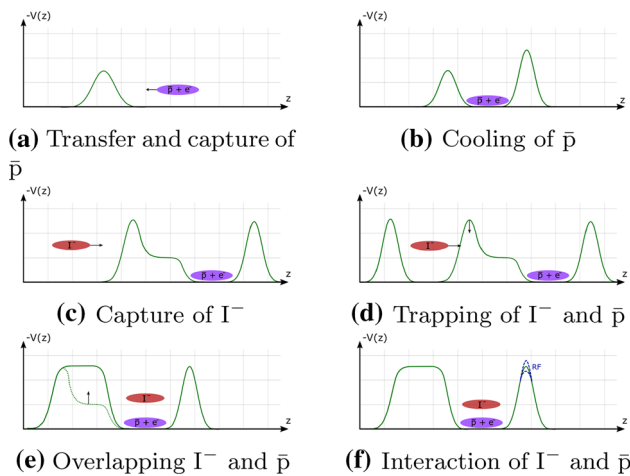
(a) Transfer and capture of p̄

(b) Cooling of p̄

(c) Capture of I⁻

(d) Trapping of I⁻ and p̄

(e) Overlapping I⁻ and p̄

(f) Interaction of I⁻ and p̄

Fig. 26 Interaction scheme for negative ions (I⁻) and p̄

Ions at ISOLDE are favorably produced with charge $q = +1$. As the ions and antiprotons have opposite charges, a nested potential is needed for the simultaneous trapping of both species. In the case of PUMA, it is important to limit the loss of antiprotons as much as possible. The antiprotons will be trapped with electrons in the center of the collision trap. The ions will be prepared so that they "cross" the antiproton cloud with maximum overlap.

At this stage of the project, the number of electrons to be stored with the antiprotons during the mixing process is still an open question. On one hand, a large number of electrons would allow a cooling of the antiprotons. In this particular case, there will be a competition between the antiproton capture, our objective, and the recombination with a free electron [158], resulting in the loss of the neutral ion. The latter process depends strongly on the energy and density of the free electrons and occurs on a typical timescale in the order of a few seconds after the ions are overlapped with the antiproton-electron ensemble (see Fig. 27). The suppression of the recombination process in the first seconds is caused by the significant electron heating induced by the hot ions, which effectively reduces the cross section for a radiative recombination [159]. On the other hand, the electrons within the collision region could be extracted by fast switching. By this, a pure reservoir of antiprotons could be prepared in the collision zone, into which the ions are injected. The absence of electrons will lead to a rapid excitation and heating of the antiproton cloud and a loss of antiprotons which should be prevented. One could consider to alternate between phases with electrons for cooling and phases with a lesser number of electrons, if recombination appears to be an issue. The above schemes will be tested and optimized within the first months at ELENA.

Y=N

After the capture, the short-lived ions and the antiprotons are simultaneously stored in the collision region with a spatial overlap that allows for interactions of both species. Assuming the case where the antiprotons and electrons are stored within the negative potential well (compare Fig. 28), this spatial overlap is limited by the sympathetic electron cooling of the ions, which will cause losses of ions in the potential wells next to the negatively charged ensemble on a timescale of seconds [154,155]. To overcome these losses, an axial RF excitation is foreseen, which will keep the energy of the ions high enough to overlap with the antiprotons. Here, the frequencies of the excitation will be chosen to (i) optimize the annihilation rate and spatial overlap and (ii) minimize the impact on the stored antiprotons. For that, a dedicated series of tests with stable ions will be performed at ELENA.

Depending on the lifetime of the ions, the time of simultaneous storage and interaction will be defined to avoid significant contamination of the surface annihilation signals that PUMA is interested in. After this time interval, the ions are dumped upstream of the collision zone, while the remaining antiprotons are transported back into the storage zone of the PUMA trap.

We describe, schematically, the possible steps of a full mixing cycle of positive ions and antiprotons. The mixing of plasmas of opposite charges has been developed in particular at the Antiproton Decelerator (AD), focusing on antiprotons and positrons to form antihydrogen [160–162].

1. **Transfer and capture of p̄**
2. **Cooling of p̄ and trapping of p̄**: After the cooling process the antiprotons and electrons are trapped within a shallow positive potential well with a depth of just a few tens of volts. This is necessary to avoid significant losses of ions when overlapping the antiprotons with the positive RI. The RW field is applied to the mixed ensemble.
3. **Positive ion capture:** After deceleration in the pulsed drift tube the positive RI are stopped within the upstream half of the collision trap by a positive stopping potential. Due to the spatial separation, no initial heating is induced into the cold antiproton ensemble. By pulsing a second potential well at the upstream end of the collision trap, the RI are then trapped within the upstream half of the trap.
4. **Transferring the I⁺ to the p̄**: To initialize the overlap, the ions are transferred towards the p̄ cloud. The potential well which separates the positive ions from the antiprotons is lowered to zero.
5. **Mixing I⁺ with p̄:** Both clouds are spatially overlapped at the location of the nested potential defined by two negative wells at both ends, which avoid axial antiproton losses. The optimum height of these wells needs to be fine tuned: deep wells minimize antiproton losses but will increase the field gradient seen by the ions when approaching the
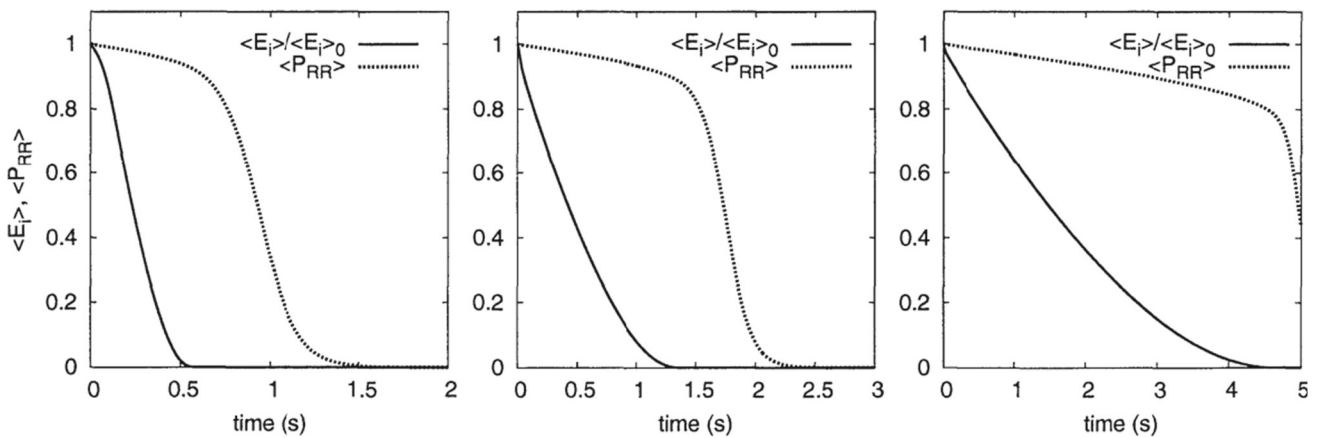
Fig. 27 Average ion energy E_i/E_{i_0} and surviving probability P_{RR} as a function of time for an ensemble of bare uranium ions sympathetically cooled by electrons with $T_e = 4\,\mathrm{K}$, $n_e = 10^7\,\mathrm{cm}^{-3}$, $B = 6\,\mathrm{T}$ and different uranium ion densities of $n_i = 10^2\,\mathrm{cm}^{-3}$ (left), $n_i = 10^3\,\mathrm{cm}^{-3}$ (center) and $n_i = 10^4\,\mathrm{cm}^{-3}$ (right). Reprinted with permission from [159] @2020 by AIP Publishing

sides of trapping region, further converting axial kinetic energy into radial kinetic energy. Note that the side wells can be used for dumping electrons out of the central nested well. By pulsing the shallow well on a timescale of less than a microsecond, in principle all electrons could be removed, while the antiprotons remain mostly unaffected [163].

6. **RF heating of RI:** While both clouds are overlapped, the ions are continuously sympathetically cooled by collisions with electrons and antiprotons. Over time, this cooling might cause losses of ions in the shallow potential well on the left and right-hand side of the central antiproton-electron well, reducing the spatial overlap of ions with antiprotons and thus reducing the rate of events. The typical timescale for this cooling process and the subsequent spatial separation is in the order of seconds [155], which is longer than the lifetimes of most short-lived ions in the trap. This cooling time needs to be determined in PUMA's experimental conditions to decide how much attention should be paid to overcome this axial separation of ions and antiprotons. In case of ions with a longer lifetime, an additional optional axial RF excitation of the ions is foreseen, which keeps the ions at sufficient energy to overcome these shallow potential wells and minimizes the impact on the antiprotons. When locked to the drive, an option pointed out by S. Ulmer (BASE), the bounce frequency of the ions could be tuned precisely to the desired axial energy of the ion, i.e., the excitation with respect to the antiproton nesting potential [157]. A dedicated series of tests to identify suitable frequencies and amplitudes of the drive as well as determining the impact of such a drive on the radial overlap of the two species is part of the R&D program.
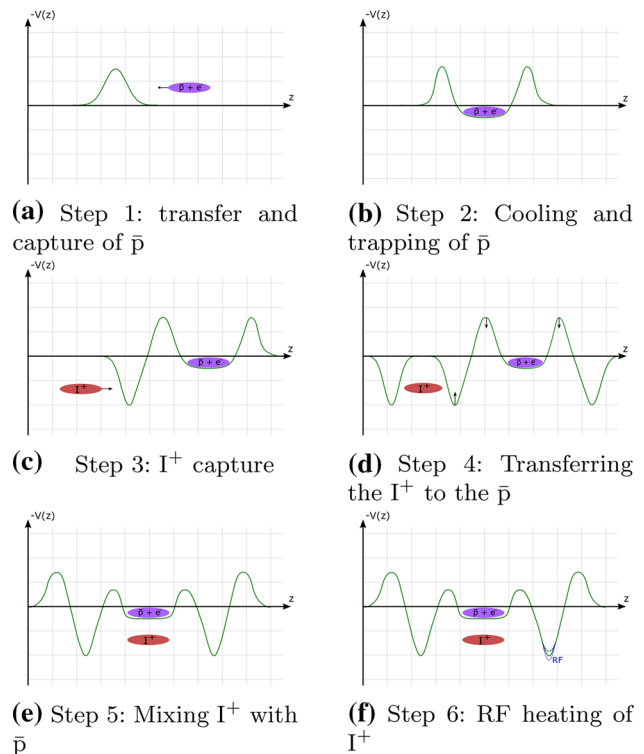

(a) Step 1: transfer and capture of $\bar{p}$

(b) Step 2: Cooling and trapping of $\bar{p}$

(c) Step 3: I^+ capture

(d) Step 4: Transferring the I^+ to the $\bar{p}$

(e) Step 5: Mixing I^+ with $\bar{p}$

(f) Step 6: RF heating of I^+

Fig. 28 Interaction scheme for positive ions (I^+) and $\bar{p}$

4.4.3 Antiproton losses

We emphasize the importance of reducing the antiproton losses in the collision zone, since the number of trapped antiprotons will be limited for measurements at ISOLDE. An acceptable rate of losses is below $100\,\mathrm{s}^{-1}$ when ions are inserted inside the antiproton cloud. $100\,\mathrm{s}^{-1}$ is significantly below the rate capabilities of the TPC readout. It would be an acceptable loss of antiprotons for the foreseen experimental

cycle at ISOLDE: typically a day of measurements before the need to refill the collision zone with a new load of 10^7 antiprotons.

Radial losses in the collision zone will be unambiguously separated from annihilation events from ions inserted in the trap by the vertex tracking capabilities of the detection ($\sigma < 1$ mm, see Sect. 4.5, below).

4.4.4 Ion removal from collision trap

The ejection of ions from the antiproton cloud can be performed in several ways.

In the particular case of radioactive nuclei, ions can decay while trapped. In this case, the new isotope will be naturally removed from the collision zone by the recoil energy gained from the beta decay. A typical β-decay Q value is few MeV (e.g. 3.1 MeV for the β^+ decay of ^{132}Sn, 15.6 MeV for the β^- decay of ^{17}Ne), leading to a recoil energy of the daughter nucleus much larger than the few hundred eV of the axial confining electrical potential. In the case a 1 MeV recoil energy is transmitted to the axial direction, it corresponds to a trajectory radius in the 4 T field of the solenoid of ~ 20 cm (e.g. 42 cm for ^{132}Sn, 15 cm for ^{17}Ne), significantly larger than the 2-cm radius of the collision trap. In conclusion, the recoil nucleus following a β decay in the collision will exit the trap, and the ions mixed with the antiprotons will remain isotopically pure. The recoil nuclei following an annihilation will also most often exit the trap due its recoil momentum, equal to the intrinsic momentum to the annihilated nucleon under the sudden and core-spectator approximations.

In the case of stable or long-lived ions, one could in principle keep them inside the antiproton cloud until a capture occurs, followed by annihilation. In this particular case, they might also capture an electron and leave the plasma as neutral particles.

Finally, in the case of negatively charged ions and antiprotons, the separation can occur by centrifugal separation [162,164]. The separation takes place at low temperature when the condition

$$|\frac{m_i}{q_i} - m_{\bar{p}}|\omega_r^2 R_p^2 \geq k_B T \tag{18}$$

is met. In the above inequality, m_i is the mass of the ion, q_i its charge (+ 1, here), $m_{\bar{p}}$ the mass of the antiproton, ω_r the rotation frequency of the plasma, R_p the plasma radius, T the temperature. The timescale of the drift of ions inside an antiproton plasma is much longer than the typical cooling time [165]. The centrifugal separation can be avoided by manipulating the plasma with the RW technique and keeping the temperature relatively high by exciting the plasma, either by white noise or at specific frequencies away from collective-mode frequencies.

4.5 Pion detection

4.5.1 Overview

The pion detection of PUMA has two objectives: to determine the positively and negatively charged pion multiplicities after capture and annihilation from nuclei of interest, and the diagnosis of the stored antiproton cloud from annihilation with residual gas molecules. To achieve these goals we developed a tracking detection system, positioned inside the 4–Tesla PUMA solenoid. The signals are transported via low capacitance cables to a common data acquisition system with the front and back end electronics being located outside the magnetic field. The detection system consists of a time-projection chamber around the collision trap, surrounded by a plastic-scintillator barrel, read out by Silicon Photomultipliers (SiPMs).

After the annihilation takes place in the collision trap, energetic pions are produced. The charged particles traverse the gas volume of the TPC and ionize the atoms of the gas mixture along their trajectory. The released electrons drift towards the anode plane driven by an electric field applied between the endplates of the TPC. At the anode plane, the electrons are amplified and induce a signal on the readout pads. The track projection on the pad plane and the drift times measured for each individual pad allow one to reproduce the charged particle tracks throughout the detector.

The plastic barrel will be also used to estimate the vacuum inside the storage and collision zones from the monitoring of the antiproton decay rate caused by the interaction with the residual gas. An additional monitoring system around the storage zone might be considered at a later stage of the experiment.

4.5.2 Geometry and simulations

Simulations based on the Geant4 toolkit [166] have been carried out in order to optimize the geometrical acceptance and the detection efficiency, using the ROOT framework [167] for the analysis of the data. They consist of three main blocks:

– The detector and the generation of the pions corresponding to realistic annihilation events occurring in the trap are simulated. Each event produced in the simulation consists of a set of pions randomly generated according to the appropriate branching ratios of antiproton–neutron [84] and antiproton–proton [168] annihilations. The total kinetic energy that satisfies energy conservation is isotropically shared among final–state pions. Figure 29 presents a typical event in the collision trap surrounded by the TPC and the plastic barrel.
– The drift of the ionization electrons towards the pad plane considering the transport parameters (drift velocity, lon-
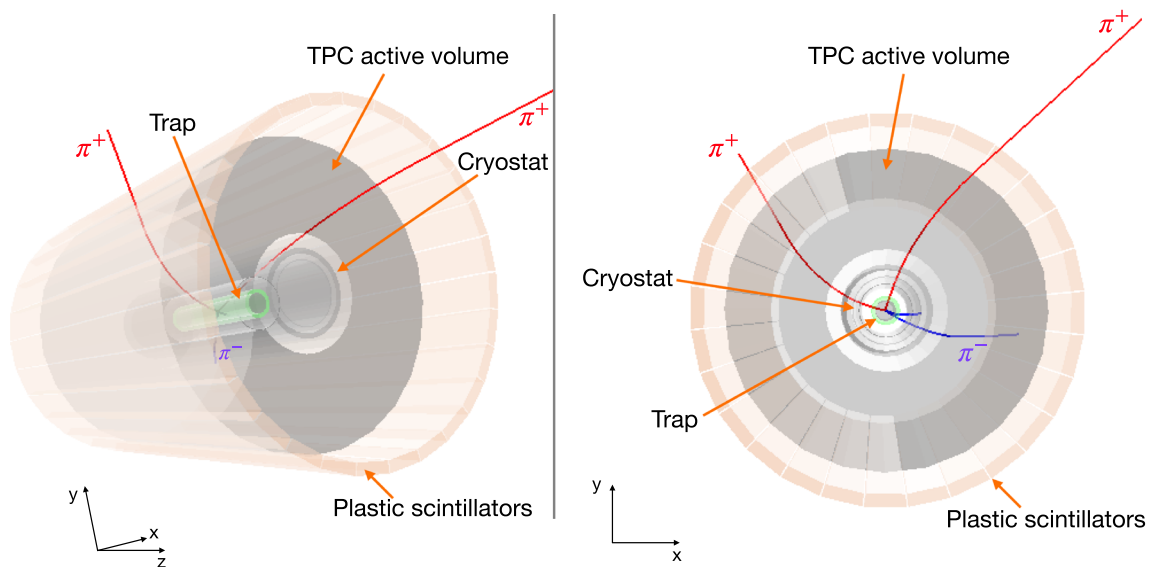
Fig. 29 Typical event simulated with the Geant4 toolkit. The blue line corresponds to a π^- and the red ones to π^+

gitudinal diffusion and transverse diffusion) is computed with MAGBOLTZ [169] in the conditions of the experiment for different gas mixtures. At this stage the response of the electronics system is also simulated. The model used was developed for the MINOS experiment [170] and was extensively benchmarked with data (see for example [171]).

– The identification of the vertex and the charge of the pions by the bending of the tracks in the magnetic field [170,171] is computed using the MINUIT tool with the MIGRAD minimizer [172].

The optimal geometry of the TPC for the purpose of the experiment was chosen by varying three main parameters: the TPC external radius R, its length L and the pad plane layout.

We define the total efficiency as

$$\varepsilon_{tot} = \varepsilon_{TPC} \cdot \varepsilon_{ID},$$

where ε_{TPC} corresponds to the ratio of the number of charged pions that deposited energy in the TPC with respect to those that were generated in the trap (in other words, they were within the TPC's geometrical acceptance and not absorbed by the surrounding materials). The identification efficiency ε_{ID} is the ratio of the number of particles whose charge was correctly identified by the analysis algorithm over the total number of tracked pions.

The simulations were performed for 1500 events, corresponding to roughly 3500 pions. The material which the trap is made of as well as the rest of the components surrounding the trap (see Sect. 4.3.5) were simulated. A point-like annihilation vertex at the center of the trap was considered.

The TPC inner (mechanical) radius R_{int} = 53 mm is fixed by the dimensions of the trap and the 4 K cryostat. Taking the space needed for the field cage, the internal radius of the active volume is set to 66 mm. Simulating the detection efficiency as a function of its outer radius is relevant for the evaluation of the dimensions of the plastic barrel as well as the size of the magnet's bore.

Figure 30 displays the efficiencies ε_{tot} (triangles), ε_{TPC} (squares) and ε_{ID} (circles) obtained, considering a length L = 300 mm. The red curve (squares) corresponds to the aforementioned ε_{TPC} which, as expected, remains constant. The absorption probability of a pion depends only on the materials the particle traverses during its path towards the sensitive gas of the TPC, and the geometrical acceptance only depends on its length. An increase is observed on the charge identification efficiency ε_{ID} (circles) due to an increase of the track length as the radius enlarges. A plateau is reached at R∼110 mm, which determines the active volume external radius.

Figure 31 presents a sketched 3D view of the pion detection system for the collision zone around the XHV tube. The TPC is a 300 mm long cylinder, 53 mm internal radius and 110 mm external radius, filled with ionizing gas, where a uniform electric field of about 200 V/cm is applied (according to the choice of the gas).

Two flanges at either end of the setup will accurately set the plastic scintillators in position. Table 6 shows the list of materials and thicknesses of the components that the charged particles traverse upon reaching the detector. From this list, the total radiation length experienced by a particle traversing the system with a minimum trajectory (in the radial direction from the center of the collision trap) is 2.3 cm, whereas
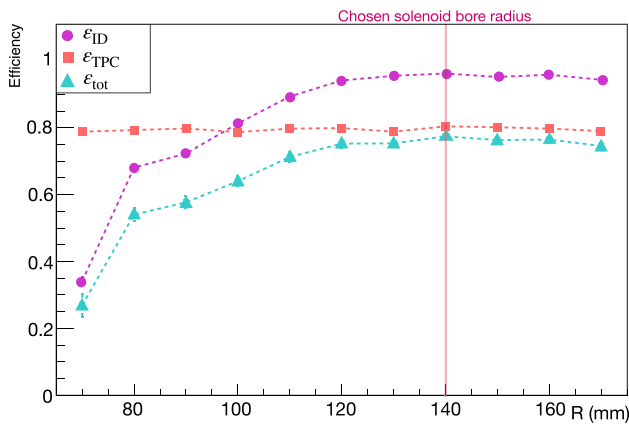
Fig. 30 Efficiencies ε_{TPC} (squares): Ratio between charged pions within the TPC's geometrical acceptance and total charged pions simulated. ε_{ID} (circles): Ratio of the number of pions whose charge was correctly identified by the analysis software over the total number of tracked pions. ε_{tot} (triangles): Product of the former two. Variables plotted as a function of the external radius of the TPC. The error bars (represented by the size of the points) correspond to statistical uncertainty from the simulation
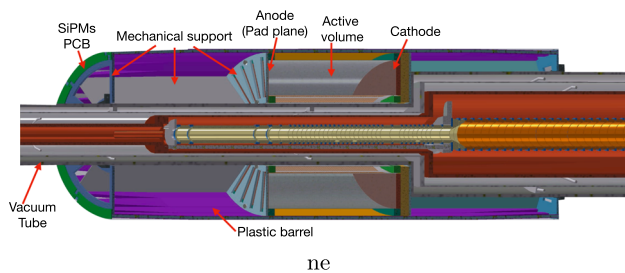
Fig. 31 Cut view (half is shown) of the proposed setup CAD model and mechanical support of the detection system in the collision zone

the radiation length is 1 cm for a particle with a maximum trajectory inside the system.

For the amplification of the signal, a Micromegas detector is employed. It will have a low impedance grounding circuit to the mesh, a resistive layer (DLC Diamond Like Carbon) biased to a maximum of 500 V and the grounded pad plane. The pad plane, together with the field cage structure, have been conceived to be mechanically stable and electrically homogeneous.

Both PCB plates holding the anode an cathode are shaped in a 32-faced polygon, which support the plastic scintillator bars.

The 11-mm-thick cathode, biased at -6 kV, presents a sparking risk. The close distance to ground produces edge effects that create distortions in the electric field, particularly in the corners of the TPC. At the anode to field cage side, the homogeneity of the field is crucial to avoid dead zones on the pads. To achieve a uniform field in practically all the available volume, electrostatic simulations of the field cage were carried out. An open source finite element mesh gener-

ator software, gmsh [173], was used to compose a 2D model of the field cage with the appropriate materials and boundary conditions. After the model was built, the geometry was meshed into 16,585,650 nodes and 4,125,786 finite 8-node-quadrangular elements. The mesh obtained was imported into the multiphysics solver software Elmerfem [174], which solves the Laplace equation for a given charge and material configuration. While the anode is grounded, the voltage on the field cage strips drops linearly until it reaches the cathode, set to -6000 V. Finally, the field obtained was imported into the GARFIELD toolkit [175], which allows for the simulation of the electrons' drift considering in addition the gas mixture with the appropriate transport parameters at a given temperature and pressure, and the magnetic field map simulated for the PUMA solenoid (see Sect. 4.2.3). For this simulation, the gas mixture used was 95% Argon, 3% CF_4 and 2% Isobutane. The final mixture and proportions are to be evaluated to comply with CERN safety regulations.

The configuration of the simulated field cage consists of two layers of electrode rings glued to each side of a flexible PCB material of 0.3 mm thickness: The electrodes that belong to the layer at the side of the active volume are 1 mm wide with 0.5 mm spacing, while those in the back side of the PCB are 1.1 mm wide with 0.4 mm spacing.

The drift of 1000 electrons was simulated by releasing them at different positions in the active volume. The maximum deflection from a straight path near the field cage, corresponding to electrons travelling through the complete length of the TPC, is less than 0.4%, which has no impact on the disentanglement of positively and negatively charged pions. Figure 32 shows the deflection, defined as

$$\Delta r = \sqrt{(x_i - \langle x_f \rangle)^2 + (y_i - \langle y_f \rangle)^2}, \quad (19)$$

where x_i, y_i are the initial position of a cloud of 1000 electrons in the *XY* plane (transverse to the drift direction) and $\langle x_f \rangle$, $\langle y_f \rangle$ are the mean values of the final position reached by the same cloud on the *XY* plane after drifting a distance L, as a function of the radial direction (horizontal axis *x*).

4.5.3 Background rejection

The influence of atmospheric muons, product of cosmic ray showers in the atmosphere, was investigated. Simulations with Geant4 have been made to determine their rate and the rejection capabilities of PUMA.

The simulation of atmospheric muons was done using the Cosmic Ray Shower library (CRY) integrated in Geant4 in which cosmic ray showers are generated from data tables and show good agreement with cosmic rays measurements [176]. The library allows to choose a set of parameters (altitude, latitude and date -to account for the eleven year sunspot cycle-

Table 6 Material budget of the inner tube, the TPC and the plastic scintillators

Piece	Material	Density [g/cm^3]	Thickness [mm]	Radiation length [mm]	Radiation length [%X0]
Trap	Cu	8.96	4	14.3	27.9
Cryostat	Cu	8.96	0.75	14.3	5.2
70 K shield	Al	2.50	1	88.9	1.12
300 K vacuum pipe	Al	2.50	5	88.9	5.62
Insulator	Polyimide	1.42	4×0.02	285	0.02
Field cage outer structure	PCB	1.8	1.5	280	0.53
Field cage	PCB	1.8	0.3	280	0.1
Gas mixture	ArCF$_4$Iso	0.0019	53–55	107213	0.05
Insulator	Mylar	1.4	0.02	285	0.007
Scintillator wrap	Teflon	0.38	1	158	0.63
Scintillator	PVT	1.032	4	425	0.9
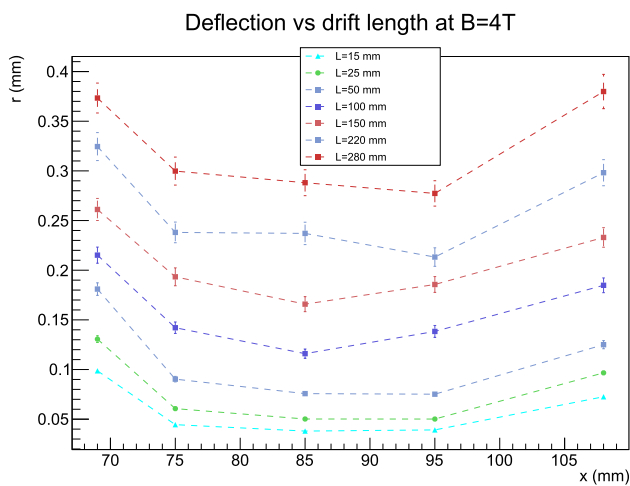
Fig. 32 Deflection Δr (Eq. 19) as a function of the radial direction (x)

Fig. 33 Comparison of the energy deposit in the TPC by muons and pions

) to adjust the particle distributions to the conditions in which the experiment will work. Cosmic particles are generated in an area of 3×3 m^2 at 2 m above the detector.

From the simulations, the rate of muons expected to cross the TPC is ~ 2 s^{-1}. However, $\sim 90\%$ of them are rejected by adding the constraint that their track should also pass through the collision zone of the trap: In this case, after a simulation of 3 million muons, the expected rate is 8 ± 0.5 min^{-1}.

Figure 33 shows the total energy deposit per particle in the TPC, comparing the muons that cross the trap with the pions produced from the simulated events, assuming a rate of 10 min^{-1} real events. In this case, the energy deposit of the muons is larger than that of the pions since their track is about twice as large as that of the pions. A clear cut can be seen at ~ 30 keV and only less than 1% of the pions will have an energy deposit in the TPC similar to the muons. In addition, since the muons will only pollute the channels of multiplicity M = 1 and 2 (which represent 30% of the
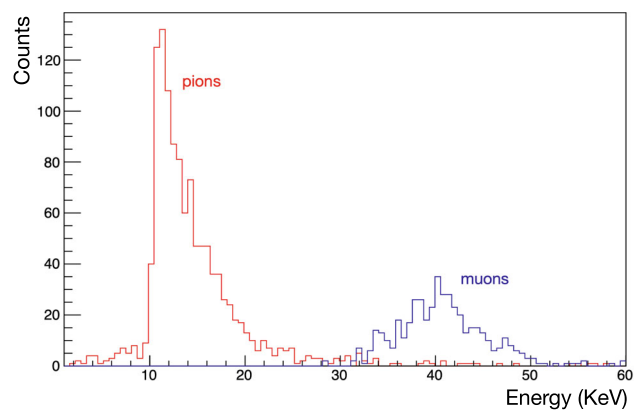
total branching ratios), it is estimated that at least 99.7% of the muons will be rejected. Moreover, it is expected to further reject muons from the track reconstruction in the z-axis during the analysis process and the measurement and subtraction of the background before the ions are introduced. Additionally, the curvature of the muons' trajectory due to the magnetic field will change after passing through the different components of the trap as a consequence of the energy loss experienced. A correlation between both types of tracks can be established and removed, leaving a negligible number of muons that might not be possible to disentangle from the pions. Studies are under progress. The muons have an important function, as they will allow an inspection of the functionality of the detection system (barrel and TPC). The procedures to be adopted are being formulated.

4.5.4 Amplification

As mentioned previously, the amplification of the signal will be achieved via a Micromegas concept [177]. In particular, the resistive Micromegas technology will be deployed.

The mesh woven will be 18 µm with 45 µm spacing. A standard 128 µm gap between the mesh and the resistive foil will be used for amplification. The avalanche produced is diffused in the resistive foil following the telegraph equation [178]

$$\rho(r, t) = \frac{RC}{2t} e^{-r^2 RC/(4t)}, \tag{20}$$

where RC are the resistance and capacitance respectively, determined by the spacing between the anode and the readout pads, and the dielectric constant of the glue. This provides a number of advantages:

– The preamplification stages of the electronics do not need to be protected if this technique is used.
– With the high suppression of transverse diffusion in strong magnetic fields, the track ionization charge clusters arriving at the pad plane will be confined to a single pad, resulting in a loss of resolution. However, the spread of the signal in three to four pads perpendicular to the track will enable a more accurate centroid determination, thus reaching values of the order of $\sigma \approx 100$ µm for zero drift distance.

Table 7 is drawn on specifications and the expected performance for the resistive micromegas.

Given a modest gain of 10^4 in the micromegas, and the electronic noise of the front-end modules set at 1 m away from the pad plane, the signal-over-threshold ratio for induced signals on the side pads of the main projected pad is approximately 4 for a signal originating from 30 primary electrons, assuming a threshold set at $5 \times \sigma_{RMS}$ ($\sigma_{RMS} = 1500$ e) and a resistive and diffusion spreading, giving 1:10. If, however, the noise or gain limits noted above are not achieved because of technical limitations, the system will operate simply through the plastic trigger because of the low rates involved.

4.5.5 Gas system

The gas handling system for the PUMA TPC is an open-loop system that will supply a regulated gas flow at atmospheric pressure where the premixed, non-contaminated gas is provided from a standard B50 bottle. The final composition will be chosen to be in accordance with the safety regulations and recommendations at CERN. A choice of CF_4-free gas mixture is being studied. The choice of the gas for the TPC is a trade-off between electron transverse and longitudinal dif-

fusion, electron drift velocity and maximum reachable gain. From the mentioned parameters, PUMA's event rate (10–100 Hz) does not require an ambitiously-high drift velocity. Instead, more importance is given to the gain in the amplification step and the transverse diffusion coefficient, which is relevant for the centroid determination given the strong magnetic field of PUMA. The drift field will be studied on a prototype and will include the optimized charge and time resolutions.

As considered to date, there will be 4 gas inlets on the cathode and 4 on the anode, where the gas mixture will be filtered for dust particles. The tubing system will allow to establish clean lines with very low contamination of H_2O and O_2 in the gas. The gas flow will be regulated from a flowmeter in series between the regulator of the bottle and the TPC. The pressure in the TPC relative to atmospheric pressure is kept constant with better than 0.1 mbar precision. Oxygen and water will be removed from the gas with cartridges filled with a copper catalyzer. Ten l/h of mixed gas continuously flow through the TPC which has a volume of 16 l. A small amount of gas will be analyzed at the exit line, which will provide a measurement of the O_2 and H_2O contaminants. The exhaust will be combined with an oil-filled bubbler to avoid air back-flow. The system is arranged in functional modules distributed on shells of the frame system and on the floor of the PUMA frame. A Programmable Logic Controller (PLC) will supervise the system with a user interface based on National Instrument software and modules, where the temperature and the pressure will be monitored continuously. A particle filter will be placed at the entries of the gas supply, accessible for regular change and inspection.

During transportation, the main gas bottle will be disconnected from the system and the gas system will run on a 5-liters backup gas supply attached to the frame.

4.5.6 TPC trigger–scintillator barrel

The choices of plastics, geometry and SiPM are relatively standard. At this stage of the project, samples of two types of plastic, EJ-204 and EJ-212 are being tested.

Machined, trapezoidal sectioned polished bars of 4 mm thickness have been purchased and will be tested at TU Darmstadt, as well as two types of sample SiPM (Hamamatsu and On Semiconductor) of 3×3 mm^2 that couple well with the plastics in terms of wavelength response.

Simulations of photon emission and transport to the SiPM have been performed by means of the GODDeSS library extension of the Geant4 toolkit [179]. Figure 34 displays the energy deposit of the pions in a plastic scintillator as a function of its thickness, showing that the mean energy deposit obtained for a 4 mm thick plastic is in the order of 1 MeV, corresponding to a mean light yield of 10400 photons. Ten percent of this value will be detected by the 4 SiPMs

Table 7 Amplification region specifications

Specification	Value
Mesh woven	18 μm
Optical transparency	54%
Pad geometry	Projective with constant area of 10 mm^2
Inter-pad distance	150 μm
Pillars diameter	300 μm
Pillar spacing	6000 μm on inter-pad crossing
Pillar height	128 μm
Gain	10^4
XY resolution at 1 cm and 30 cm drift with 4T	150 μm and 200 μm
Charge resolution	22%
Time resolution	5–10 ns
Z resolution	250–500 μ m
Rates	200 Hz
DLC resistivity	3 MOhm before baking

in a given plastic scintillator. The simulation of the three Hamamatsu SiPMs models with different pixel pitch that will be tested (25, 50 and 75), gives a mean photon count of 50 to 100 per SiPM, well above the typical dark current threshold of 10–20 photons. In addition, it is expected that the time resolution in one scintillator bar will be of the order of 100 ps.

The study of the plastic's acceptance via simulations performed with GEANT4 shows that the maximum acceptance, considering a TPC of 300 mm length, is reached for a length of ∼ 450 mm (see Fig. 35).

Each scintillator bar will be wrapped with Teflon and aluminised mylar of 100–150 μm thickness to allow minimum light cross-talk and to reach optimal light capture. The position resolution along the longest dimension of the bar is
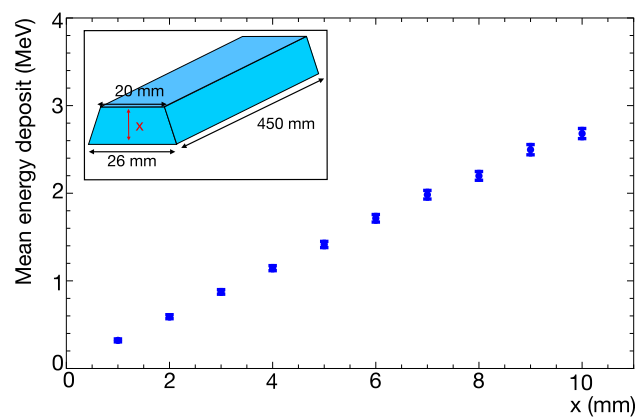

Fig. 35 Acceptance obtained for simulated events detected in the plastic scintillators. The red vertical line shows the length of the TPC. The dotted line shows that the maximum acceptance (ratio of detected events over total number of events) reaches a value of 0.98 from ∼450 mm

expected to reach 10 mm FWHM from the time difference of the signal received on both ends of the bar.

The barrel will require 128 channels of electronics, namely 2 SiPM attached on each side of each plastic. This will allow relatively low thresholds to be set on the SiPMs and hence a high efficiency and a good time resolution.

4.5.7 Electronics

The PUMA-TPC consists of 4096 channels, surrounded by a barrel of plastic scintillators which is read by 128 SiPMs. The signal will be transported via low capacitance cables (possibly 50 pF/m) to a common data acquisition system with the front and back end electronics being housed outside the magnetic field. The stray magnetic field in this placement is lower than 2 mT, which complies with the electronics specifications for proper operation. Tests with sample cables from the barrel and TPC are forseen, however experience from

Fig. 34 Energy deposit by simulated pions as a function of the plastic's thickness. The inset in the upper left corner shows a sketch of the plastic bar shape with the simulated dimensions. The error bars correspond to statistical uncertainty from the simulation
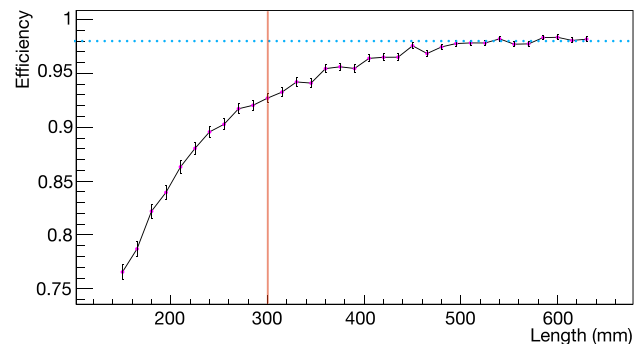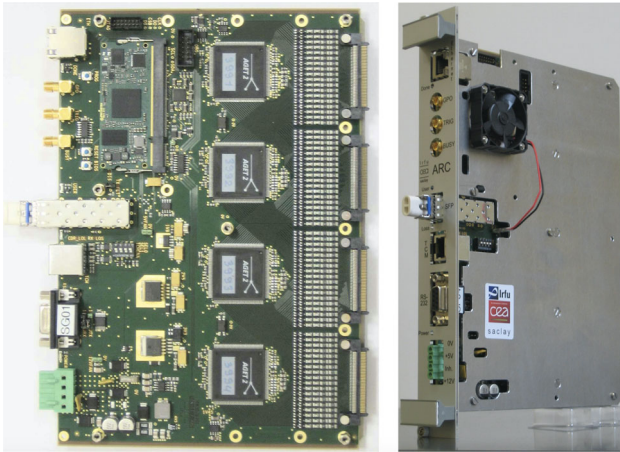
Fig. 36 (Left) ARC front end card equipped with four AGET chips. (Right) ARC front card with the electromagnetic shield and a fan

Fig. 37 Equivalent Noise Charge (ENC) versus input capacitance for different peaking times in the 120 fC range. Courtesy of B. Pascal, IRFU-CEA

MINOS [170] at RIKEN largely covers the difficulties associated with the needed cable lengths, of about 1 m.

The front-end electronics for the TPC consist of the so-called "Another Readout Card" (ARC), shown in Fig. 36. ARC collects the analog signal from the pads through four readout Application Specific Integrated Circuits (ASICs). It is then sampled in an analog memory (512-bucket switched capacitor array) and converted into digital format using a 4 channel (one per ASIC), 25 MHz 12-bit multi-channel analog-to-digital converter (ADC).

The system will operate with the latest development by IRFU, STAGE [180], based on the previous ASICs, AFTER [181] and AGET [182].

All generations of chips allow for pulse shape sampling at a programmable frequency of 1–100 MHz and support programmable charge range and peaking time. AFTER supports 72 channels while AGET and STAGE supports 64 channels. The most notable difference between AFTER and its successors is that the newer chips provide the possibility of self-trigger with a discriminator in each channel. These discriminators also allow the selective digitization of hit channels, which reduces readout dead-time and data volumes. Another advantage of AGET and STAGE over AFTER is that the charge sensitive preamplifier (CSA) covers a wider dynamic range (120 fC to 10 pC while AFTER has a maximum range of 600 fC) and the 4 possible values of dynamic range is adjustable on a per channel basis, while it is identical for all channels in AFTER.

Although both AGET and STAGE are suitable for PUMA, STAGE brings a few improvements. In particular the range of peaking time (16 possible values) covers 50 ns to 8 μs while it is 50 ns to 1 μs in AGET. Also the dynamic range of the analog output signal that represents the number of hit channels can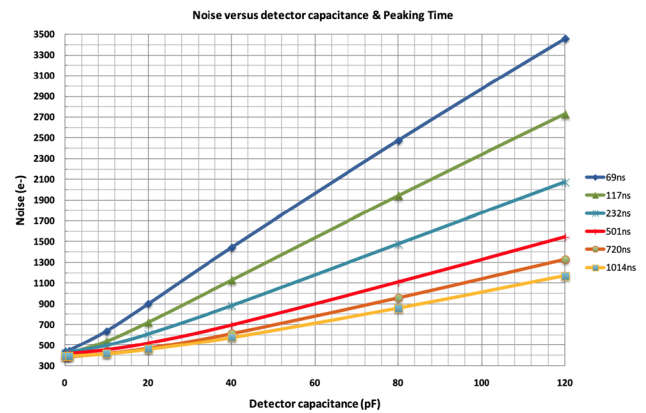 be set to correspond to 16 hit channels instead of 64. This allows a more robust discrimination of low hit multiplicity counts.

The rms noise per channel as a function of input capacitance is given in Fig. 37 for a 120 pC dynamic range. Using a peaking time of 230 ns and an input total capacitance of 80 pF gives a noise level of 1200 electrons rms. Hence thresholds of above 6000 electrons gives a significant operational margin to use the multiplicity trigger in the ARC electronics. The final settings of the ARC+TPC parameters will be adjusted to yield optimized efficiencies.

While STAGE is intended for operation in ordinary environments, a radiation hardened version, called ASTRE, is also available for the concerned scientific applications [180]. The main specifications are detailed in Table 8.

Flat cables give the input from the TPC. Outputs, numeric data, clock, and trigger are optically carried to the Trigger and Data Concentrator Module (TDCM) and forwarded over standard Ethernet to a control and data acquisition PC. Hence the system is reasonably well protected from electromagnetic disturbances. An assembly in crate is shown in Fig. 38.

The data of each detector module are transported to the back-end unit by optic fibers. The back-end consists of a TDCM, which distributes a primary reference clock to the set of front-end cards as well as a common trigger signal and global synchronization of the front-ends [183]. The TDCM is composed of two mezzanine cards (custom made board that can house up to 16 small form factor pluggable optical transceivers (SFP)) that are plugged into the carrier board of the back-end unit, a Field Programmable Gate Array (FPGA) module (the Mercury ZX1 commercially available from Enclustra [184]), and a main carrier board designed to carry the FPGA module and the mezzanine cards. A test setup is currently under preparation at TU Darmstadt.

For 4096 pads of the TPC, 64 STAGE chips housed on 16 ARCs will be needed. Regarding the back-end, one TDCM

Table 8 Synthesis of the AGET/STAGE chip [180]

Parameter	Value
Polarity of detector signal	Negative or positive
Channel numbers	64
External preamplifier	Yes; access to the filter or SCA input (external CSA)
Charge measurement	
Input dynamic range	120 fC, 240 fC, 1 pC, 10 pC
Gain	Adjustable per channel
Output dynamic range	2V p-p (differential)
INL	$< 2\%$
Resolution	$< 850\ e^-$
	(Gain: 120 fC; Peaking Time: 200 ns; $C_{\mathrm{input}} < 30\mathrm{pF}$)
Sampling	
Peaking time	8 μs (16 values)
SCA time bin number	512 or 2×256 cells
Sampling frequency	1 MHz to 100 MHz
Multiplicity	
Multip. signal	Analog sum of 64 discriminator outputs
Input dynamic range	5% or 17.5% of input channel input charge range
INL	$< 5\%$
Threshold value	7-bit DAC
Readout	
Readout frequency	25 MHz
Channel readout mode	Hit, selected or all
SCA readout mode	1 to 512 cells
Test	
Calibration	1 channel among 64; 1 external test capacitor
Test	1 channel among 64; internal test capacitor (1 among 4)
Functional	1 to 64 (68); 1 internal test capacitor per channel
Counting rate	< 1 kHz
Power consumption	< 10 mW/channel @ 3.3 V

module would suffice since it can read out up to 32 ARCs, i.e. 8192 channels.

Here we have not included a detailed description of the ARC+TDCM system as it has been largely documented in FEMINOS [185]. However it is important to note that ARC+TDCM is a second generation of FEMINOS and we thus expect an enhanced performance with this novel system even though the PUMA project is less demanding both in coupling with other subsystems and in rates. Firmware on TDCM will be developed to take into account the improved resolution through the use of resistive micromegas.

Because the required timing resolution for the barrel scintillators is above the performance reachable with the STAGE chip, the plastic scintillator barrels will be read out using TRB3-based digital electronics [186]. The TRB3 system is a versatile FPGA-based platform which can be used primarily as a TDC and is accompanied by a variety of front-end
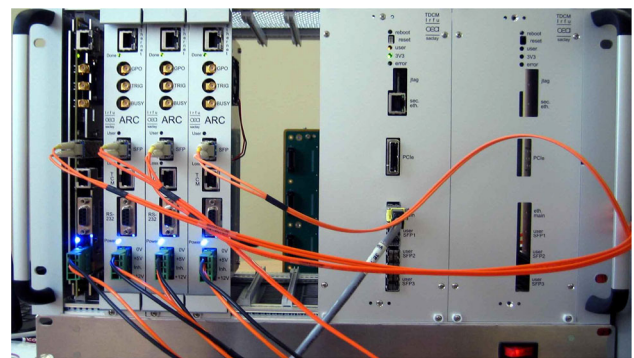
Fig. 38 Front-end and back-end cards set within an enclosure

electronic modules, ensuring full compatibility throughout the electronics chain. In the present case, we intend to use a PADIWA4 [186,187] signal discriminator board, developed to handle PMT-like signals. Each PADIWA4 card has 16
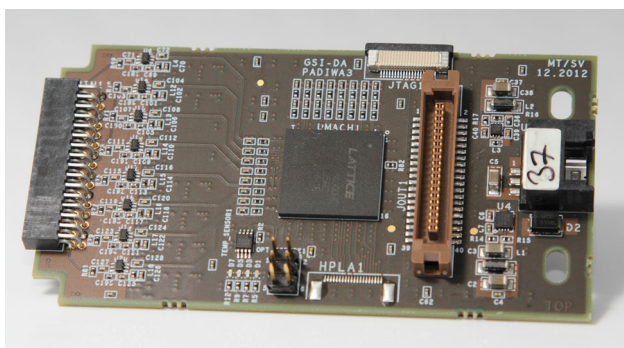
Fig. 39 PADIWA3 front-end board [186]. The PADIWA4 board has the same size and similar layout, mainly without signal amplification, in order to handle larger signals
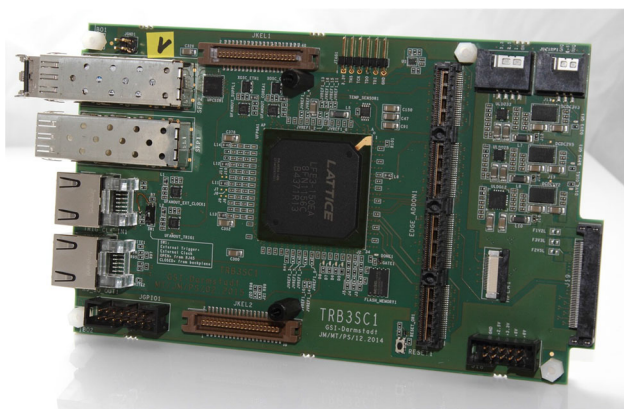

Fig. 40 TRB3sc board, with bare 208-pin connector [186]

input channels which are discriminated individually against a reference voltage at the LVDS input buffers. The pulse width is encoded into the timing of differential signals sent to the TRB3 TDC. The timing information can thus be obtained from the leading edge LVDS signal and the pulse amplitude from the time difference between the leading and trailing edge signals, providing a time-over-threshold measurement.

The layout of the PADIWA4 board is shown in Fig. 39. The input is received through a 32-pin connector seen in the left of the figure. The LVDS output is transmitted to the TDC through a 40-pin connector to a ribbon cable. Additionally, each PADIWA4 board is powered individually with 5 V. The PADIWA4 boards will be placed as close as possible to the SiPMs connected to the plastic scintillator bars, in order to reduce any losses of the analog signal. Therefore, the front-end electronics boards need to be small and not require any active cooling, criteria that are met by the chosen front end. Once the analog signals have been converted to LVDS signals, they are directed to the TRB3 board *via* ribbon cables.

The TRB board family comes in various versions and form factors. The original TRB3 boards are equipped with 5 FPGAs, where basically 4 FPGAs could be programmed to match the users' needs, while the fifth FPGA is used for communication with the 4 peripheral FPGAs and for triggering purposes. In the present case, a smaller version - the TRB3sc - will be used (as shown in Fig. 40), which is to be used in a 3U crate with a dedicated back-plane for data transfer and slow-control communication. Each crate needs a master TRB3sc board in slot 5. This TRB3sc board takes over the role of central FPGA of the TRB3 board, and allows the remaining TRB3sc boards in the crate to be run and read out. If only one crate is in use, an additional TRB3sc board will be programmed as CTS (Central Trigger System), required for the data acquisition to run. When fully equipped, the crate will then contain 8 slave TRB3sc boards, which can be used as TDCs. These boards will be equipped with 4conn add-on boards [186] which allow for 4 ribbon cables with standard 40-pin connectors to be connected to each TRB3 FPGA. The current TDC design, however, only allows up to 48 channels to be used per FPGA and is therefore configured to only accept inputs on the first three 40-pin connectors. This limitation is expected to be resolved in the mid-term future.

The TRB3 TDC determines hit times using two different timescales. A 200 MHz clock determines a 5 ns time grid with which the coarse times t_{c1} and t_{c2} are measured. For precise timing, a tapped delay line [188] is used to measure the hit time between the 200 MHz clock cycles, resulting in fine-time measurements t_{f1} and t_{f2}. With these time measurements, the time difference between two hits can be precisely reconstructed as [189]

$$\Delta t = \text{hit}_2 - \text{hit}_1 = (t_{c2} - t_{f2}) - (t_{c1} - t_{f1}) \\ = (t_{c2} - t_{c1}) - (t_{f2} - t_{f1}). \tag{21}$$

To ensure the highest possible timing precision, the 200 MHz clock signal must be identical for all input channels. When more than one TRB3sc board is used, an external clock source should be installed and distributed to all TRB3sc boards. Also, since the individual delays in the delay line are not identical to each other, they need to be calibrated before use. With a properly calibrated delay line and with a stable clock signal for all input channels, a time precision of the order of 10 ps RMS can be achieved [187–191].

After digitization of the scintillator signals, the data is collected from the individual TRB3sc boards through the back-plane of the TRB3sc crate and is concentrated in the TRB3sc crate master board. This board is connected *via* Ethernet cable to a DAQ PC, on which the data acquisition as well as the TRB3 control framework is running. The PC is required to have two Ethernet ports, with at least one of them being a 1 Gb/s port or higher, to which the Ethernet cable from the TRB3sc system will be connected to.

Since a trigger signal must also be provided from the scintillators, a couple of additional constraints on the hardware configuration must be taken into account. While the PADIWA4 front-end boards will be used to separate hit can-
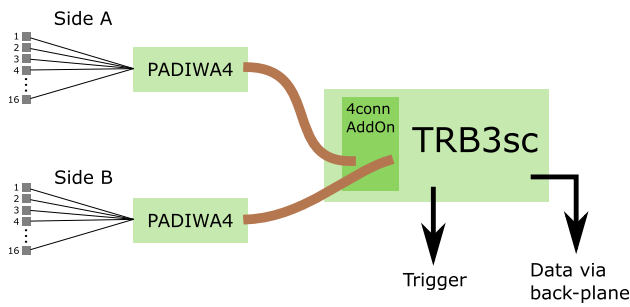
Fig. 41 Cabling scheme for scintillator barrel electronics

didates from the dark counts using the adjustable threshold, a more advanced trigger definition is required to combine high trigger efficiency and selectivity. As soon as the majority of dark rate has been cut by selecting an appropriate threshold, a coincidence between the sensors at both ends of a given scintillator will be requested, which will provide a good trigger selectivity. The trigger logic is executed within the FPGA of the TRB3sc board. Since a synchronous trigger signal is required, all logic operations must be carried out in the first-level FPGA, meaning that no logic operations involving channels on different FPGAs is possible, as the data stream is asynchronous. Therefore, a cabling scheme for all scintillator channels must be established, to ensure that the sensors of both ends of any given scintillator are cabled to the same FPGA. Due to the minimization of cable lengths for the analog signals, each PADIWA4 board will be connected to sensors located all on the same side of the detector, meaning that the signal emerging from the opposite end of the scintillator will in all cases be sent to another PADIWA4 board. As shown in Fig. 41, the desired trigger logic can be implemented if a series of 16 channels from one side of the detector (Side A) is sent to one PADIWA4 and the 16 signals of the opposite end of the scintillators (Side B) to another PADIWA4. The two front-end boards must then be connected to a common TRB3sc board. Then, the following trigger logic can be executed on the FPGA and sent to the trigger output:

$$(A1 \wedge B1) \vee (A2 \wedge B2) \vee (A3 \wedge B3) \vee ... \vee (A16 \wedge B16). \tag{22}$$

Each TRB3sc will perform the same logic operation, which will allow all trigger signals to be combined by logical OR into a single trigger in a dedicated trigger board. This unfortunately prevents all 48 channels of the TDC to be used, if all channels are to be cabled in the same manner. Only 32 channels per TRB3sc boards will then be used, until the TDC image is upgraded to handle the full 64 TDC channels.
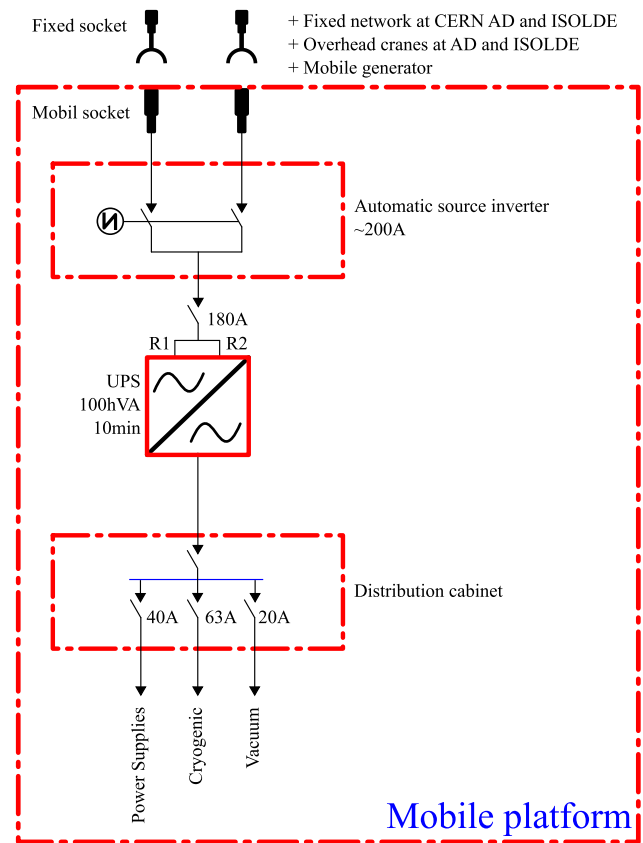

Fig. 42 Powering scheme for the PUMA experiment. The UPS is integrated inside the PUMA frame

4.6 Electrical power

The PUMA frame has the ability to be powered by 2 different input sources while being channeled through the Uninterruptable Power Supply (UPS) system which is installed into the smaller support frame of PUMA. This allows an interruption free switching between grid, power generator or any other appropriate source of power. The power grid, as it is currently installed in the PUMA frame is considered to be a TN[3] system.

4.6.1 UPS

The PUMA powering scheme relies on an integrated UPS of 100 kW for a lifetime of more than 5 minutes. The UPS allows a AC-DC-AC conversion which solves any phase offset between the two AC power sources. The UPS will absorb power shortages from the grid.

In addition, it provides a power buffer in case of extra transient consumption. The powering scheme is illustrated in Fig. 42.

---

[3] Earthed neutral.

The input power selection cabinet allows to switch between different electrical grids. Each grid has to be 400 V, 3 phase/N/PE, 50 Hz. Switching is associated with going through the "0" position of the switch where both grids are disconnected. The output of the power selection cabinet is connected to the UPS. Under standard operating conditions, the UPS can buffer the time needed to switch between two grids.

For operating on the on-site grid or on the power generator, a standard 125 A CEE connector (e.g. 125A 5P 400V 6h IP67 von WALTHER-WERKE, Art.Nr.: 379) will be connected to the input power selection cabinet.

4.6.2 Power generator

A 80 kW diesel power generator will provide the power to the PUMA experiment when (i) the experiment is transported by truck from ELENA to ISOLDE (normal operation), (ii) a power outage longer than 60 s takes place at ELENA or ISOLDE.

As stated earlier, at this stage, three diesel generator UPS are considered: one at each experimental zone, and one dedicated to transportation. The generators at experimental areas will be automatically triggered in case of power shortage longer than 10 seconds.

4.7 Vacuum and antiproton storage

4.7.1 Objectives

The PUMA project aims at storing antiprotons with a half-life of the antiproton plasma better than 30 days. Around 30 days is indeed the duration of an experimental cycle which includes capture of antiprotons at ELENA, transportation, installation at ISOLDE and experiments for a total of ~ 10 days. In addition, annihilations on the residual gas inside the collision trap also contribute to a background for the measurement of annihilations on radioactive nuclei. The lifetime is limited by these annihilations of the antiprotons with residual gas molecules and thus the pressure level P_T within the trapping region. Based on the empirical formula

$$\tau [\text{days}] \approx 6 \cdot 10^{-16}\, T[\text{K}]\, /\, P_T\, [\text{mbar}], \tag{23}$$

the lifetime τ of the antiprotons within the trap can be estimated as a function of the temperature T and the pressure level (see Sect. 4.7.2 for the derivation). To be able to perform a full experimental cycle (*i.e.*, accumulation, transportation and interaction with short-lived ions) PUMA aims for a lifetime of at least 30 days and low annihilation rate on residual hydrogen molecules of $\mathcal{O}(1\ \text{Hz})$. Both conditions can be met for a vacuum level of $P_H < 1 \cdot 10^{-17}$ mbar for a trap temperature of about 4.2 K. This cryogenic trap temperature

is necessary to reach such low pressure levels, because the surfaces of the electrodes and the vacuum tube containing the trap setup as well as the PDT then act as a cryo pump, which adsorbs residual gas molecules on the surface. Due to the low thermal energy of these molecules, they cannot overcome the weak attractive force of the surface and eventually stick to it. By this cryopumping, the pressure levels can be reduced by several orders of magnitude ($< 1 \cdot 10^{-17}$ mbar in the ATRAP [108] and BASE [192] experiments, for example) in comparison to the pressure levels reached with conventional vacuum pumps at room temperature (typically $> 1 \cdot 10^{-12}$ mbar, while a lower vacuum, $> 1 \cdot 10^{-14}$ mbar, can be reached with extensive use of NEG coating). To ensure that the cryogenic temperature is kept during the operation and transportation of the setup, two cold heads are connected to both ends of the vacuum tube. The general concept of transporting charged particles within a Penning trap, on a truck, has already been demonstrated for electrons by Tseng and Gabrielse [193].

In the following section, the residual gas is considered to be composed solely of molecular hydrogen (H_2) as the other gas species are most likely pumped by the different vacuum pumps in front of the PUMA frame. However, a direct determination of the hydrogen vapour pressure within the cryostat is not possible, as the corresponding isotherm is not defined down to such low pressures. Instead, the following simulation determines the hydrogen molecule number density, which is also helpful for determining the background signal in the collision zone region caused by residual gas annihilations.

4.7.2 Lifetime of the antiproton plasma

The lifetime of the antiproton plasma and the residual-gas density in the trap are related. The following capture cross section of antiprotons on molecular hydrogen, which is likely to be the dominant process in a cryogenic vacuum system, is assumed [194–196]

$$\sigma = 3\pi a_0^2 \sqrt{\frac{27.2\ \text{eV}}{E}}, \tag{24}$$

where $a_0 = 5.3 \times 10^{-11}$ m is the Bohr radius of the hydrogen atom and E the kinetic energy of the antiproton in the centre-of-mass system. The annihilation probability Γ is given by [196]

$$\Gamma = \frac{1}{\tau} = n_{\text{gas}} v \sigma, \tag{25}$$

where $v = \sqrt{2E/m_p}$ is the antiproton velocity. The lifetime τ of the antiproton plasma relates to the residual gas density

Table 9 Equivalence between the pressure P, the molecular volume density n_{gas} at 4 K and the lifetime τ of the antiproton plasma. The density and lifetime have been rounded to the closest decade

n_{gas} (cm^{-3})	τ (days)	P (mbar)
200	30	10^{-16}
20	300	10^{-17}

Fig. 43 Schematic drawing depicting (left) submonolayer cryosorption, where the pumping is based on molecule-substrate interactions; and (right) cryocondensation, where the leading mechanism is intermolecular interaction

via [196]

$$
n_{gas} = \frac{1}{\tau} \left(3\sqrt{2} \pi a_0^2 \cdot \sqrt{\frac{27.2 \text{ eV}}{m_p}} \right)^{-1}
$$
$$
\approx \frac{1}{\tau} \left(5.2 \cdot 10^8 \right) \text{ s} \cdot \text{cm}^{-3}. \tag{26}
$$

Considering the equation of state for ideal gases $PV = nRT$, one gets Eq. (23) and the equivalence of τ, n_{gas} and P of Table 9. According to Table 9, a pressure of at least 10^{-16} mbar to keep the antiproton plasma for 30 days would be needed. A residual gas density[4] $n_{gas} = 20$ cm^{-3} is the maximum number of gas particles we should allow to achieve a low rate of residual-gas-induced annihilations. The half life of the antiproton plasma after which half of the initial number of antiprotons has annihilated relates to the lifetime through the relation $t_{1/2} = \ln(2)\tau$.

With the above requirements, the design of the cryostat and the vacuum conditions of PUMA are a central challenge of the experiment. Special care is therefore taken into account to (i) optimize the vacuum conditions in front of the PUMA setup at both ELENA and ISOLDE, (ii) design the cryostat to achieve the residual gas density requirements for a time exceeding 30 days. The design of the cryostat is the object of this section. The realisation of the vacuum conditions at ELENA and ISOLDE are detailed in Sects. 4 and 6, respectively.

4.7.3 Cryopumping

To satisfy the above requirements, the concept of PUMA is based on cryopumping on the 4 K surface of the trap electrodes and cryostat. The extreme vacuum is maintained as long as the surface density of adsorbed molecules on the walls of the trap does not exceed a critical value given by the H$_2$ isotherm at the temperature of the trap.

Cryopumping relies on two main pumping mechanisms: cryocondensation and cryosorption. Cryocondensation is based on the intermolecular Van der Waals forces which are

---

[4] For PUMA, we use the residual gas density target value as an objective, instead of pressure. Indeed, they are related by Ideal Gas Law only for isotropic speed distribution. If there is a flow or beaming this is no longer true and pressure depends on the orientation of the surface as it is defined as force per unit area.
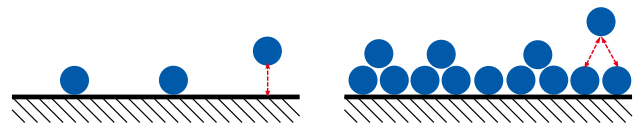
strong enough to maintain molecules bound together when the temperature is low enough (see Fig. 43). The key property is the saturated vapour pressure P_v, i.e. the pressure of the gas phase in equilibrium with the condensate at a given temperature. The lowest pressure attainable by cryocondensation is limited by the saturated vapour pressure. Among all gas species, only Ne, H$_2$ and He have P_v higher than 10^{-11} mbar at 20 K. The saturated vapour pressure of H$_2$ at the liquid He boiling temperature (4.2 K) is in the 10^{-7} mbar range, and is 10^{-12} mbar at 1.9 K. The quantity of gas that may be cryocondensed is very large and limited only by the thermal conductivity of the condensate. Cryosorption, on the other hand, is based on the attraction between gas molecules and the substrate. The interaction forces with the substrate are much stronger than those between similar molecules [197]. As a result, providing the adsorbed quantity is lower than one monolayer, the sojourn time is much longer and gas molecules are pumped at pressure much lower than the saturated vapour pressure. A significant quantity of gas may be pumped below one monolayer if porous materials are used; for example, in one gram of standard charcoal for cryogenic application, about 1000 m^2 of surface are available for adsorption. Carbon coating increases the effective surface of a metal substrate by a factor one hundred [198].

4.7.4 Isotherms

At equilibrium, the residual gas density in the cryostat depends on three main factors: the temperature of the cold surface, its effective area and geometry, and the molecular occupation of this surface. The partial pressures of all relevant gas species at temperature levels of liquid Helium ($T = 4.2$ K), achieve the saturation vapour pressures of $P_v < 10^{-12}$ mbar, except for hydrogen and helium. All gas species heavier than hydrogen and helium are pumped by cryocondensation.

The isotherm for a specific molecule on a specific substrate gives the relation of the surface coverage and the vapour pressure. If the surface coverage ratio $\Theta = S/S_m$ between the actual surface coverage S and the maximum monolayer capacity S_m is lower than unity, the pressure at equilibrium will be lower than its saturation pressure. This ratio depends only on the surface temperature and the surface coverage. This relationship is described by an adsorption
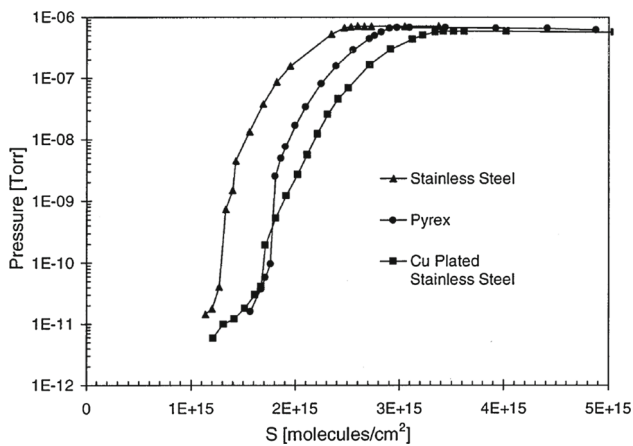
Fig. 44 H_2 adsorption isotherms at 4.2 K on Pyrex, Stainless Steel, and Cu plated Stainless Steel. Reprinted with permission from [211], ©1997 American Vacuum Society

Fig. 45 Measured adsorption isotherms of H_2 on an electropolished stainless steel surface for temperature 17.9 K, 15.1 K, 13.7 K, 11.3 K, 9.1 K, 8.1 K and 7.3 K (straight curves). The dashed curves are fitted theoretical isotherms calculated according to the DRK model. Reprinted with permission from [199], ©2019 American Vacuum Society

isotherm depending on S_m and P at a constant temperature. At $\Theta \approx 1$ the given pressure rises up to its temperature dependent saturation vapour pressure [199].

There are different models for adsorption isotherms. Examples are Henry's law [200,201], the Freundlich equation [202] and the Brunauer-Emmet-Teller (BET) isotherm equation [203,204], which all describe the isotherms for different temperatures and different pressures. The physisorption isotherms for low temperatures in the submonolayer region are described by the Dubinin- Radushkevich-Kaganer (DRK) equation [205–209], which is

$$\ln(\Theta) = -D \left[k_B \cdot T \cdot \ln (P_0/P) \right]^2 , \tag{27}$$

where T is the temperature, k_B is Boltzmann's constant and D is an empirical constant depending on the given adsorbent-substrate system. Furthermore P corresponds to the equilibrium pressure and P_0 is the saturated vapour pressure. D has an energy unit (eV^{-2}) and is linked to the vapourization heat of the adsorbate [200] and is also called the "DR energy" (Dubinin-Radushkevich energy) [210].

The adsorption isotherms of H_2 on pyrex, stainless steel, and Cu plated stainless steel measured at CERN [211] are shown in Fig. 44. All three isotherms in this figure can be divided into three parts: a plateau area, where the isotherms reach the saturated vapour pressure, a cliff area where the isotherms have a steep rise, and, at lower pressure, the DRK region where the DRK equation is considered the best model to extrapolate the isotherms at pressures lower than $\sim 10^{-9}$ mbar.

In cryopumped XHV systems (below 10^{-12} mbar), hydrogen is typically the most dominant residual gas. For PUMA, we consider the H_2 isotherm data points measured at 4.2 K by Wallén [211] for Cu plated stainless steel and extrapolate the values to lower pressures. Data have been measured to
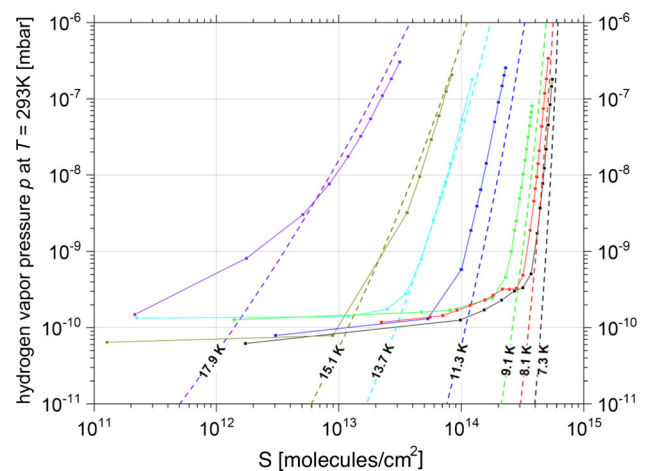
10^{-11} mbar and do not cover our XHV region of interest. To calculate the pressure P depending on the surface coverage S for the extrapolation, Eq. (27) can be reformulated as:

$$P = P_0 \cdot \exp \left[-\frac{\sqrt{-\ln (S/S_m)}}{\sqrt{D} \cdot k_B \cdot T} \right]. \tag{28}$$

We used data measured by Chill, Wilfert and Bozyk at GSI [199] to extrapolate the isotherm to our region of interest. They measured H_2 adsorption isotherms in a temperature range between 7 K and 18 K. Their data (straight curves) are pictured in Fig. 45, where it is easily seen that all pressure measurements saturate below $P < 4 \cdot 10^{-10}$ mbar, showing limitations in the measurement. The high quality of the data allows to extrapolate an isotherm to 4.2 K. A vapour pressure of $P_0 = 4.25 \times 10^{-7}$ mbar for H_2 was used [212], as well as an effective monolayer surface density $S_m = 6.45 \times 10^{14}$ cm^{-2} and $D = 1.29 \times 10^{41}$ J^{-2} (corresponding to $B = 3075$ eV^{-2}) from Ref. [199].

The extrapolation down to 10^{-17} mbar still generates large uncertainties which will lead to uncertainties in the lifetime of the antiproton plasma for a given cryostat geometry. It is therefore essential to measure the isotherms at lower pressure.

4.7.5 Initial conditions and outgassing

The phenomena of diffusion and outgassing are important throughout the operating pressure range of PUMA. Adsorbed particles can migrate into a solid by skipping to interstitial sites or lattice defects or by moving along grain boundaries of crystallites. This effect is temperature dependent, because the particles require energy for every position change an acti-

vation energy E_{dif}. Diffusion is caused by a concentration gradient dn_{dis}/dx and features after Fick's fist law a particle flow rate:

$$j_{dif} = -D \frac{dn_{dis}}{dx}. \tag{29}$$

Here, n_{dis} is the density of dissolved particles and x the path length. D is the so-called diffusion coefficient. The number of gas particles absorbed in the bulk of the surface material can be much larger than the number of adsorbed gas particles, because the number of sites available inside the solid is clearly much larger than on the surface of the solid [201]. During steel production a large amount of H_2 from the atmosphere dissolves in the steel [213]. This hydrogen in stainless-steel vacuum systems diffuses out and is the main source of residual gas in baked-out, ultra-high vacuum systems [201]. According to Kiuchi and McLellan [214], the hydrogen diffusion in steel can be expressed as an Arrhenius law following

$$D = D_0 \cdot \exp\left(-\frac{E_{dif}}{RT}\right), \tag{30}$$

where R denotes the ideal gas constant, T the temperature, with $D_0 = 7.3 \times 10^{-8}$ m$^2 \cdot$ s^{-1} and $E_{diff} = 5.69$ kJ/mol. According to Eq. (30), one gets $D \sim 10^{-40}$ cm$^2 \cdot$ year^{-1} for hydrogen in steel at 4 K. One can therefore legitimately consider that outgassing at 4 K is negligible. On the other hand, one may wonder what is the resulting surface coverage of the cryostat after the cooling phase.

In the following, we propose an order-of-magnitude estimate which shows that the residual gas present in the cryostat at the beginning of the cooling phase leads to a negligible contribution to the surface coverage. We assume the following cryostat conditions while cooling: a pressure of 10^{-7} mbar, volume $V = 5$ l, an effective inner surface $S = 0.5$ m^2. At equilibrium and considering the ideal gas relation, this pressure corresponds to a number of molecules in the volume of

$$N = \frac{PV}{k_B T} \sim 2 \times 10^{12}, \tag{31}$$

where $T = 300$ K, before cooling, is taken. If one considers that this number of molecules contribute uniformly to the surface of the cold surface when cooled to 4 K, one gets a surface density of 4×10^8 molecules per cm^2, very small compared to the value corresponding to 10^{-17} mbar, as extrapolated from the H_2 isotherm. We therefore conclude that the contribution of the initial residual gas molecules present in the cryostat before cooling is negligible for PUMA.

4.7.6 Molfow+ simulations

The Monte-Carlo software Molflow+ allows to calculate the pressure in a complex geometry when a molecular flow regime is met, i.e. when the mean free path of gas molecules is so long compared to the geometry size that collisions between the molecules can be neglected. In this case, the gas molecules fly independently, which makes this phenomena particularly suitable for Monte Carlo simulations. Desorption and reflection directions are generated in the same manner following the cosine law. The absorption on a surface is driven by a *sticking parameter* to be given as an input of the simulation. MOFLOW does not allow for a time dependent sticking factor, *i.e.*, coverage dependent. MOFLOW results are valid only for very low coverage when all the surface act as pumps.

In Fig. 46, a schematic overview of the cryostat used for the simulations is shown. The cryostat is divided in two parts, the *upstream cryostat* and the *downstream cryostat*. The beam will enter the cryostat from the left hand side. The upstream cryostat is divided into three parts:

1. A *4 K beam pipe*, where particles enter from the left hand side.
2. A pipe with a small diameter to further reduce the conductance at the entrance (*conductance pipe*).
3. In front of the conductance pipe is an area for additional elements like an einzel lens. This part of the conductance pipe is called the *cold gate-valve pipe*.

The downstream cryostat contains the pulsed drift tube (PDT) and the trap electrodes. This part is divided into the *collision zone* and the *storage zone*. The antiproton plasma will be stored during transport and during experiments within the trap in the storage zone and will be transferred into the collision zone for experiments at ISOLDE.

First simulations with Molflow+ were performed with a simplified cryostat model in order to study whether it is possible to get a number density lower than 20 cm^{-3} in the collision zone and the storage zone. A simulation with COMSOL Multiphysics was performed with the same parameters and lead to number densities which agree within a factor of 1.5, which provides a satisfying benchmark for the presented study.

4.7.7 COMSOL framework

For simulations which include the H_2 isotherm, COMSOL Multiphysics [215] version 5.5 (released 14. November 2019) was used, which is based on the finite element method (FEM). In addition to the core version, we used the Molecular Flow Module. The Molecular Flow Module is designed for the accurate modeling of low-pressure gas flows in complex

Fig. 46 Schematic overview of the cryostat and the electrodes/trap inside. The different parts of the cryostat are named diverse for an easier description in the text. The total length of the cryostat will be 1864 mm
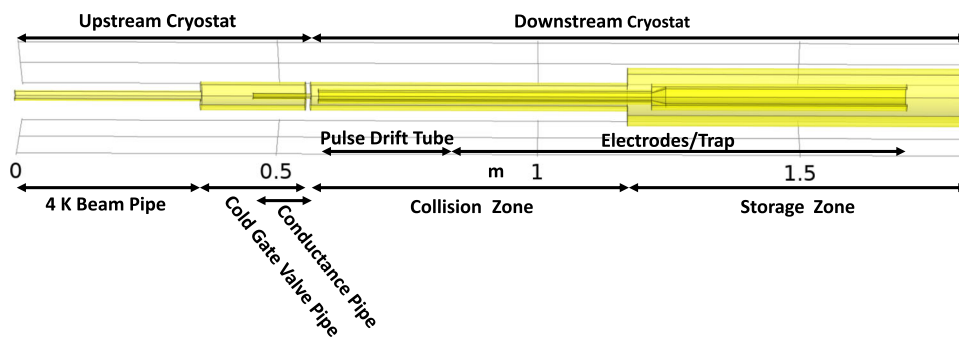
geometries and it is optimized for calculations with vacuum systems.

The gas flows that occur inside vacuum systems cannot be described by conventional fluid flow models. At low pressures, the mean free path of the gas molecules becomes comparable to the size of the system and gas rarefaction becomes important. Historically, flows in this regime have been modeled by the Direct Simulation Monte Carlo (DSMC) method. It computes the trajectories of large numbers of randomized particles through the system, but introduces statistical noise into the modeling process. For low-velocity flows, such as those encountered in vacuum systems, the noise introduced by DSMC renders the simulations unfeasible [216].

The Molecular Flow Module uses the angular coefficient method to simulate steady-state free molecular flows, allowing the molecular flux, pressure and number density to be computed on surfaces. In this context the angular coefficient method computes the molecular flow by summing the flux arriving at a surface from all other surfaces in its line of sight. The macroscopic variables (e.g. molecular flux, pressure, etc.) in the vicinity of the surface can be derived from kinetic theory. Furthermore the number density can be reconstructed from the molecular flux on the surrounding surfaces [216,217]. The angular coefficient method is using the Knudsen's cosine law and the Maxwell-Boltzmann distribution. The distribution of angles of reflection follows

$$f(\theta)d\theta = \frac{1}{2}\cos(\theta)d\theta \qquad (32)$$

and

$$f(\sin(\theta))d\sin(\theta) = \frac{1}{2}d\sin(\theta) \qquad (33)$$

for θ in the range $(-\pi/2, \pi/2)$ for cylindrical coordinates in two dimensions. The gas molecule velocity components follow in free space the Maxwell-Boltzmann distribution

$$\rho(c_i) = \sqrt{\frac{m}{2\pi k_B T}} \cdot \exp\left(-\frac{mc_i^2}{2k_B T}\right), \qquad (34)$$

where c_i is the velocity component in the i direction ($-\infty < c_i < \infty$) and $i \in \{x, y\}$ in two dimensions, k_B is the Boltz-

mann constant, and T is the temperature. In many cases it is reasonable to assume that molecules are adsorbed and subsequently diffusely emitted from the surface. In this instance, the appropriate probability density functions for emission from a surface $\rho(\theta, c)$, have been derived from the laws of physical gas dynamics and confirmed by molecular dynamics simulations [217–219].

4.7.8 Simulations

The simulations in COMSOL Multiphysics are performed with a cylindrical symmetrical 2D-shape which leads to less computational cost [217]. From the 3D-shape of the CAD-model a separate 2D model on the resulting cross section geometry was created. This modeling technique was used to complement realistic but heavy-to-compute 3D simulations.

The following figures summarize the simulation results by plotting the number density of H_2 on the center axis of the cryostat as a function of the longitudinal z-coordinate within the cryostat. The most important area for PUMA is in the z-coordinate interval between about 0.8 m and 1.8 m, as this interval represents the location of the storage zone and the collision zone, where the antiprotons will be stored and the interaction with other nuclei will be investigated, respectively.

One of the unknown factors at the PUMA experiment is the sticking factor s on the cold surfaces. The sticking factor describes the probability of a molecule to stick to the wall of the cryostat instead of being emitted. Its value depends on several parameters like the surface temperature, surface quality and numbers of molecules which were already attached. As a first assumption a sticking factor of about 0.3 is expected at low surface coverage [220]. At variance with MOLFLOW, our COMSOL simulations intrinsically consider the evolution of the sticking factor with coverage, i.e. time dependent. In our model the impinging flow is pumped at a constant sticking factor that corresponds to the sticking factor at zero coverage. We calculate the equilibrium pressure at the surface, using the isotherm, and we use it to calculate the flow emitted from the surface, also multiplied by the same sticking factor to ensure at equilibrium net flow is zero. As the coverage increases, the equilibrium pressure also increases
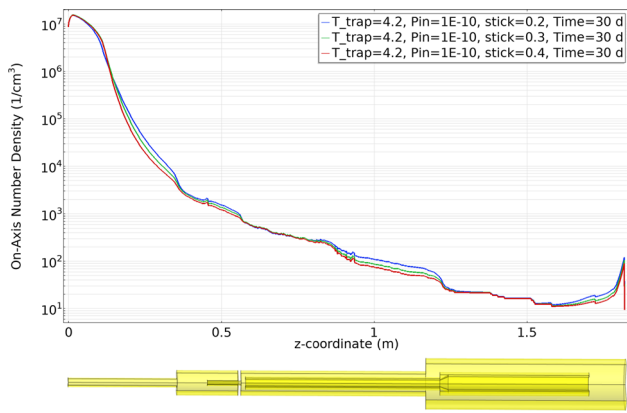
Fig. 47 On-axis H_2 number density after 30 days of particle flow through the pinhole ($z = 0$) with a radius of $f = 7.5$ mm into the cryostat for a wall temperatures of 4.2 K and different sticking factors $s = 0.2, 0.3$ and 0.4. The pressure at the entrance of the cryostat is 10^{-10} mbar. A 3D model of the cryostat is added for orientation

and so the flow emitted by the surface. This is equivalent to a part of the impinging flow being reflected and to a lower sticking factor with coverage.

In Fig. 47, simulations with sticking factors of $s = 0.2$, $s = 0.3$ and $s = 0.4$ are depicted. It can be summarized that a higher sticking factor leads to an overall lower on-axis number density in the region of the collision trap (between 0.8 m and 1.2 m), but the absolute values for the densities vary by a factor of less than 2 between the different sticking factors. In addition, the effect of the different sticking factors on the pressure in the storage trap (between 1.25 m and 1.7 m) is negligible.

To evaluate the influence of the temperature of the cryostat, simulations were performed at 4.2, 5 and 8 K. It can be concluded that the exact temperature of the cryostat does not have a huge impact on the on-axis number density in the region of the two traps, even for longer time intervals of 100 days. The reason for this is the low surface coverage of the cryostat wall within this region, which is well below the saturation coverage. This avoids the release of additional hydrogen on the center axis. An opposite behavior occurs within the 4-K beam pipe, where a significantly higher on-axis number density is reached after 100 days assuming a temperature of 8 K compared to the lower temperatures. This increase by at least one order of magnitude is presumably caused by a faster surface saturation and a higher release of hydrogen into cryostat.

The total number of incoming particles can be reduced by implementing a pin hole at the entrance of the cryostat. This pin hole will reduce the surface area where particles can enter the 4-K beam pipe. The smaller this pin hole will be the less particles can enter into the cryostat. A set of simulations has been performed to determine the effect of a reduction of the radial aperture at the entrance of the cryostat. Based on the
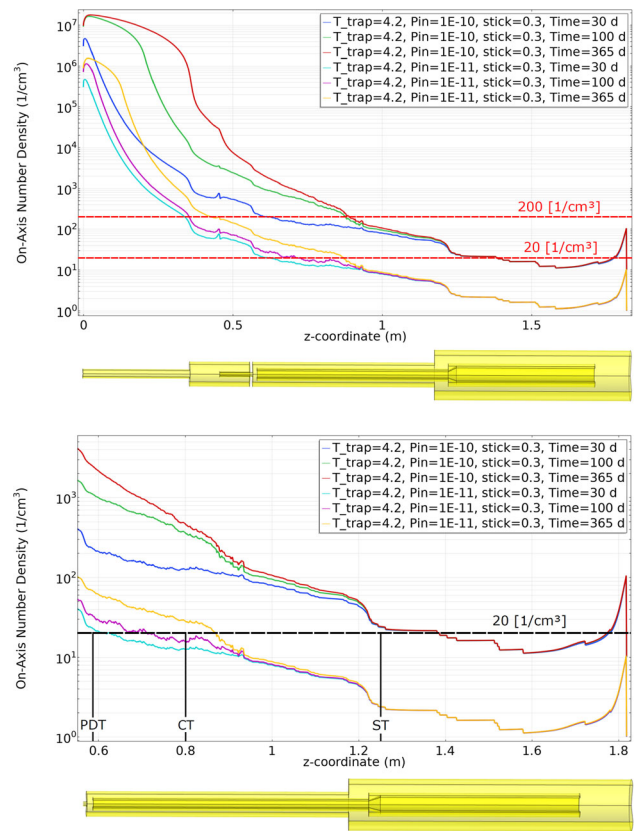

Fig. 48 On-axis H_2 number density after 30, 100 and 365 days of particle flow through the pinhole ($z=0$) with a radius of $f = 7.5$ mm into the cryostat for a wall temperature of 4.2 K and a sticking factor of $s = 0.3$. The pressure at the entrance of the cryostat is varied between 10^{-10} mbar as assumed in the previously plots and 10^{-11} mbar. The top plot covers the full cryostat, while the lower plots focuses on the trapping region, i.e. the pulsed drift tube (PDT), the collision trap (CT) and the storage trap (ST). In both cases a 3D model of the cryostat is added for orientation. In addition, the number densities corresponding to a pressure of 10^{-17} mbar (20 particles per cubic centimeter) and 10^{-16} mbar (200 particles per cubic centimeter) are highlighted

results it can be summarized that a reduction of the aperture by a pinhole has a negligible impact on the on-axis number density, because this density is mainly guided by the particles which enter the cryostat close to the center axis. Thus, to reduce the on-axis number density, it would be necessary to include a cold gate valve (cold shutter) which reduces the flux of incoming particles around the center-axis.

The minimization of the pressure in front of the cryostat is key to minimize the number of incoming residual-gas particles into the cryostat. An achievable 10^{-10} mbar vacuum was assumed in the above simulations. A proportional factor is expected between the vacuum at the entrance of the cryostat and the time to reach a given number density inside the cryostat.

In Fig. 48 the on-axis densities are simulated for time intervals of 30, 100 and 365 days assuming input pressures of 10^{-10} mbar and 10^{-11} mbar at the entrance of the cryostat.

Comparing the the curves of the two input pressures it can be concluded that the number density scales linearly with the input pressure for short time intervals up to 30 days. For longer time intervals, however, the saturating surface coverage within the 4-K beam pipe starts to affect the pressure levels especially in the region of the pulsed drift tube and the entrance of the collision trap with a factor of about 20–40 compared to a factor of 10 between the input pressures. These results emphasize the requirement of an input pressure which should be as low as possible to achieve long-term storage.

A technique developed at CERN shows that, when you cover the cryostat inside with an approximately 100 nm thick carbon layer, the effective surface for cryopumping would increase drastically [198]. This carbon layer can only be applied to the walls of the cryostat, not on the pulsed drift tube or the electrodes. Coating the complete cryostat can prove to be very difficult, so it is also a possibility to just coat parts of it.

Figure 49 shows the on-axis number density with a carbon layer on the full cryostat except for the pulsed drift tube and the electrodes and as a comparison the number density assuming no carbon layer on any surface over time intervals of 30, 100 and 365 days. The carbon coating has a high impact on the on-axis number density in the entrance area of the cryostat and especially after long time intervals, as the higher effective surface for cryopumping significantly increases the time interval until the surfaces are saturated. In the region of the pulsed drift tube (between $z = 0.6$ m and $z = 0.8$ m) the carbon coating improves the number density by a factor of about 4 for long time intervals, while there is no significant gain in the region of both traps.

From the above COMSOL calculations, the following first conclusions can be drawn:

– A cryostat concept leading to a number density of residual hydrogen gas less than 20 particles per cubic centimeters for more than 100 days in the storage zone of the PUMA trap has been achieved with realistic vacuum conditions at the entrance of the 4 K region. A lower residual gas density in the collision zone could be reached with a 10^{-11} mbar vacuum at the entrance of the system for more than 100 days. In the case of a 10^{-10} mbar vacuum, the resulting number density in the collision zone is estimated to be around $100 \, \text{cm}^{-3}$ after 100 days.
– In the considered conditions, the one-atomic-layer surface coverage is not reached after 100 days. The on-axis vacuum in the trap can be improved by use of a 4-K shutter reducing the on-axis conductance at the entrance of the 4-K region.
– The results do not strongly depend on the sticking factor in a reasonable range of values: the vacuum in the
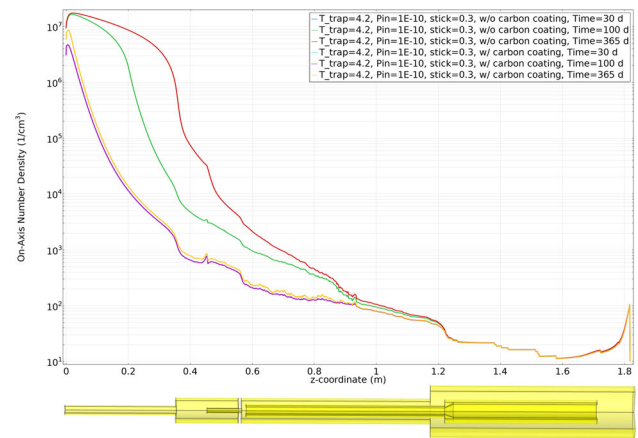

Fig. 49 On-axis H_2 number after 30, 100 and 365 days of particle flow through the pinhole ($z = 0$) with a radius of $f = 7.5$ mm into the cryostat for a wall temperature of 4.2 K and a sticking factor of $s = 0.3$ for the case of a carbon coated cryostat wall compared to an uncoated cryostat. The pressure at the entrance of the cryostat is 10^{-10} mbar. The curves for 30 days are covered by the ones for 100 days due to similar number densities. A 3D model of the cryostat is added for orientation

collision zone increases by a factor 2 from $s = 0.4$ to $s = 0.2$.
– The above conclusions depend on the hydrogen isotherm at low pressure. New measurements are under way.

4.7.9 Entrance of the PUMA frame

All simulations presented above aimed at determining the molecular hydrogen number density in a volume around the center axis of the cryostat, i.e. in the region of the PUMA setup which is at a temperature of 4 K. The starting point of these simulations is set to the entrance of the 4-K beam pipe and the requirements with respect to the input pressure and number density were defined with respect to this point in the setup. To investigate if an input number density in the order of a few 10^6 particles per cm^3 can be provided at the entrance of the 4-K beam pipe, a simplified cylindrical symmetric model of the upstream beam pipe within the PUMA frame is defined, which is then simulated with COMSOL. The aim of this model is to qualitatively estimate the evolution of the number density from the entrance of the PUMA frame up to the entrance of the 4-K beam pipe.

As an input pressure for this entrance region of the PUMA frame the nominal pressure of ELENA with a value of $1 \cdot 10^{-10}$ mbar is assumed. In addition, all surfaces within the model which are at room temperature (300 K) are subject to outgassing, while the release of hydrogen by all 50-K as well as 4-K elements is neglected due to the significantly lower diffusion coefficient within the materials. The outgassing rates of the 300-K surfaces are initially set to a value of $7 \cdot 10^{11}$ 1/s m^2, which corresponds to the outgassing rate of vacuum-fired stainless steel after 24 h of baking at 150
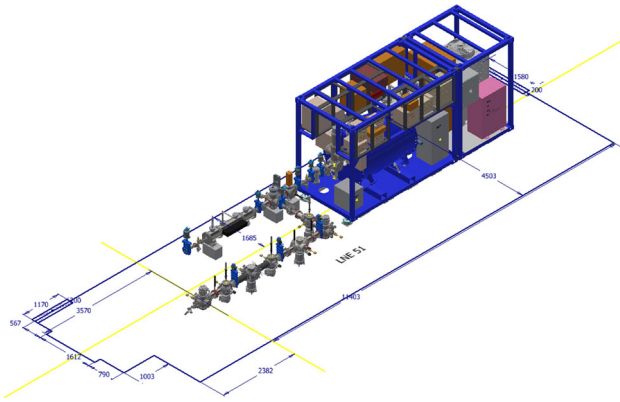
Fig. 50 Overview of the PUMA setup including the permanent installation at LNE51

°C for molecular hydrogen [221]. These outgassing rates can be reduced even further by baking the parts for longer time intervals and at higher temperature, which improves the overall on-axis number density.

The cold shutter, not inserted in the present simulation, will improve further the reduction of residual gas molecules entering the trap.

Infrared radiation from room temperature elements can lead to a hydrogen equilibrium pressure higher than expected. This is caused by the transmission through phonons from the substrate. Although the openings of the 4-K tube and the cold shutter are minimised, the remaining radiation passing through may not be negligible. A detailed estimate is planned for the near future. As a remedy to this potential problem, we will study the possibility of using a pre-condensation of a few monolayers of heavier gases such as suggested by Benvenuti and Calder [222].

5 PUMA at ELENA

5.1 Implementation at AD/ELENA

An overview of the PUMA experimental setup at the LNE51 beam line is shown in Fig. 50. The handover point from the machine to the experiment is located at 3.57 m from the upstream wall of the experimental zone.

The PUMA experimental beam line is composed of a pulsed drift tube (see Sect. 5.4.1) to slow down the antiprotons from 100 to 4 keV and an ion source system (see Sect. 5.4.2) for development and reference measurements at ELENA. The beam line is designed to fulfill the vacuum requirements (see Sect. 5.4.3) and provide an optimal antiproton transmission (see Sect. 5.4.4).

5.2 Experimental zone infrastructure

5.2.1 Electrical distribution

The PUMA experiment will have the specificity of moving back and forth between the AD and ISOLDE, typically twice per year. In the AD, the trap will be transported by the 50-ton crane onto a truck located at the loading platform in front of the transfer gate. During these transport operations, a number of systems must be powered without interruption. The requirements are therefore the following:

– While located in the experimental area and suspended from the crane: 70 kW (40 kW at 400 V - 3 phases, and 30 kW 240 V - 1 phase).
– Vital apparatus which cannot suffer any short power outage (trap electrodes, control circuit for the solenoid) will rely on a 100 kVA UPS in parallel with the main power grid. It is important that the disconnection and connection operations are totally transparent to the apparatus in terms of power supply since any power shortage would lead to the instantaneous loss of the antiprotons.

It is foreseen that a single UPS of 100 kVA is attached to the PUMA apparatus at all time. This UPS will then be the interface to the various power supplies and will guarantee no glitches at disconnection and connection operations.

In addition to the main power supply for the transportable device, five sets of 5 × 8 A single phase power plugs on the walls of the experimental area will be installed, together with a dedicated supply for the pulsed drift tube.

The analysis of the power cuts at AD in the previous years has shown that about three breakdowns with service disruption of more than 10 minutes (limit of the UPS considered) can be expected over a 12-month period. The occurrence of such an event during the operation of PUMA is unacceptable. For this reason, a diesel generator will be installed on a concrete slab, close to the AD hall connected to the supply switchboard of PUMA in order to ensure powering of the experiment even during long duration power cuts at ELENA. This generator will be part of CERN's contribution as it will serve the purpose of several experiments in the AD hall. Its detailed characteristics remain to be defined, but it shall be at minimum 100 kW, with 3 h autonomy.

A second diesel generator will be used for the transport phases and attached to the same trailer as the experiment during its transport.

A third generator will be connected to the ISOLDE main switchboard for PUMA to ensure service continuity when connected to ISOLDE, as detailed in Sect. 4.

5.2.2 Cooling water

Cooling water will be needed for the experiment, in particular for the cryocoolers. The total cooling capacity required is estimated to 50 kW. The water flow will be set to 40 liters per minute and the maximum temperature of the cooling water should be limited to 29 °C.

The transportable frame is equipped with a chiller, used for the cooling water in closed circuit during transportation. In case of power outage, it is foreseen that the chiller will start automatically, providing the necessary cooling for the PUMA operation.

5.3 LNE51 beamline: upstream the hand-over point

In the baseline design for LNE50 (transfer line to GBAR), sufficient space was allocated to install a fast switch and deflector to service other experimental stations on another beamline between GBAR and the ASACUSA laser room. The experimental station located on LNE51 would be suitable to be used by different future experiments with similar requirements.

5.3.1 Layout

The layout of the LNE51 design is presented in Fig. 51. A standard fast-switch and deflector (33.16°) ZDFA-ZDSA unit is used as the switching point from LNE50. The line is made compact enough to allow the integration of movable experiments, close to the transfer gate but far enough from the entrance door to the zone. To satisfy the integration constraints and match the beam to an experimental target at the end of the line, four extra quadrupole units (ZQNA) are needed along with a 37.7 ° standalone deflector (ZDSD). Two beam profile devices (BSGWA) are proposed for installation on LNE51 with the final profiler to be placed immediately upstream of the vacuum valve demarking the new experimental area. There is space on the LNE51 beamline for the installation of a fast-switching deflector unit (ZDFA-ZDS) opening up the possibility for another experimental station on LNE52.

The inventory of beamline elements for the LNE51 line is summarized in Table 10. The assembly of the LNE51 is under completion.

5.3.2 Ion-optics

The baseline ion-optics of LNE50 to GBAR was taken as the starting point and matched with the available quadrupoles in LNE51 to provide a beam spot size (rms) of approximately
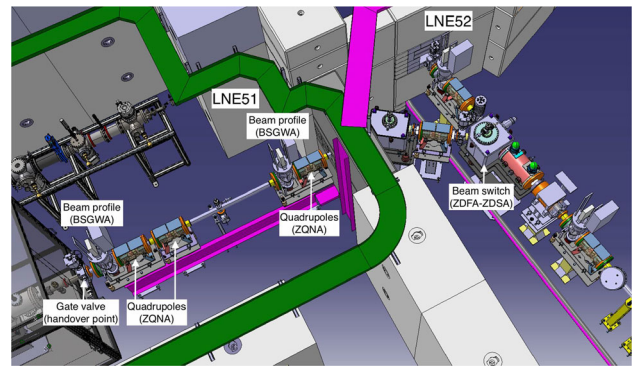

Fig. 51 View of the LNE51 beam line towards the PUMA/AD-9 experiment. See text for details

Table 10 Summary of beamline elements to be installed for LNE51

Unit	Quantity	Comment
ZDFA	1	Existing design
ZDSA	1	Angular bend of 33.16°. New design
ZDSQ	1	Angular bend of 37.69°. New design
ZQNA	4	Existing design
BSGWA	2	Existing design

Table 11 Summary of beamline elements to be installed for LNE51

Horiz. geometric emittance ($95\% = 6\epsilon_{rms}$)	6 mm mrad
Vert. geometric emittance ($95\% = 6\epsilon_{rms}$)	4 mm mrad
Momentum spread (95%, FW = $4\sigma_{rms}$)	$2.5 \cdot 10^{-3}$

2 mm at the experiment's focal point where,

$$\sigma_{x,y}(\text{rms}) = \sqrt{\frac{1}{6}\beta_{x,y}\epsilon_{x,y}(95\%) + \left(\frac{D_{x,y}}{4}\frac{\Delta p}{p}\right)^2} \qquad (35)$$

and $\Sigma_{x,y}(95\%) = \sqrt{6}\sigma_{x,y}.$ (36)

The assumed beam parameters are summarised in Table 11.

The beam dynamics in the new ZDSD deflector and the computation of its optical transfer matrix used in the MADX simulations can be found detailed at length in the CERN Optics Repository. The LNE51 matched optical functions along the transfer lines from ELENA extraction to the experimental target are shown in Fig. 52, where all quadrupoles are to be powered individually. The required quadrupole strengths remain well within the design specification of the hardware of ± 6 kV.

The RMS and 95% beam envelopes along the LNE51 transfer line and at the focal point (indicated by the black dashed line) are shown in Fig. 53 and are within the usual specifications of ELENA experiments.
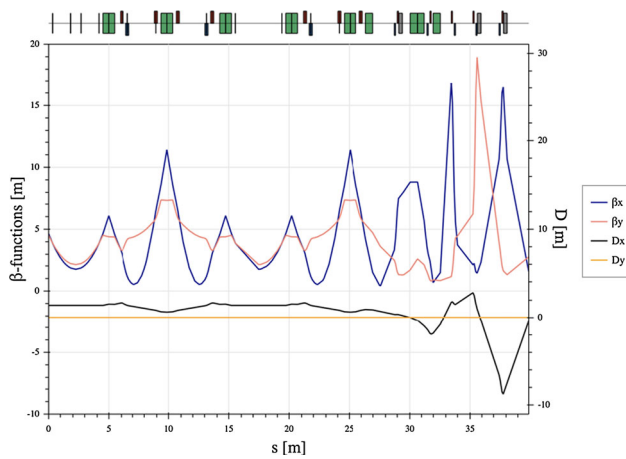
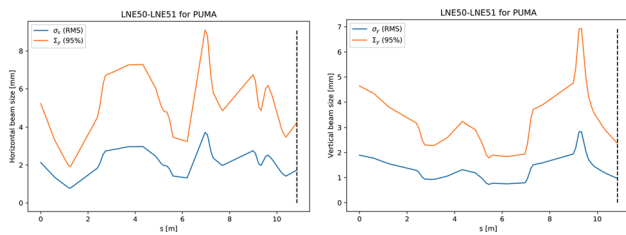**Fig. 52** Optical functions from the ELENA ring, through LNE50 and 51 to the hand-over point

Fig. 53 Horizontal (left) and vertical (right) RMS and 95% beam envelopes along LNE51 to the focal plane at the hand-over point
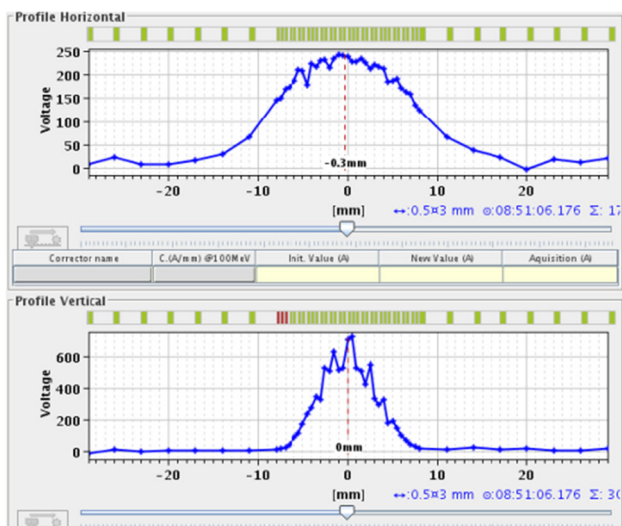

Fig. 54 Antiproton-beam profile measured with a SEM detector at the extraction of GBAR (LNE.50.BSGW.5020). Data taken on September 30, 2020

Some flexibility in the beam spot size is possible to welcome experiments with different requirements. Each request will be analysed on a case-by-case basis.

5.3.3 Diagnostics

The beam diagnostics will be provided by two Secondary Emission Monitors (SEM), of the same type as installed in other ELENA transfer lines. These SEM (naming code BSGWA in ELENA context) have the particularity of being bakeable at a temperature of 180 °C and present a standard low outgassing of 10^{-8} mbar l/s after bakeout. Having fixed-position SEMs is also under consideration: by removing the bellow, the wall surface will be reduced significantly and one could expect a reduction of about 20% for the outgassing rate (to be confirmed by measurement). The internal grid intercepts about 2% of the antiproton beam only and is movable in and out of the beam trajectory. The SEM provides a profile of the beam in horizontal and vertical directions.

5.3.4 Vacuum

The vacuum system considered for LNE51 is of a similar type as used for other ELENA transfer lines, with standard opening of 63 mm and with stringent requirements on the vacuum level to be achieved. The pressure in the ELENA ring that is fully NEG coated is typically of a few 10^{-12} mbar. Transfer lines are pumped by portable turbomolecular movable pumping groups and combined ion and NEG pumps. The line is fully baked with in-situ permanently installed bake-out jackets.

Only the last segment before the handover point to the experiment (typically 1 m) is NEG coated, so that the pressure is $< 10^{-10}$ mbar.

The pressure monitoring system is connected to the general ELENA vacuum control system. A specific gauge located close to the experiment will trigger a fast vacuum valve in LNE50 transfer line to protect the ELENA machine from any accidental air inlet in PUMA while the interface gate valve is open.

Also, this interface gate valve is interlocked with the access safety system that will trigger a closure of the valve as soon as the experimental area is being accessed, to limit the risk of accidental venting.

5.4 LNE51 beamline: downstream the hand-over point

5.4.1 Pulsed drift tube

The antiprotons from ELENA will be decelerated from 100 keV to 4 keV using the same pulsed drift tube (PDT) technique as employed by the GBAR experiment. This technique relies on the electrostatic deceleration of the antiprotons pulses by switching a drift tube from − 96 kV to ground while particles are travelling through.

At CERN, antiparticle beams are transported at ground potential. When a beam with a kinetic energy E_i arrives in
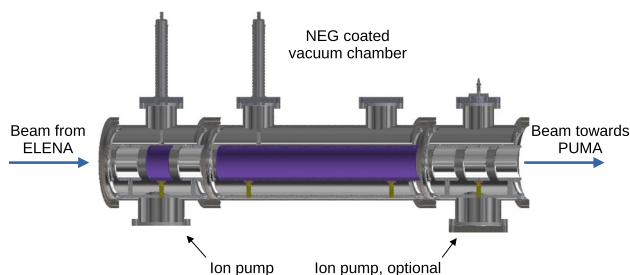
Fig. 55 Design of the Pulsed Drift Tube chamber. The purple electrodes are on high voltage, yellow indicates the boron nitride insulators

the vicinity of the drift electrode polarized at a potential V, the electric gradient at the entrance decelerates the charged particles. Inside the drift tube, antiprotons travel through with a remaining energy of $E_f = E_i - \frac{V}{e}$. Since the longitudinal potential in the tube is flat at first order, the pulse feels no gradient of potential. The voltage applied on the drift tube can then be switched from -96 kV to ground. When exiting the tube, the decelerated antiprotons do not feel any re-accelerating gradient. Following Liouville's theorem, the emittance of the beam will blow up during the deceleration process. To counterbalance the increase of the emittance at the entrance of PUMA, upstream optics are necessary. The GBAR experiment uses a six electrodes pre-decelerating system designed for more flexibility in the potential shape at the entrance. Based on a similar system, simulations [223] have shown that a much simpler design based on telescopic optics should be sufficient. We will implement a simple and compact einzel lens-based design at the entrance and exit of the drift tube. The design of the pulsed drift tube for PUMA is shown in Fig. 55.

A deceleration down to 4 keV results in an increase of the transversal emittance of a factor 5. The PUMA project proposes a two step deceleration: first, in a dedicated apparatus, from 100 keV to 4 keV for a better beam definition and, second, using a smaller pulsed drift tube in the solenoid field from 4 keV to few hundreds of eV taking advantage of the magnetic field for the radial confinement of the antiprotons. The antiprotons then can be caught by electrodes to which up to 500 V can be applied.

Previous experience with pulsed tube deceleration has shown very good efficiency up to 80% with heavy ion beams [224,225]. Such efficiency is achievable in the framework of the PUMA project (see Sect. 5.4.4). The current design of the Pulsed Drift Tube (PDT) integrates an injection einzel lens, the drift tube electrode and a second refocusing einzel lens. Both einzel lenses' electrodes have a diameter of 100 mm. Such a diameter is necessary to accept the decelerated beam without suffering from edge effects. The electrodes are 80 mm long with a gap of 30 mm. The bunch length is expected to be 300 ns (95%) at 100 keV. It corresponds to a

bunch length of 1.3 m. When decelerated to 4 keV, the bunch length shrinks to 29 cm, which is small compared to the 700 mm drift tube. To make the PDT high voltage compatible particular attention was paid to the shielding of the triple junctions (vacuum-insulator-electrode intersection) and avoiding any sharp edges or corners.

5.4.2 Ion source

In order to perform reference measurements with a broad variety of stable nuclei at ELENA, a pulsed ion source system is under development. An electron-impact plasma ion source for the ionization of different gases will be employed in the beginning but also a laser ablation ion source is supposed to be used in the future to gain access to a broader variety of stable ion species. A commercial differentially pumped plasma ion source (model IEQ 12/38 from SPECS) is currently used leading to a vacuum of about 10^{-9} mbar at the extraction tip of the source. The extraction potential of the source is tunable for ion energies up to 5 kV. The source furthermore offers a sub-millimeter beam spot at a tunable focal position.

Such ion sources do not generate a single-species ion beam, depending of the gas that is used. Other undesired ions must be separated from the ions of interest. This will be done by using a multi-reflection time-of-flight mass separator (MR-ToF MS) into which a bunched beam of different ions can be injected. The flight-path of the ions will be prolonged significantly due to the use of electrostatic mirrors. The ions are then separated in their time-of-flight according to their mass-over-charge ratio m/q and a single ion species can then be extracted from it [226].

The purified ion bunch is then accumulated and cooled in a RFQ cooler-buncher before the ion package is injected into the PUMA trap. For this purpose, a new linear quadrupole radio-frequency cooler-buncher will be commissioned which was developed by the collaboration of the Multi Ion Reflection Apparatus for Collinear Laser Spectroscopy (MIRA-CLS) [227] and build at the TU Darmstadt. Previous experiences with linear Paul traps using buffer gas cooling, e.g. ISCOOL [228] or at the ISOLTRAP [229] at ISOLDE, showed emittances of few π mm mrad at beam energies of 30 kV. We aim for an accumulation of about 10^4 purified ions per bunch [230]. The mass separated ion bunches coming from the MR-ToF MS have an energy of several keV which complicates trapping them in the Paul trap for a low-voltage regime. To modify the ions energy before and after the Paul trap accordingly, two PDTs are used to first decelerate them to an energy of several eV and then, after the extraction, re-accelerate for an efficient transport towards the PUMA traps.

When exiting the ion source, a fraction of the ions suffer recombination processes. This neutral component of the beam would have a damaging effect on the trapped antiproton plasma and must be removed. For this purpose, we imple-
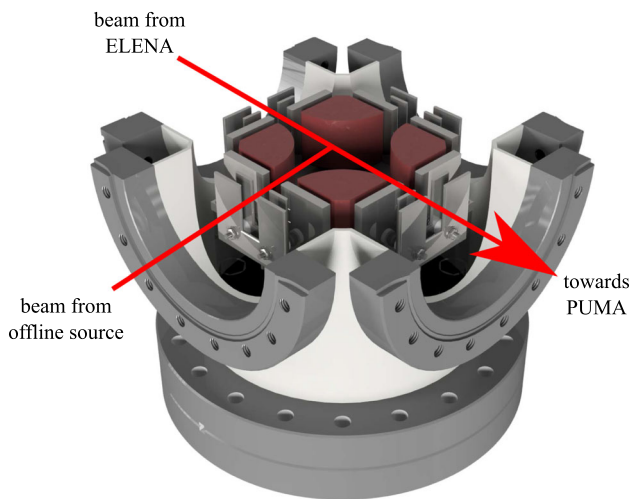
Fig. 56 CAD representation of a quadrupole bender which is planned to be used for the implementation of the offline ion source of PUMA while being located at ELENA

Fig. 57 Beamline at ELENA from hand-over point (left) to PUMA (right). Indicated are the locations of the ion and NEG pumps

ment the pulsed source system perpendicularly to the main antiproton line. An electrostatic quadrupole bender (see Fig. 56) bends the ion trajectory with a 90° angle.

The bender will suppress the transmission of neutral species from the beam since only charged particles undergo the 90° bending. In addition, such electrostatic quadrupole will offer the opportunity to supply the PUMA trap with two different types of particles without any mechanical operations. When the electrodes of the bender are not polarized, the antiproton beam coming from ELENA will pass through it without being affected and when the electrodes are polarized, the PUMA trap will be supplied with the ions coming from the pulsed source system. Due to space constraints at ELENA, a second quadrupole bender is foreseen in the offline ion-source beam line to adapt it to the available space. Additionally, manually controllable iris shutter will be installed along the ion source beamline to separate the sections with different vacuum requirements.

5.4.3 Vacuum

To estimate the pressure in front of the last gate valve before the PUMA frame starts (see Fig. 57), the beamline at ELENA was modeled with the software MOLFLOW [231].

The goal was to determine the pressure in front of the last gate valve when it is closed. The following assumptions were made:

– Only hydrogen is considered.
– Where possible, NEG coating is applied. This includes crosses, beampipes, and the vacuum tube of the pulse drift tube (CF DN250). A pumping speed of 0.044 l/s/cm^2 (sticking factor $1 \cdot 10^{-3}$) was assumed.
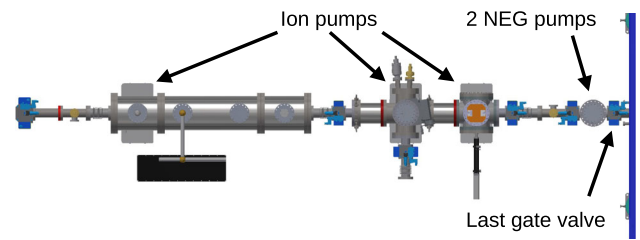
– Other surfaces of the beampipe are stainless steel and have an outgassing rate per surface unit of $5 \cdot 10^{-12}$ mbar l/s/cm^2.
– All other components have an outgassing rate of $1 \cdot 10^{-8}$ mbar l/s[5], except the pulse drift tube ($1 \cdot 10^{-7}$ mbar l/s) and the extractor gauges ($1 \cdot 10^{-9}$ mbar l/s [232]).
– 2 NEG pumps with a pumping speed of 1000 l/s for H_2 each.
– 3 ion pumps with a pumping speed of 240 l/s for H_2 each.

With these assumptions the MOLFLOW simulation gives a pressure at the last gate valve of about $2 \cdot 10^{-11}$ mbar.

The main determining point for the pressure at the last gate valve comes from the outgassing of the valve itself. This was conservatively estimated to be $1 \cdot 10^{-8}$ mbar l/s. However, the outgassing can be reduced drastically [233], for example by repetitive baking. If the outgassing of the valves can be reduced to $1 \cdot 10^{-9}$ mbar l/s, the MOLFLOW simulation gives a vacuum pressure of $1 \cdot 10^{-11}$ mbar.

5.4.4 Beam optics

The overall goal of the LNE51 beamline is to provide as many antiprotons as possible to the PUMA experiment, which requires a precise tuning of the beamline elements. To minimize the losses of antiprotons per bunch, the evolution of the longitudinal and transversal spread of an incoming antiproton bunch within the beamline have to be investigated and tuned. The longitudinal spread of the incoming antiproton bunch is defined by the bunch length of 75 ns (rms) in ELENA at the nominal kinetic energy of 100 keV, while the transversal spread of the beam is defined by the horizontal emittance of $\epsilon_h \approx 6(\pi)$ mm mrad and the vertical emittance of $\epsilon_v \approx 4(\pi)$ mm mrad for about 95% of the Gaussian beam.

Within the first pulsed drift tube the antiproton energy is reduced from 100 keV to about 4 keV. This deceleration leads to a shrinking in the longitudinal spatial extension by a factor of 5, but at the same time the transversal emittance is increased by about the same factor. This increase in transversal emittance as well as bunch length and energy
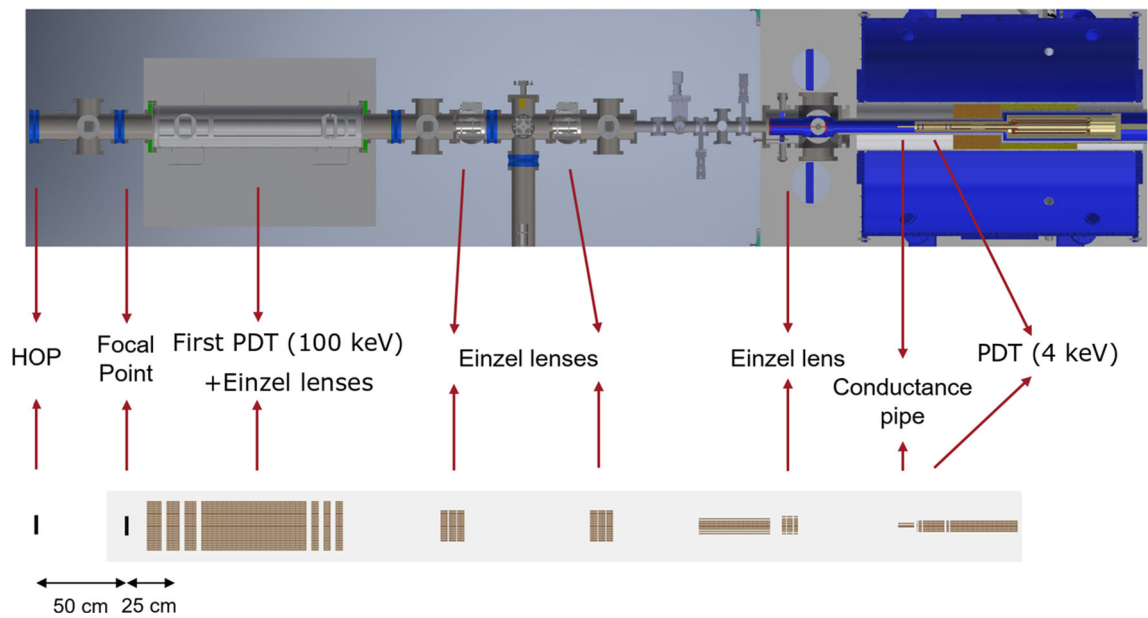
---

[5] Reference value of SEM grid from ELENA.

Fig. 58 Overview over the full set of electrodes included in the geometry file for the simulation of the antiproton transmission

spread effects in the finite length pulse drift tube are the main sources of antiproton losses within the antiproton beamline. To quantify the losses caused by those two effects and the total transmission of antiprotons into the storage region of the PUMA setup, ion optics simulations based on SIMION were performed.

The baseline of all presented simulations is the definition of the geometry file, which summarizes the shape of all electrodes within the beamline. The main ion optical elements, which tune the antiproton trajectories within the LNE51 beamline between the handover point and the storage zone within the PUMA trap setup are the two pulsed drift tubes used for the deceleration from 100 keV down to about 250 eV and different einzel lenses (two in the beamline, one at the start of the PUMA frame). An overview over the full geometry (except for the grounded beam pipe) for the investigation of the antiproton transmission is shown in Fig. 58.

After the definition of the electrode dimensions, the initial properties of the particles that propagate through the beamline have to be defined, i.e. the initial positions and momenta of each particle and their respective charge. In the case of the antiproton simulations, these values were defined on the basis of Gaussian distributions in the time-of-birth (TOB) and momentum space to mimic a bunch effect.

For the simulation of the ion optics from ELENA up to the PUMA trapping region two different programs are used, treating on the one hand the antiproton transfer from the ELENA ring up to the focal point by MAD-X, while on the other hand the antiproton propagation downstream of the focal point with the time-dependent deceleration in the pulsed

drift tubes is treated with SIMION. In case of MAD-X, the transversal beam shape is defined based on Twiss parameters, which represent the shape of the phase space ellipses in the horizontal x–x'-plane and the vertical y–y'-plane. These phase space ellipses are in our case defined in such a way that 95% of the particles are contained within this phase space area. In contrast to this, SIMION cannot initialize particles based on Twiss parameters, but requires a definition of the distributions in each of the six dimensions, which are energy offset ΔE, time offset Δt, horizontal and vertical offset (x any y) and horizontal and vertical divergence angle (x' and y') relative to the nominal particle.

The first step to match both interfaces is to determine acceptance plots, which plot the initial particle properties only in case a particle is transmitted into the trapping region and sufficiently decelerated. These plots are determined by covering a large phase space of initial parameters. In case of the longitudinal ΔE-Δt transmission plot, the distribution of the transmitted particles is highly asymmetric with respect to the zero point (see Fig. 59), which is caused by the non-uniform deceleration in the pulsed drift tubes (low-energy region) and the strict maximum trapping energy (sharp edge in the high-energy region). However, the longitudinal phase space of the antiproton bunch coming from ELENA is fixed by $\Delta t_{rms} = 75$ ns and $\Delta E_{rms} = 100$ eV and cannot be adjusted by the ion optical elements.

The transmission plots for the transversal phase space can be used as interface between the MAD-X simulation and the SIMION simulation. Due to the full cylindrical symmetry of all ion optical elements downstream of the focal point the acceptance plots in the x-x' and the y-y' plane are similar (see
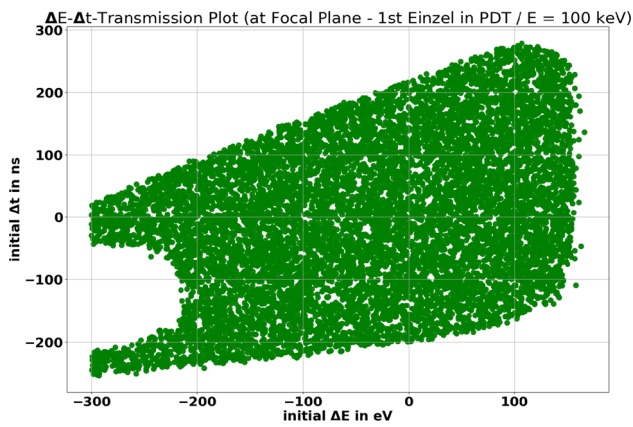
Fig. 59 Transmission plot for the longitudinal ΔE-Δt phase space

Table 12 Summary of the Twiss parameters determined by the transversal transmission plots

Twiss Parameter	Unit	Value
$\epsilon_{x/y}$	mm mrad	60
$\beta_{x/y}$	mm/mrad	1.40
$\gamma_{x/y}$	mrad/mm	0.87
$\alpha_{x/y}$		0.46

Fig. 60 Transmission plots for the transversal x–x' and y–y' phase space. Phase space ellipse representing an estimated 2σ-interval of a Gaussian were added for defining suitable Twiss parameters at the focal point

Fig. 59). In both cases, the transmitted particles do not follow a sharp ellipse, but rather a swirl-shaped distribution with smaller transmission rates for highly off-centered particles. Thus, only the area of high transmission density close to the zero point was taken into account for the definition of the estimated 2σ-emittance ellipse. The Twiss parameter of this fitted emittance ellipse are summarized in Table 12. Based on the area of the ellipse, i.e. the emittance, and the widths of the distributions $\sigma_{x/y}$ and $\sigma_{x'/y'}$, respectively, the correlation coefficient of the tilted phase space ellipsis can be determined as

$$\rho_{xx'/yy'} = \sqrt{1 - \frac{\epsilon_{x/y}}{\sigma_{x/y} \cdot \sigma_{x'/y'}}} = -0.3.$$

The determined Twiss parameters are then used as a boundary condition for the optimization of the ion optics settings upstream the focal point in MAD-X. In the following MAD-X simulation it was found that it is possible to provide a beam with the stated Twiss parameters at the focal point, with a horizontal emittance of about 8 mm mrad and a vertical emittance of about 6 mm mrad.

For the investigation of the antiproton transmission, the voltages of the einzel lenses and the PDTs are optimized. In case of the two pulsed drift tubes, the voltages are currently ramped instantaneously after a certain time of flight of the particles. As the particles are initialized at different times, representing the longitudinal bunch length, the particles are then decelerated at different locations within the PDTs. In
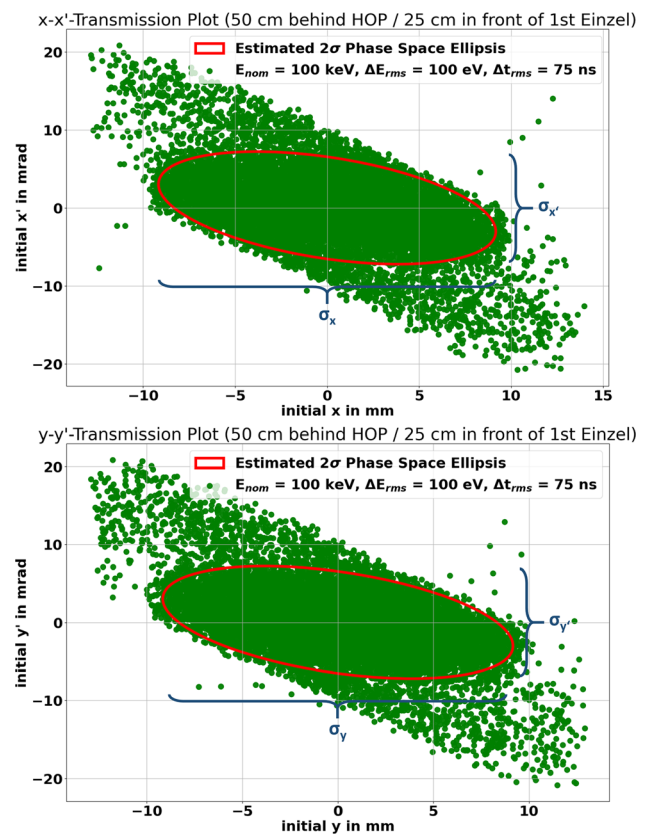
the corresponding simulations it was found that the pulsing of the two PDTs has to be performed within a time interval of about 200 ns to avoid significant losses.

The optimization of the voltages led to the conclusion that all electrodes behind the first PDT are set to voltages below 6 kV, which allows the use of standard cables and controllers. The einzel lens directly in front of the first PDT and the following PDT are in contrast set to voltages of −88.5 kV and −96.0 kV, which makes the implementation of a Faraday field cage around the PDT setup necessary.

After the optimization of the voltages, input beams with the Twiss parameters determined by the transmission plots and different emittances are defined to determine the robustness of the system with respect to the beam size. For each simulation, the beam is assumed to be perfectly centered, i.e. there is no transversal offset from the center line, and the nominal widths for the bunch length and the energy spread are assumed for the longitudinal dimensions. Besides the nominal emittances of 6 mm mrad in horizontal direction and 4 mm mrad in vertical direction, the cases with four times and ten times of the nominal emittance were also investigated. The transmissions reached for the different emittances are summarized in Table 13.

Table 13 Antiproton transmission into the PUMA trap for different horizontal and vertical input emittances without transversal offset

Horizontal [mm mrad]	Vertical [mm mrad]	Transmission [%]
6	4	95.5
24	16	87.3
60	40	54.4
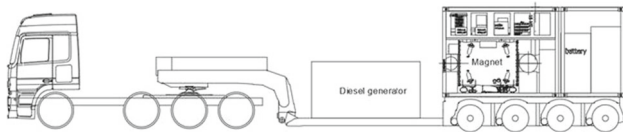
Fig. 61 Sketch of truck configuration for the transport from ELENA to ISOLDE

It can be concluded that the transmission of antiprotons is limited to a maximum value of about 95.5% by the longitudinal component, while additional losses arise if the transversal beam size is significantly larger than the nominal value. Assuming a centered beam, the beamline would allow emittances up to about three times the nominal values so that a transmission of at least 90% is reached, while the emittances should be smaller to compensate for potential transversal offsets.

6 Transportation

6.1 General overview

PUMA is a transportable experiment with the specific requirement to remain under operation during the transport phase since the storage of antiprotons requires the full operation of the Penning trap. The transfer of PUMA will take place between the ELENA experimental area (building 193) and the ISOLDE experimental hall (building 170) at CERN.

Once PUMA is loaded on a trailer and during transport, the experiment will be powered by an external diesel generator. A sketch of the truck configuration is shown in Fig. 61. So far, a solution that allows to compensate the road inclination along the itinerary is taken in consideration. The frame will be equipped with sensors to record the acceleration and vibration history of PUMA during the transport. Transport of fragile large-size objects, such as accelerating cavities, have often been performed at CERN (i.e. HIE ISOLDE RF cavities). Note that the demonstration of transporting trapped charged particles was made more than twenty years ago: an electron cloud in a Penning trap was transported by truck over 5000 kilometers from the west coast to the east coast of the USA [193].

6.2 Powering procedure

The power consumption of PUMA is estimated to 70 kW in operation during transport (20 kW of chiller power consumption to be added to the 50 kW of on-site operation of the system). The transport time from ELENA to ISOLDE is estimated to last one to two hours. A powering exclusively from batteries is excluded. PUMA will always be connected to an external source of power.

The electrical power supply is equipped with a power transfer switch, allowing to change the power connection between different grids. The outlet of the power transfer switch is connected to the UPS. All equipment on the frame is supplied via the UPS, therefore a change of the power supply to the magnet is without interruption. When supplied from a generator, the generator needs to be in grid configuration TN[6]. PE (Protective Earth) of the frame needs to be screw-connected either to ground or to PE of the generator.

During the transport phase, the generator will be in IT configuration.

6.3 Operations at ELENA

A first operation is the transfer of the PUMA experiment from its experimental location at ELENA to the trailer. This operation will be performed by the overhead crane. The AD hall is equipped with 50-ton cranes which are suited for this operation.

The transfer of PUMA to the trailer will be performed according to the following steps:

- At the end of the collection of antiprotons, the three gate valves in front of the PUMA setup are closed while the 4-K beam shutter in front of the 4-K cryostat entrance is in "close" position. The last two gate vales remain attached to PUMA, while the first one is disconnected from PUMA. At this stage, the PUMA frame is not connected anymore to the ELENA beamline.
- The slings and spreader beam are attached to the PUMA frame (main and annex attached together). Twist-lock container connectors attached to the inner container corners. The frame shall only be lifted at the bottom corners using container lifting hooks.
- The ELENA generator is disconnected from the distribution panel of PUMA, and the grid-power cable running from the crane is connected. Providing a 70 kW power from the crane requires a modification of the present equipment. The crane will be equipped with a specific power line and a cable reeler to supply the power to the experiment.

---

[6] From french: terre neutre.

– The power source is then switched from the floor grid power to the crane grid power.
– The wire-rope damping system is unlocked.
– The cooling water flow is switched from the ELENA distribution to the chiller. Water pipes are disconnected.
– The PUMA experiment is craned from its experimental position at LNE51 to the trailer at the delivery zone.
– The transportable generator is connected to the power distribution panel of PUMA. The generator is switched on, and the power is switched from the crane grid-power source to the generator. The grid power cable is disconnected.
– Slings are detached, and the crane removed. The frame of PUMA is fixed to the trailer. PUMA is ready to be transported.

A dedicated lifting beam for PUMA frame is being developed to be compatible with the cranes at ELENA. A dedicated low-headroom spreader beam satisfies the maximum height available for the crane operation which is limited to 3.67 m at ELENA (available space over the AD ring shielding), as illustrated in Fig. 62. The lifting beam will have adjustment capability to adjust the position of the gravity center according to the exact position of the center of gravity.

The space available in the AD hall is sufficient to handle the two joint modules of the PUMA experiment in terms of length and height. The size of the door at this location is 5.5 m height and 6 meter width. The distance between the door and the shielding wall is 6 meters.

6.4 From ELENA to ISOLDE

6.4.1 Path

The foreseen itinerary is 2 km long and is shown in Fig. 7. The heavy weight of the experiment and the expected length of the convoy prevent from considering a shorter itinerary. The current itinerary implies slopes up to 6% ($\sim 3.4°$) in both directions. Changes of direction will require careful adjustments of the trajectory as it implies changes of slope in both directions at the same time. The estimated time to complete the travel between the two locations is 60 min. The overall handling operation from its position in the ELENA beamline to the ISOLDE beamline is estimated to 4 h. The road along this path is in relatively good condition and most of the asphalt has been replaced during the last 5 years. The road will be inspected a couple of weeks ahead of the transport to identify and request repair of possible defective drainage covers and holes in the road to ensure a safe and smooth transport.
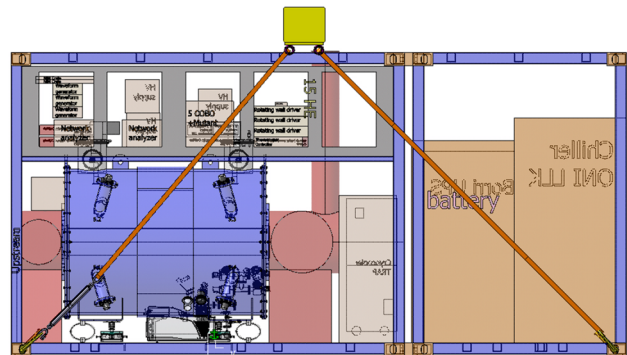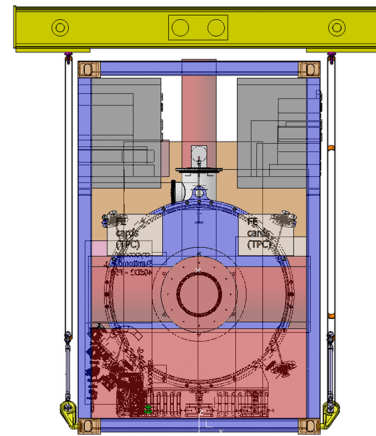

Fig. 62 Preliminary design of the spreader beam for the PUMA frame. 3D model by M. Perez Ornedo, CERN

6.4.2 Convoy

The convoy will consist of a tow tractor with a low bed trailer. The tow tractor used for this transport will be equipped with a hydraulic converter to regulate the speed during the overall transport. The trailer used for this operation will have hydraulic axles compensation to have a better damping and some capability to minimize the pan and tilt during the transport. The experiment will be loaded on the rear of the truck to allow the off loading operations at ISOLDE. The speed will be limited to 5 km/h as such minimizing the effects of vibrations, acceleration and deceleration. In addition to prevent hard braking on the road the convoy will be escorted (front and back) to ensure a smooth travel from AD the ISOLDE.

A waterproof tarp will be adapted to the PUMA frame geometry to protect the system against rain. Custom openings will be foreseen for a proper operation of the chiller and warm air evacuation.

6.4.3 Vibrations during transport and handling

Particular precaution during transport will be taken to avoid having vibrations which could disturb the equipment. This
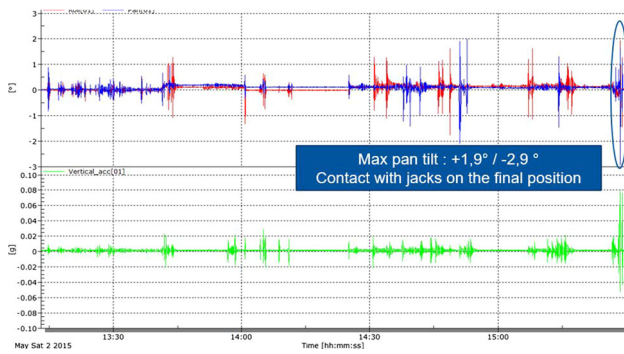
Fig. 63 Tilt and acceleration monitoring during the handling and transport of HIE-ISOLDE cavities

has been demonstrated during the transport of various sensible objects at CERN such as the HIE ISOLDE cryomodules. The range of possible expected accelerations during transport and handling are in the range of ± 0.1 g. Figure 63 shows the record of tilt and acceleration during the transport between SM18 and ISOLDE of one HIE ISOLDE cryomodule.

To prevent the possible perturbation of the experiment by the vibrations caused by the generator, the generator will be placed on damping pads.

6.5 Operations at ISOLDE

Space is limited at the entrance of the ISOLDE experimental hall. It was checked that PUMA can be delivered and transported to its final position without modification of the overall infrastructure at the exception of the crane. The delivery of the PUMA experiment will be done driving backward the trailer below the crane hook which will be already equipped with the lifting beam. From this point the frame will be connected to the lifting beam with the container hooks in the four corners. The load will be moved off from the trailer. Then, the trailer will be moved out of the way. Finally, the frame will be rotated in situ to be positioned at 90 degrees from the entrance. This allows the full insertion of the experiment in the ISOLDE hall. From this point the frame will be raised to pass over the HIE ISOLDE beam lines up to it final position.

The installation of the PUMA device to its experimental location at ISOLDE will be done with the overhead crane of the building. The existing crane is limited to a lifting capacity of 10 tons, while the total weight of PUMA is currently estimated to be 9.7 tons (lifting beam not included). The crane will be equipped with a similar system as the one foreseen at AD to supply the power to the experiment from the crane. A dedicated lifting beam for the PUMA frame is being developed to be compatible with the crane at ISOLDE. A dedicated low-headroom spreader beam satisfies the maximum height available for the crane operation. This lifting device will have the same feature as the one designed for AD. The only difference between the two lifting beams is the interface

Table 14 Requirements for the radioactive ions beams at the entrance of PUMA

Isotopic purity	$> 99\%$
Beam diameter	< 5 mm
Transverse emittance at 30–60 keV	$< 50\pi$ mm mrad
Energy	1–2 keV
Energy spread	± 30 eV
Bunch length	< 15 cm
Longitudinal emittance (^{18}Ne @ 2 keV)	$< 30\,\mu$ seV

with the hook of the cranes as the two cranes have slightly different crane-hook sizes. The final exact position will be identified on the floor with reference points to allow an easy and efficient prepositioning with the crane (± 1 cm respect to the final positioning).

6.5.1 Connection to beam line

The connection to the beam line follows the operations at ELENA in reverse order, with one difference related to the vacuum. Once the transported setup is connected to the vacuum beam line at ISOLDE, the venting valve is pumped, baked and the NEG coating is activated. Once a sufficient vacuum is reached, the gate valves can be opened.

7 Installation at ISOLDE

7.1 General overview

In the following a brief description of ISOLDE and the production rates of the radioactive isotopes proposed as first physics cases for PUMA are given. The beam energy, time structure, purity and emittance requirements for PUMA are demanding. They are summarized in Table 14. These requirements can be achieved with a system similar to the ongoing MIRACLS [227,234] project, downstream the ISCOOL buncher [235]. The two apparatus are introduced, and their current status of development is given.

In the ISOLDE experimental hall (building 170), only one position for the PUMA experiment appears to fulfill all requirements. The space identified for PUMA is located downstream of the RCX10 line, where the recently-removed NICOLE experiment was formerly installed, as well as additional space in the HIE ISOLDE part of the experimental hall for the PUMA setup itself.

The multireflection time-of-flight mass separator (MR-ToF MS) of MIRACLS [236] or a similar system will be followed by a cooler buncher based on the design of ISCOOL. MIRACLS' MR-ToF system will provide RIBs with the necessary beam requirements at the entrance of the PUMA
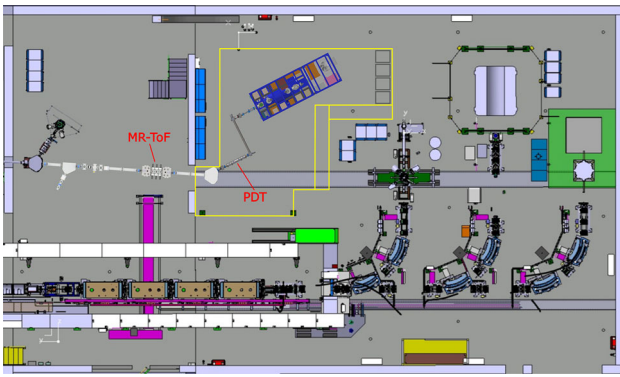
Fig. 64 General view of the ISOLDE hall with the new MIRACLS and PUMA experimental area

experiment which will be located in the HIE ISOLDE part of the experimental hall.

7.2 Infrastructure of the experimental zone

This proposed location is ideal with respect to the specific case of PUMA as a movable experiment: spacing and infrastructure is available and overhead crane (10 ton) operation is guaranteed. The opening in the wall necessary to move from the Low Energy RCX beamline into the HIE ISOLDE part of the hall as well as a sufficiently large trench for routing cooling-water hoses already exists.

A layout of the ISOLDE experimental zone is shown in Fig. 64. The left part is dedicated to low-energy experiments while the more recent experimental zone (on the right) is dedicated to high energy experiments after re-acceleration by the HIE ISOLDE linear accelerator. A possible layout of the PUMA beamline is schematically represented.

The PUMA experiment will have the specificity to be moved back and forth between the AD and ISOLDE. During these transport operations the PUMA trap must be powered without interruption in order not to lose the stored antiprotons. The same is valid for any other interruptions such as unforeseen power-cuts while in operation.

The power generator to be used on the truck during transport will also serve as a backup power group both at the AD as well as at ISOLDE. This power generator will automatically start when a power cut occurs. The earlier described UPS will cover any sudden power interruption whereas the power generator will guarantee power for a large number of hours in case of more than just a glitch and power interruptions longer than the UPS lifetime of 10 min.

7.3 Radioactive beams

7.3.1 Production

The on-line isotope separation (ISOL) technique is a powerful method to produce pure low-energy radioactive-ion beams. High-energy light particles from accelerators or nuclear reactors impinge onto a heavy-ion production target. Many different isotopes are then created from several reaction mechanisms such as fission, fragmentation or spallation. In the ISOL method, the reaction products are stopped in the bulk of the target material. They then diffuse and effuse out of the heated target to an ion source section where they are ionized. Each element, with its specific chemical properties, requires an optimisation of the production target ensemble and of the ionisation process. ISOLDE at CERN has been a worldwide leading facility in the production of radioactive ion beams using the ISOL technique [237,238]. At ISOLDE, the radioactive isotopes are produced from the interaction of a 1.4 GeV proton beam delivered by the PS Booster at a maximum intensity of 3.2×10^{13} protons per pulse. The repetition rate is typically on the order of one Hz. Today, at ISOLDE, about 600 isotopes of more than 60 elements are available. Radiochemical methods and ionisation techniques have been developed for the majority of them. These radioactive ion beams with half-lives down to a few milliseconds can be delivered in intensities ranging from 10^{11} to 0.1 per second. In addition to the advantage of being close to ELENA, the unique range of low energy radioactive isotopes and highly competitive beam intensities make ISOLDE a perfectly suited facility where the PUMA physics program can be carried out.

ISOLDE has two on-line isotope separators with independent target-ion source systems that deliver 60 keV mass separated radioactive ion beams with a typical emittance of 25 to 35 π mm mrad [239]. The high-resolution separator (HRS) is theoretically able to separate the isotopes of interest from unwanted ions with a mass resolving power of up to 1.5×10^4 [240]. Since PUMA requires isotopically pure beams at a level of a percent, this separation is not enough for medium-mass nuclei. This aspect is further discussed in the following. The beam intensities for the isotopes of interest to be studied with PUMA at ISOLDE are presented in Table 15.

With the above yields, the measurements are feasible. Note that few isotopes of particular interest are not reachable at ISOLDE: the hypothetical *p-wave* halos ^{31}Ne and ^{37}Mg are currently not sufficiently produced since their expected rates are less than 1 s^{-1}. PUMA will benefit from any future improvement of rates at ISOLDE.

Table 15 Radioactive ion beam yields and primary target material at ISOLDE facility for isotopes targeted by PUMA

Nuclei	Yield (ions/μC)	Target
^{6,8}He	5.4×10^7 / 4.7×10^5	BeO - UC$_x$
^{7,9,11}Li	8.2×10^9 / 3.9×10^6 / 1.4×10^3	UC$_x$
^{8}B	300	C
^{17,18}Ne	4.5×10^3 / 3.5×10^6	MgO
...	...	...
^{26,27}Ne	4.9×10^4 / 200	UC$_x$
$^{28,...,33,34}$Mg	3.6×10^7 / ... / 3×10^3 / 140	SiC$_x$ / UC$_x$
$^{19-22}$O	1.3×10^5 / 3.4×10^4 / 7×10^3 / 1.3×10^3	UC$_x$
^{105}Sn	8×10^4	LaC
...	...	...
^{136,137,138}Sn	4×10^3 / 100 / 2.5	UC$_x$

7.3.2 Negative ion beams

At radioactive ion beam facilities, some isotopes are available as negative ions. Negative ion beams of the halogens chlorine, bromine and iodine were among the first ones which were used at ISOLDE [241]. These were ionized using a negative surface ion source, although such sources are limited to elements which have a high electron affinity. A different approach to create negative ion beams is to use charge exchange reactions to convert the incoming positive ion beam in, for example, a cesium vapor charge-exchange cell, into a negative ion beam. This has been applied to light nuclei from helium to chlorine [242] but also the efficiency for heavier isotopes like arsenic, selenium, tin, strontium and rubidium has been investigated at HRIBF at ORNL [243]. Using this technique, a conversion efficiency of 41% for tin beams was reported [244], putting exotic tin beams onto the list of possible candidates for experiments with PUMA either using the positive or the negative mixing scheme with the p̄. Furthermore, a dedicated development program is ongoing at ISOLDE to increase the variety of negative ion beams [244–246], which established astatine and resulted in the first measurement of its electron affinity [247].

For the first measurements at ELENA, an offline ion source, capable of producing positive and negative ions is foreseen. A versatile approach is to utilize a laser at 532 nm to create positive as well as negative ions by ablation from a solid target material. Such sources coupled to a MR-ToF MS have been used at Greifswald university [248]. Using this source and identifying the ions unambiguously with the MR-ToF, the following negative ion species [249] could be observed: boron, carbon, magnesium, aluminium, chromium, manganese, iron, cobalt, nickel, copper, silver, indium [250], tin [251], hafnium, tantalum, gold, lead [248] and bismuth [252].

7.3.3 The ISCOOL buncher

In order to comply with the PUMA requirements, the ISOLDE beam parameters need to be further optimized after the magnetic separation. In particular, they need to be bunched and purified, accordingly to the requirements of PUMA (see Table 14). The bunching will be performed by the existing ISCOOL cooler and buncher [235]. ISCOOL is a general purpose RFQ ion trap, located in the HRS beamline and constructed to improve the emittance of the incoming radioactive ion beams and to deliver them as bunches to the experiments. It is presented in Fig. 65.

The system consists of a linear Paul trap filled with a buffer gas in which the ions thermalize through collisions with the buffer gas while the oscillating quadrupole field of the trap rods provides radial confinement [253]. The buffer gas is chosen as a noble gas to minimise charge transfer to the radioactive ions. For an efficient cooling, the mass of the buffer gas atoms should be smaller than the mass of the nuclei to cool. Light ions have to be cooled with helium or even hydrogen as a buffer gas. Currently, ISCOOL is not able to use hydrogen as a buffer gas since specific safety considerations have to be taken into account which are envisaged in the future. In the case of PUMA, these light mass gasses causes a particular difficulty since it is difficult to remove them with vacuum pumps. The vacuum system will therefore be dimensioned and thought for helium, together with other gases. The gas volume of ISCOOL is isolated from the beam-line by two differential pumping sections which guarantee a vacuum better than 10^{-6} mbar both upstream and downstream. These vacuum conditions set the constraint for the dedicated differential pumping system for PUMA which aims at a reduction better than 10^5, from 10^{-6} to better than 10^{-11} mbar at the entrance of the PUMA cryostat.

ISCOOL provides the possibility to deliver bunches of a few microseconds length, reduced energy spread (~ 1 eV for slow extraction) and reduced transverse beam emittance (less
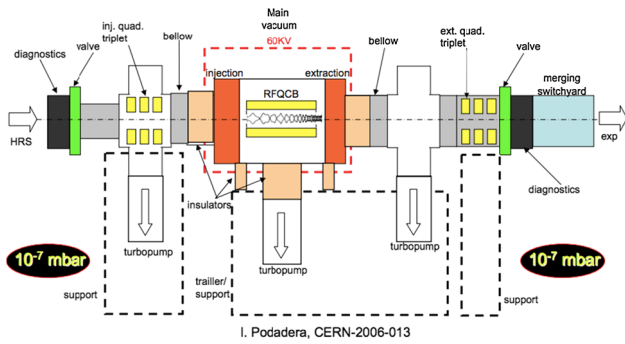
Fig. 65 Sketch of the ISCOOL buncher. A differential pumping maintains a vacuum better than 10^{-6} mbar upstream and downstream the buncher despite the gas flow in the RFQ. Figure from [254]
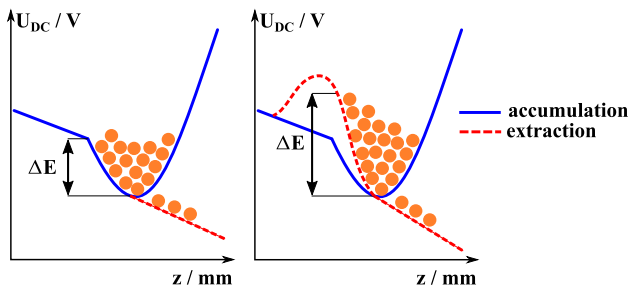

Fig. 66 Ion extraction procedures from an RFQ: slow extraction (left) and fast extraction, also called *push-pull* extraction (right). Figure adapted from [254]
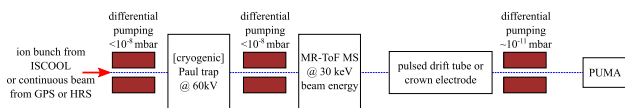

Fig. 67 Schematic layout for the PUMA beamline at ISOLDE. Focusing elements and pumping elements are not shown

than 3π mm mrad at 60 keV), which allows the experiments to have a better injection of the beam into the experimental setups [228,255] and to gate on the time structure of the beam to reduce unwanted background. The different ejection methods are schematically shown in Fig. 66.

7.3.4 Overview of the RCX10 beamline

A sketch of a possible beamline layout at ISOLDE for PUMA is shown in Fig. 67.

The first part of the RCX10 beamline will require compact electrostatic quadrupole triplets which could be based on the design of the doublets at ELENA. The beam line will then be composed of a Paul trap floated to 50 kV and a 30-keV multi-reflection time-of-flight mass separator (MR-ToF MS), both developed as part of the MIRACLS project. This MR-ToF system will produce 30-keV isotopic beams with proper emittances. At first the Paul trap will be at room temperature, while the development of a cryogenic Paul trap for a better

emittance is considered at a later stage. Vacuum pressure better than 10^{-9} mbar is targeted downstream the MR-ToF, while a vacuum better than $5 \cdot 10^{-8}$ mbar is guaranteed.

A $\theta = 10-30°$ electrostatic deflector will be added to turn the beam after the MIRACLS MR-ToF setup to the PUMA setup in the HIE ISOLDE experimental zone. An existing standard ISOLDE diagnostic box containing a Faraday cup and beam profile scanner will be located at the end of the RCX10 line before the MIRACLS setup.

7.3.5 The MR-ToF mass separator

A MR-ToF MS for ions at high energy (up to 30 keV) is under development at ISOLDE by the MIRACLS and the ISOLDE collaboration. A MR-ToF device is a component of typically one meter length which consist of a field free drift section surrounded by two electrostatic mirrors. Charged ions can be injected into and ejected from the MR-ToF MS by quickly switching the potential applied to the so called intrap lift [256] or parts of the mirror electrodes [257]. Once trapped between the mirrors of the MR-ToF MS, the ions are separated in time as a function of their mass.

The Multi Ion Reflection Apparatus for Collinear Laser Spectroscopy (MIRACLS) experiment is a new setup at ISOLDE aiming at enhancing the sensitivity of collinear laser spectroscopy (CLS) for short-lived radioactive nuclei by a factor 20–600 in order to probe rare isotopes out of reach with conventional techniques [258]. This is achieved by storing ion bunches of radionuclides in a MR-ToF device. While the ions are bouncing back and forth between the electrostatic mirrors, the ion bunch interacts with the spectroscopy laser during each revolution in MIRACLS, compared to only once in conventional CLS. This increased laser-ion interaction time results in an improved sensitivity. In order to maintain the high resolution of CLS, MIRACLS MR-ToF device will operate at an ion beam energy of 30 keV, compared to a few keV in state-of-the-art instruments. In order to meet the requirements of CLS (low energy spread) and MR-ToF operation (narrow temporal bunch width), MIRACLS will prepare the ion bunch in a Paul trap to obtain an improved ion-bunch emittance. The combination of improved emittance and increased ion beam energy in the MR-ToF device at MIRACLS are also very beneficial for fast and highly selective mass separation in a MR-ToF device. It is planned to develop the respective techniques within MIRACLS, serving as a prototype for a future general purpose 30 keV MR-ToF device at ISOLDE. An illustration of the functionality of a MR-ToF mass separator is shown in Fig. 68.

The mass separation capability of a MR-ToF MS, its emittance requirements and its bunched working condition fit very well with the demands of PUMA. In the concept of PUMA at ISOLDE, it is expected that MIRACLS' MR-ToF system will be located a few meters upstream of PUMA. It
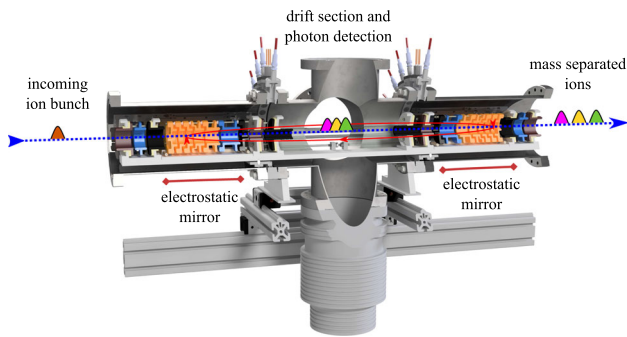
Fig. 68 Sketch of a MR-ToF device similar to the one in development for the MIRACLS experiment

Fig. 69 Segmented beamline for the transportation of purified ion beams from the MR-ToF to PUMA. Beams from the MR-ToF MS is entering from the left

will be possible to supply a beam with a high purity and a low energy as needed. In addition, the MR-ToF MS together with its dedicated coller buncher will also allow to tackle the more challenging isotopes in terms of required mass resolving power and initial beam emittance from the target ion source arrangement.

The development of the experiment is divided in three phases: the first one is the commissionning of the 30-keV MR-ToF MS as part of the MIRACLS project, the second one is the reconfiguration of the 30-keV MR-ToF MS at the RCX10 low-energy beam line, and the third one is the development and inclusion of a cryogenic Paul trap to adjust the traversal and longitudinal emittance of the beam entering the MR-ToF MS, leading to an improved turnaround-time of the ions and a lower energy spread. Designs and simulations of the full beam line are ongoing. It is expected that the MIRACLS system will be commissioned for laser spectroscopy with radioactive beams in 2022. The first purified beams are expected to be provided from late 2023 in line with the PUMA schedule.

The kinetic energy of the ions after MIRACLS is expected to reach 30 keV, which is too high for PUMA to trap them. For this reason, we are currently considering a dedicated pulse drift tube, following a similar design of the one developed for ELENA, which will allow us to slow the beam down to the desired energy of about 4 keV. As an alternative, we are also considering to lower the beam energy to few keV by using the in-trap lift technique [256] together with the mirror ejection technique [257], therefore without a pulsed-drift tube.

7.3.6 PUMA beam optics

The optics for the beamline will need to be designed according to the requirements for PUMA and to the specifications of ISCOOL (the RFQ cooler and buncher after the HRS ISOLDE separator, upstream from the MIRACLS and PUMA setup) as well as to the requirements of the MIRACLS system for beam purification situated after the ISCOOL and before the PUMA setup.
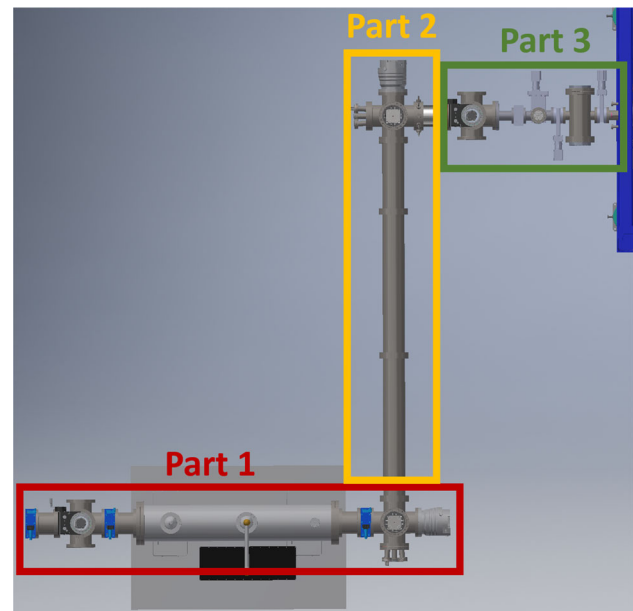
A first draft of a beamline connecting the MIRACLS MR-ToF mass separator and the PUMA frame has been simulated with the SIMION software. As indicated in Fig. 64, the beamline will include two 90° bends, allowing to transport the purified ion beam into the PUMA setup. For the ion optical simulations, this beamline is divided into three straight segments, as shown in Fig. 69. An overview over the ion optical elements within the segments is given in Fig. 70.

The general purpose of the beamline is to transport the purified ions as efficiently as possible into the PUMA trapping region. As a measure for this efficiency, the transmission of ions into the PUMA collision trap is considered. Similar to the case of the ELENA LNE51 beamline, a particle is transmitted if it did not get lost on a radial aperture (e.g. the conductance pipe in front of the collision trap) and is sufficiently decelerated by the two pulsed drift tubes. In comparison to the straight beamline at ELENA, an additional complexity of the ion optics arises from the electrostatic quadrupole benders, giving rise to a horizontal dispersion. To compensate for the induced dispersion, ELENA-type electrostatic quadrupole doublets are placed behind both benders, which compensate the growth of an incoming ion bunch in horizontal direction.

As an input into the ion optical simulations, a conservative set of input beam parameters assuming a transversal beam emittance of 1 mm mrad has been taken into account. These parameters are summarized in Table 16. In the discussed simulations, the ion mass and charge were considered to be those of $^{17}Ne^+$. A transmission of about 73% was reached. Even
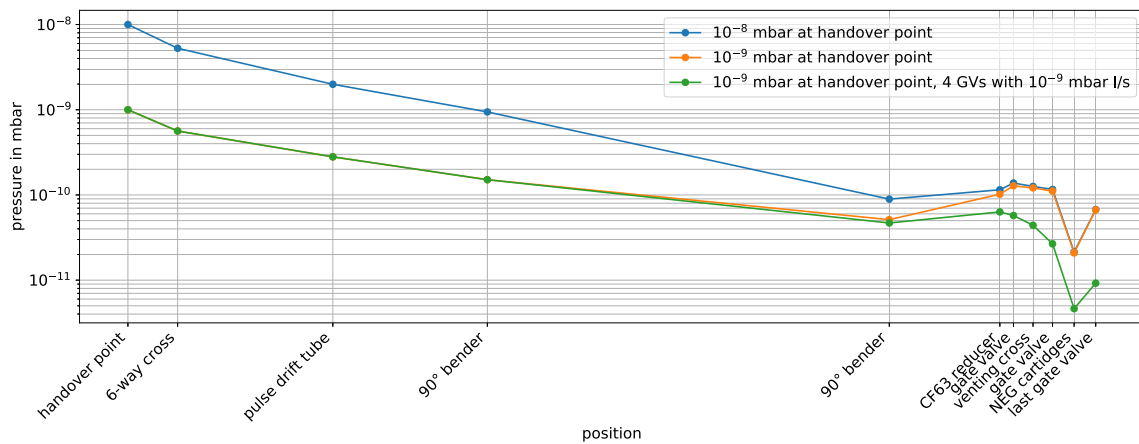
Fig. 71 Pressure along the PUMA-ISOLDE beamline at selected elements for different input pressures. The total length of the beamline is ~ 6.8 m
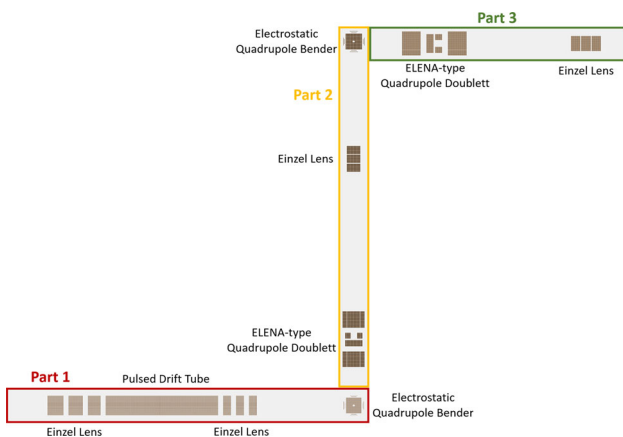

Fig. 70 Overview over the ion optical elements included into the three segments of the beamline between MIRACLS and PUMA

Table 16 Input beam properties for the transmission determination of purified ions

Property	Value
Transversal beam size (RMS)	1 mm
Transversal angular spread (RMS)	1 mrad
Input energy	50 keV
Energy spread (RMS)	100 eV
Bunch length (RMS)	50 ns

in case of a more pessimistic approach with a transversal beam size which is twice as high, the transmission is at about 50%. However, it is assumed that the future cryogenic Paul trap will provide significantly smaller emittances, leading to an overall higher ion transmission into the PUMA collision trap.

7.4 Vacuum

The vacuum conditions at ISOLDE set the constraint for the dedicated differential pumping system that will be necessary for PUMA. It aims at a reduction better than 10^3, from few 10^{-8} mbar (worst case scenario) to better than $5 \cdot 10^{-11}$ mbar at the entrance of PUMA (at the last 300-K gate valve of the PUMA experiment). A vacuum line between the MIRACLS MR-ToF and PUMA will be designed and installed. Additional sector valves between the MIRACLS and PUMA setup will be added for protection reasons and to enable connecting and disconnecting PUMA. The injection of any gas other than H_2 upstream PUMA, in particular He, has to be addressed and will have an impact on the vacuum system design. We present here first vacuum estimates based on the considered concept.

7.4.1 Hydrogen

The ISOLDE beam line will include two 90° bends to increase the length of the beam line and to remove neutral, non-gettable gases. An electrical network analysis (ENA) similar to the one done for ELENA (see Sect. 5.4.3) was done for the ISOLDE location. The reducer-cross with two NEG-pumps is attached to the frame and will be moved with it. The assumptions made for the calculations are as follows: (i) Only hydrogen is considered; (ii) Where possible, NEG coating is applied. This includes crosses, beam pipes, and the vacuum tube of the pulse drift tube (CF DN250). A pumping speed of 0.044 l/s/cm^2 (sticking factor $1 \cdot 10^{-3}$) is assumed; (iii) The other surfaces of the beam pipe are stainless steel and have an outgassing rate of $5 \cdot 10^{-12}$ mbar l/s/cm^2; (iv) All other components have an outgassing rate of $1 \cdot 10^{-8}$ mbar l/s, except the pulse drift tube ($1 \cdot 10^{-7}$ mbar l/s) and the extractor gauges ($1 \cdot 10^{-9}$ mbar l/s [232]); (v) The conductance of pipes and crosses can be calculated as cylinders; (vi) 2 NEG
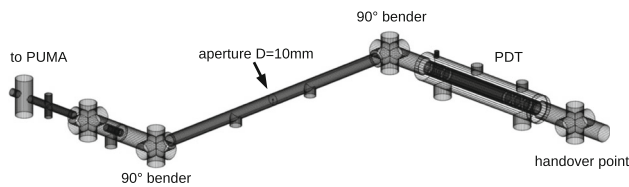
Fig. 72 MOLFLOW model of the ISOLDE beamline for helium transmission calculations

pumps with a pumping speed of 1000 l/s for H_2 each; (vii) 5 ion pumps with a pumping speed of 240 l/s for H_2 each; (viii) 3 turbo pumps with a pumping speed of 555 l/s for H_2 each.

The ENA performed with LTspiceXVII (see Sect. 5.4.3) shows that the two NEG pumps can reduce the pressure at the last gate valve to the order of $7 \cdot 10^{-11}$ mbar. The pressure at the hand-over point was assumed to be $1 \cdot 10^{-8}$ mbar, but even a reduction to $1 \cdot 10^{-9}$ mbar virtually does not change the pressure at the last gate valve as it is dominated by outgassing along the beam line (see Fig. 71).

The largest influence on the pressure at the last gate valve comes from the outgassing of the valve itself. This was conservatively estimated to be $1 \cdot 10^{-8}$ mbar l/s. However, the outgassing can be reduced drastically [233], for example by repetitive baking. If the outgassing of the last two valves can be reduced to $1 \cdot 10^{-9}$ mbar l/s, the electrical network analysis gives a vacuum pressure of $1.6 \cdot 10^{-11}$ mbar. If the outgassing of all four CF63 gate valves can be reduced, the pressure drops to $1 \cdot 10^{-11}$ mbar.

7.4.2 Helium

Since the ion optical layout of the ISOLDE beam line is not fixed yet, the beam pipe diameters and conductances cannot be optimised. Nevertheless we give a first estimate of the transmission of helium atoms from the handover point to the last gate valve, calculated with MOLFLOW.

The assumptions made for the calculations are as follows: (i) No outgassing of helium; (ii) 3 turbo pumps with a pumping speed of 820 l/s for He each; (iii) 5 ion pumps with a pumping speed of 24 l/s for He each (10% of nominal pumping speed); (iv) Same pulsed drift tube as at ELENA, this shall still be optimised; (v) An iris shutter at the focal point of the mid-section einzel lens (see Fig. 72).

The dimensions of the beam elements are chosen to be the same the same as for ELENA since the ISOLDE beam line is not finalized yet. Only the middle 2.5 m stretch is reduced to CF100. Since the ion optics of the RCX10 beamline is still under development, the ion optical elements were not implemented in these simulations.

With an aperture of the iris shutter of $D = 10$ mm, the transmission probability is $2 \cdot 10^{-4}$. Even though the saturation of the surface for helium will be quicker than for hydrogen [259], the setup allows for enough freedom to reduce the

transmission further, for example, with the aperture of the pulsed drift tube, depending on the emittance from MIRA-CLS.

8 Conclusion

The PUMA, antiProton Unstable Matter Annihilation, experiment aims at investigating rare isotopes with low-energy antiprotons as a probe. The experiment is based on the detection of pions resulting from the annihilation of an antiproton with the nucleus. These pions come from the decay of an in-trap formed antiprotonic atom, following the historical work of Bugg et al. [3] and the later idea of Yamazaki and Wada [260]. The experiment will give access to the number of proton-to-neutron annihilation ratio in the tail of the nuclear density at an accuracy better than 10%.

PUMA aims at transporting one billion antiprotons from the ELENA facility, where antiprotons from the Antiproton Decelerator (AD) are cooled down to 100 keV, to the rare-isotope beam facility ISOLDE. An extreme vacuum in a Penning trap, achieved via cryopumping and a low-conductance cryostat design, will allow to store antiprotons with a half-life better than one month, enabling experiments at ISOLDE. A low residual gas density of $20 \ \text{cm}^{-3}$ in the reaction zone will limit the background and enable the PUMA physics case.

The PUMA experiment at CERN is unique, and made possible by the combination of the world-leading facilities ELENA, for the low-energy antiproton production, and ISOLDE, for the radioactive isotope production. Physics experiments with rare-isotopes and antiprotons as proposed with PUMA will need to face three main challenges: the required extreme vacuum to store the antiprotons long enough, the transport of antimatter with acceptable or compensable excitation of the antiproton plasma and the efficient in-trap mixing of ions and antiprotons with relative energies of few tens of eV.

The development of the experiment has already started. The installation of the antiproton beam line is expected to be finalized in 2022. The first benchmark experiments are expected to take place in 2023, first at ELENA with stable ions, then with rare isotopes at ISOLDE.

In addition to probing the so-far unexplored isospin composition of the nuclear-radial-density tail of radioactive nuclei, PUMA has the potential to explore other nuclear-physics topics, such as nuclear correlations at low density or hypernuclei, bound nuclear system that contain one or several hyperons, a baryon with a strange quark. The later should provide unique information on the in-medium hyperon-nucleon interactions. PUMA will also contribute to the democratisation of antiprotons for research, by allowing the delivery of a sizeable amount of antiprotons to other laboratories.

Author contributions AO designed the experiment. NN, AO, AS, FW designed the trap. DN, YK, FW designed and installed the control of the trap electrodes. JF, NN, FW designed and built the electron gun. JF, NN, FW defined the plasma diagnostics. PC, JFS, EF, AS designed the cryostat and performed the vacuum simulations. AF performed the thermal calculations for the cryostat and trap. ECP, RDO, SZ designed the TPC. SZ performed the electronic field simulations and designed the TPC field cage. SZ developed the Monte-Carlo simulations for PUMA. DC developed the electronics for the TPC. DR, SZ designed the plastic-scintillator barrels. HDG, NM, WM computed a pre-design of the PUMA solenoid. AH managed the solenoid and frame design and construction at Bilfinger-Noell. JF, AS performed the acceptance magnetic-field measurements. OBF, AS performed the first non-neutron plasma simulations for PUMA. YK, YO developed the formalism and the analysis method based on the neural network to correct the observables from final-state interactions in a model-independent way. SME and MV conceived and designed the MIRACLS setup and, together with SS, contributed in the definition of the low-energy RI beam line for PUMA. CK, SME, MS, LS, MV, FW designed and built the low-energy ion source beam line and the associated Paul trap and MRTOF for ELENA. JF and HFS performed the vacuum calculations for the ELENA and ISOLDE beam lines. FB managed the integration of PUMA at ELENA and the preparation of the LNE51 area. MF, AS performed the beam optics calculations for the LNE51 beam line and preliminary calculations for ISOLDE. JFS, JF, KJ, SME, GN, AO, AS, ES, MV, FW designed the preliminary ISOLDE beam line. JF and AH designed the 100-kV pulsed drift tube. TA, GH, YK, RL, NN, AO, NP, TU, MW, FW contributed to the physics case of PUMA. CK, MGR, RS, SZ clarified the physics of the atomic cascade relevant for PUMA and developed its computer code. YK, YO developed the formalism to correct the measured total pion charge from final-state interactions. All authors have read and commented the manuscript.

Data Availability Statement This manuscript has no associated data or the data will not be deposited. [Authors' comment: The experiment is in its preparation phase, therefore not data have been taken yet.]

PUMA collaboration PUMA collaboration as per ms PUMA collaboration At the publication date of the present article, the PUMA collaboration is composed of seven collaboration institutions: [1]CERN, [2]IJClab (IN2P3), [3]IPHC (IN2P3), [4]Laboratoire Kastler Brossel, [5]Technische Universität Darmstadt, IKP, [6]Technische Universität Darmstadt, TEMF, [7]TRIUMF. The collaboration is composed of the following members from these institutions: T. Aumann[5], N. Azaryan[1], O. Boine-Frankenheim[6], U. Bonnes[5], F. Butin[1], P. Chiggiato[1], H. De Gersem[6], R. De Oliveira[1], P.-Y. Duerinck[3], J. Ferreira Somoza[1], J. Fischer[5], G. Hupin[2], P. Indelicato[4], B. Jenniger[1], K. Johnston[1], C. Klink[5], M. Kowalska[1], Y. Kubota[5], R. Lazauskas[3], S. Malbrunot-Ettenauer[7], N. Marsic[6], W. F. O. Müller[6], U. Niedermayer[6], A. Obertelli[5], N. Paul[4], L. Riik[6], R. Rinaldesi[1], D. Rossi[5], M. Schlaich[5], A. Schmidt[5], E. Siesling[1], A. Stoeltzel[1], M. Vilen[1], F. Wienholtz[5], C. Xanthopoulou[5], S. Zacarias[5].

References

1. I. Tanihata, H. Hamagaki, O. Hashimoto, Y. Shida, N. Yoshikawa, K. Sugimoto, O. Yamakawa, T. Kobayashi, N. Takahashi, Measurements of interaction cross sections and nuclear radii in the light *p*-shell region. Phys. Rev. Lett. **55**, 2676–2679 (1985)
2. J.A. Nolen, J.P. Schiffer, Coulomb energies. Annu. Rev. Nucl. Sci. **19**(1), 471–526 (1969)
3. W.M. Bugg, G.T. Condo, E.L. Hart, H.O. Cohn, R.D. McCulloch, Evidence for a neutron halo in heavy nuclei from antiproton absorption. Phys. Rev. Lett. **31**, 475–478 (1973)
4. M. Freer, H. Horiuchi, Y. Kanada-En'yo, D. Lee, U.-G. Meißner, Microscopic clustering in light nuclei. Rev. Mod. Phys. **90**, 035004 (2018)
5. P.G. Hansen, B. Jonson, The neutron halo of extremely neutron-rich nuclei. EPL Europhys. Lett. **4**, 409 (1987)
6. P.G. Hansen, A.S. Jensen, B. Jonson, Nuclear halos. Annu. Rev. Nucl. Part. Sci. **45**(1), 591–634 (1995)
7. A.S. Jensen, K. Riisager, D.V. Fedorov, E. Garrido, Structure and reactions of quantum halos. Rev. Mod. Phys. **76**, 215–261 (2004)
8. K. Riisager, Halos and related structures. Phys. Scr. **T152**, 014001 (2013)
9. Y. Kubota, A. Corsi, G. Authelet, H. Baba, C. Caesar, D. Calvet, A. Delbart, M. Dozono, J. Feng, F. Flavigny, J.-M. Gheller, J. Gibelin, A. Giganon, A. Gillibert, K. Hasegawa, T. Isobe, Y. Kanaya, S. Kawakami, D. Kim, Y. Kikuchi, Y. Kiyokawa, M. Kobayashi, N. Kobayashi, T. Kobayashi, Y. Kondo, Z. Korkulu, S. Koyama, V. Lapoux, Y. Maeda, F.M. Marqués, T. Motobayashi, T. Miyazaki, T. Nakamura, N. Nakatsuka, Y. Nishio, A. Obertelli, K. Ogata, A. Ohkura, N.A. Orr, S. Ota, H. Otsu, T. Ozaki, V. Panin, S. Paschalis, E.C. Pollacco, S. Reichert, J.-Y. Roussé, A.T. Saito, S. Sakaguchi, M. Sako, C. Santamaria, M. Sasano, H. Sato, M. Shikata, Y. Shimizu, Y. Shindo, L. Stuhl, T. Sumikama, Y.L. Sun, M. Tabata, Y. Togano, J. Tsubota, Z.H. Yang, J. Yasuda, K. Yoneda, J. Zenihiro, T. Uesaka, Surface localization of the dineutron in ^{11}Li. Phys. Rev. Lett. **125**, 252501 (2020)
10. C. Bertulani, H.-W. Hammer, U. van Kolck, Effective field theory for halo nuclei: shallow p-wave states. Nucl. Phys. A **712**(1), 37–58 (2002)
11. T. Frederico, A. Delfino, L. Tomio, M. Yamashita, Universal aspects of light halo nuclei. Prog. Part. Nucl. Phys. **67**(4), 939–994 (2012)
12. B. Jonson, Light dripline nuclei. Phys. Rep. **389**(1), 1–59 (2004)
13. I. Tanihata, H. Savajols, R. Kanungo, Recent experimental progress in nuclear halo structure studies. Prog. Part. Nucl. Phys. **68**, 215–313 (2013)
14. T. Nakamura, N. Kobayashi, Y. Kondo, Y. Satou, J.A. Tostevin, Y. Utsuno, N. Aoi, H. Baba, N. Fukuda, J. Gibelin, N. Inabe, M. Ishihara, D. Kameda, T. Kubo, T. Motobayashi, T. Ohnishi, N.A. Orr, H. Otsu, T. Otsuka, H. Sakurai, T. Sumikama, H. Takeda, E. Takeshita, M. Takechi, S. Takeuchi, Y. Togano, K. Yoneda,

Deformation-driven *p*-wave halos at the drip line: ^{31}Ne. Phys. Rev. Lett. **112**, 142501 (2014)

15. N. Kobayashi, T. Nakamura, Y. Kondo, J.A. Tostevin, Y. Utsuno, N. Aoi, H. Baba, R. Barthelemy, M.A. Famiano, N. Fukuda, N. Inabe, M. Ishihara, R. Kanungo, S. Kim, T. Kubo, G.S. Lee, H.S. Lee, M. Matsushita, T. Motobayashi, T. Ohnishi, N.A. Orr, H. Otsu, T. Otsuka, T. Sako, H. Sakurai, Y. Satou, T. Sumikama, H. Takeda, S. Takeuchi, R. Tanaka, Y. Togano, K. Yoneda, Observation of a *p*-wave one-neutron halo configuration in ^{37}Mg. Phys. Rev. Lett. **112**, 242501 (2014)

16. Z.H. Yang, Y. Kubota, A. Corsi, K. Yoshida, X.-X. Sun, J.G. Li, M. Kimura, N. Michel, K. Ogata, C.X. Yuan, Q. Yuan, G. Authelet, H. Baba, C. Caesar, D. Calvet, A. Delbart, M. Dozono, J. Feng, F. Flavigny, J.-M. Gheller, J. Gibelin, A. Giganon, A. Gillibert, K. Hasegawa, T. Isobe, Y. Kanaya, S. Kawakami, D. Kim, Y. Kiyokawa, M. Kobayashi, N. Kobayashi, T. Kobayashi, Y. Kondo, Z. Korkulu, S. Koyama, V. Lapoux, Y. Maeda, F.M. Marqués, T. Motobayashi, T. Miyazaki, T. Nakamura, N. Nakatsuka, Y. Nishio, A. Obertelli, A. Ohkura, N.A. Orr, S. Ota, H. Otsu, T. Ozaki, V. Panin, S. Paschalis, E.C. Pollacco, S. Reichert, J.-Y. Roussé, A.T. Saito, S. Sakaguchi, M. Sako, C. Santamaria, M. Sasano, H. Sato, M. Shikata, Y. Shimizu, Y. Shindo, L. Stuhl, T. Sumikama, Y.L. Sun, M. Tabata, Y. Togano, J. Tsubota, F.R. Xu, J. Yasuda, K. Yoneda, J. Zenihiro, S.-G. Zhou, W. Zuo, T. Uesaka, Quasifree neutron knockout reaction reveals a small *s*-orbital component in the borromean nucleus ^{17}B. Phys. Rev. Lett. **126**, 082501 (2021)

17. I. Tanihata, T. Kobayashi, O. Yamakawa, S. Shimoura, K. Ekuni, K. Sugimoto, N. Takahashi, T. Shimoda, H. Sato, Measurement of interaction cross sections using isotope beams of Be and B and isospin dependence of the nuclear radii. Phys. Lett. B **206**(4), 592–596 (1988)

18. T. Minamisono, T. Ohtsubo, I. Minami, S. Fukuda, A. Kitagawa, M. Fukuda, K. Matsuta, Y. Nojiri, S. Takeda, H. Sagawa, H. Kitagawa, Proton halo of ^{8}B disclosed by its giant quadrupole moment. Phys. Rev. Lett. **69**, 2058–2061 (1992)

19. G. Korolev, A. Dobrovolsky, A. Inglessi, G. Alkhazov, P. Egelhof, A. Estradé, I. Dillmann, F. Farinon, H. Geissel, S. Ilieva, Y. Ke, A. Khanzadeev, O. Kiselev, J. Kurcewicz, X. Le, Y. Litvinov, G. Petrov, A. Prochazka, C. Scheidenberger, L. Sergeev, H. Simon, M. Takechi, S. Tang, V. Volkov, A. Vorobyov, H. Weick, V. Yatsoura, Halo structure of ^{8}B determined from intermediate energy proton elastic scattering in inverse kinematics. Phys. Lett. B **780**, 200–204 (2018)

20. W. Geithner, T. Neff, G. Audi, K. Blaum, P. Delahaye, H. Feldmeier, S. George, C. Guénaut, F. Herfurth, A. Herlert, S. Kappertz, M. Keim, A. Kellerbauer, H.-J. Kluge, M. Kowalska, P. Lievens, D. Lunney, K. Marinova, R. Neugart, L. Schweikhard, S. Wilbert, C. Yazidjian, Masses and charge radii of $^{17-22}$Ne and the two-proton-halo candidate ^{17}Ne. Phys. Rev. Lett. **101**, 252502 (2008)

21. C. Lehr, F. Wamers, F. Aksouh, Yu. Aksyutina, H. Álvarez-Pol, L. Atar, T. Aumann, S. Beceiro-Novo, C.A. Bertulani, K. Boretzky, M.J.G. Borge, C. Caesar, M. Chartier, A. Chatillon, L.V. Chulkov, D. Cortina-Gil, P. Díaz Fernández, H. Emling, O. Ershova, L.M. Fraile, H.O.U. Fynbo, D. Galaviz, H. Geissel, M. Heil, M. Heine, D.H.H. Hoffmann, M. Holl, H.T. Johansson, B. Jonson, C. Karagiannis, O.A. Kiselev, J.V. Kratz, R. Kulessa, N. Kurz, C. Langer, M. Lantz, T. Le Bleis, R. Lemmon, Yu.A. Litvinov, B. Löher, K. Mahata, J. Marganiec-Galazka, C. Müntz, T. Nilsson, C. Nociforo, W. Ott, V. Panin, S. Paschalis, A. Perea, R. Plag, R. Reifarth, A. Richter, K. Riisager, C. Rodriguez-Tajes, D. Rossi, H. Scheit, G. Schrieder, P. Schrock, H. Simon, J. Stroth, K. Sümmerer, O. Tengblad, H. Weick, C. Wimmer, Unveiling the two-proton halo character of ^{17}Ne: Exclusive measurement of quasi-free proton-knockout reactions. Phys. Lett. B. **827**, 136957 (2022). https://doi.org/10.1016/j.physletb. 2022.136957, https://www.sciencedirect.com/science/article/pii/S0370269322000910

22. V. Rotival, K. Bennaceur, T. Duguet, Halo phenomenon in finite many-fermion systems: atom-positron complexes and large-scale study of atomic nuclei. Phys. Rev. C **79**, 054309 (2009)

23. S. Mizutori, J. Dobaczewski, G.A. Lalazissis, W. Nazarewicz, P.-G. Reinhard, Nuclear skins and halos in the mean-field theory. Phys. Rev. C **61**, 044326 (2000)

24. M. Grasso, S. Yoshida, N. Sandulescu, N. Van Giai, Giant neutron halos in the non-relativistic mean field approach. Phys. Rev. C **74**, 064317 (2006)

25. J. Terasaki, S.Q. Zhang, S.G. Zhou, J. Meng, Giant halos in relativistic and nonrelativistic approaches. Phys. Rev. C **74**, 054318 (2006)

26. V. Rotival, T. Duguet, New analysis method of the halo phenomenon in finite many-fermion systems: first applications to medium-mass atomic nuclei. Phys. Rev. C **79**, 054308 (2009)

27. E. Chabanat, P. Bonche, P. Haensel, J. Meyer, R. Schaeffer, A skyrme parametrization from subnuclear to neutron star densities part ii nuclei far from stabilities. Nucl. Phys. A **635**(1), 231–256 (1998)

28. I. Hamamoto, Dominance of low-ℓ component in weakly bound deformed single-neutron orbits. Phys. Rev. C **69**, 041306 (2004)

29. I. Hamamoto, Nilsson diagrams for light neutron-rich nuclei with weakly-bound neutrons. Phys. Rev. C **76**, 054319 (2007)

30. I. Hamamoto, Interpretation of coulomb breakup of ^{31}Ne in terms of deformation. Phys. Rev. C **81**, 021304 (2010)

31. M. Dutra, O. Lourenço, J.S. Sá Martins, A. Delfino, J.R. Stone, P.D. Stevenson, Skyrme interaction and nuclear matter constraints. Phys. Rev. C **85**, 035201 (2012)

32. M. Bender, P.-H. Heenen, P.-G. Reinhard, Self-consistent mean-field models for nuclear structure. Rev. Mod. Phys. **75**, 121–180 (2003)

33. J. Stone, P.-G. Reinhard, The skyrme interaction in finite nuclei and nuclear matter. Prog. Part. Nucl. Phys. **58**(2), 587–657 (2007)

34. R. Sellahewa, A. Rios, Isovector properties of the gogny interaction. Phys. Rev. C **90**, 054327 (2014)

35. X. Roca-Maza, X. Centelles, X. Viñas, M. Warda, Neutron skin of ^{208}Pb, nuclear symmetry energy, and the parity radius experiment. Phys. Rev. Lett. **106**, 252501 (2011)

36. X. Roca-Maza, X. Viñas, M. Centelles, B.K. Agrawal, G. Colò, N. Paar, J. Piekarewicz, D. Vretenar, Neutron skin thickness from the measured electric dipole polarizability in ^{68}Ni, ^{120}Sn, and ^{208}Pb. Phys. Rev. C **92**, 064304 (2015)

37. F.J. Fattoyev, J. Piekarewicz, C.J. Horowitz, Neutron skins and neutron stars in the multimessenger era. Phys. Rev. Lett. **120**, 172702 (2018)

38. C.A. Bertulani, J. Valencia, Neutron skins as laboratory constraints on properties of neutron stars and on what we can learn from heavy ion fragmentation reactions. Phys. Rev. C **100**, 015802 (2019)

39. W. Horiuchi, S. Ebata, K. Iida, Neutron-skin thickness determines the surface tension of a compressible nuclear droplet. Phys. Rev. C **96**, 035804 (2017)

40. S. Abrahamyan, Z. Ahmed, H. Albataineh, K. Aniol, D. S. Armstrong, W. Armstrong, T. Averett, B. Babineau, A. Barbieri, V. Bellini, R. Beminiwattha, J. Benesch, F. Benmokhtar, T. Bielarski, W. Boeglin, A. Camsonne, M. Canan, P. Carter, G. D. Cates, C. Chen, J.-P. Chen, O. Hen, F. Cusanno, M. M. Dalton, R. De Leo, K. de Jager, W. Deconinck, P. Decowski, X. Deng, A. Deur, D. Dutta, A. Etile, D. Flay, G. B. Franklin, M. Friend, S. Frullani, E. Fuchey, F. Garibaldi, E. Gasser, R. Gilman, A. Giusa, A. Glamazdin, J. Gomez, J. Grames, C. Gu, O. Hansen, J. Hansknecht, D. W. Higinbotham, R. S. Holmes, T. Holmstrom, C. J. Horowitz, J. Hoskins, J. Huang, C. E. Hyde, F. Itard, C.-M. Jen, E. Jensen, G. Jin, S. Johnston, A. Kelleher, K. Kliakhandler,

P. M. King, S. Kowalski, K. S. Kumar, J. Leacock, J. Leckey, J. H. Lee, J. J. LeRose, R. Lindgren, N. Liyanage, N. Lubinsky, J. Mammei, F. Mammoliti, D. J. Margaziotis, P. Markowitz, A. McCreary, D. McNulty, L. Mercado, Z.-E. Meziani, R. W. Michaels, M. Mihovilovic, N. Muangma, C. Muñoz Camacho, S. Nanda, V. Nelyubin, N. Nuruzzaman, Y. Oh, A. Palmer, D. Parno, K. D. Paschke, S. K. Phillips, B. Poelker, R. Pomatsalyuk, M. Posik, A. J. R. Puckett, B. Quinn, A. Rakhman, P. E. Reimer, S. Riordan, P. Rogan, G. Ron, G. Russo, K. Saenboonruang, A. Saha, B. Sawatzky, A. Shahinyan, R. Silwal, S. Sirca, K. Slifer, P. Solvignon, P. A. Souder, M. L. Sperduto, R. Subedi, R. Suleiman, V. Sulkosky, C. M. Sutera, W. A. Tobias, W. Troth, G. M. Urciuoli, B. Waidyawansa, D. Wang, J. Wexler, R. Wilson, B. Wojtsekhowski, X. Yan, H. Yao, Y. Ye, Z. Ye, V. Yim, L. Zana, X. Zhan, J. Zhang, Y. Zhang, X. Zheng, P. Zhu, Measurement of the neutron radius of ^{208}Pb through parity violation in electron scattering. Phys. Rev. Lett. **108**, 112502 (2012)

41. C.J. Horowitz, J. Piekarewicz, Neutron star structure and the neutron radius of ^{208}Pb. Phys. Rev. Lett. **86**, 5647–5650 (2001)

42. K. Hebeler, J.M. Lattimer, C.J. Pethick, A. Schwenk, Equation of state and neutron star properties constrained by nuclear physics and observation. Astrophys. J. **773**, 11 (2013)

43. D. Adhikari, H. Albataineh, D. Androic, K. Aniol, D. S. Armstrong, T. Averett, C. Ayerbe Gayoso, S. Barcus, V. Bellini, R. S. Beminiwattha, J. F. Benesch, H. Bhatt, D. Bhatta Pathak, D. Bhetuwal, B. Blaikie, Q. Campagna, A. Camsonne, G. D. Cates, Y. Chen, C. Clarke, J. C. Cornejo, S. Covrig Dusa, P. Datta, A. Deshpande, D. Dutta, C. Feldman, E. Fuchey, C. Gal, D. Gaskell, T. Gautam, M. Gericke, C. Ghosh, I. Halilovic, J.-O. Hansen, F. Hauenstein, W. Henry, C. J. Horowitz, C. Jantzi, S. Jian, S. Johnston, D. C. Jones, B. Karki, S. Katugampola, C. Keppel, P. M. King, D. E. King, M. Knauss, K. S. Kumar, T. Kutz, N. Lashley-Colthirst, G. Leverick, H. Liu, N. Liyange, S. Malace, R. Mammei, J. Mammei, M. McCaughan, D. McNulty, D. Meekins, C. Metts, R. Michaels, M. M. Mondal, J. Napolitano, A. Narayan, D. Nikolaev, M. N. H. Rashad, V. Owen, C. Palatchi, J. Pan, B. Pandey, S. Park, K. D. Paschke, M. Petrusky, M. L. Pitt, S. Premathilake, A. J. R. Puckett, B. Quinn, R. Radloff, S. Rahman, A. Rathnayake, B. T. Reed, P. E. Reimer, R. Richards, S. Riordan, Y. Roblin, S. Seeds, A. Shahinyan, P. Souder, L. Tang, M. Thiel, Y. Tian, G. M. Urciuoli, E. W. Wertz, B. Wojtsekhowski, B. Yale, T. Ye, A. Yoon, A. Zec, W. Zhang, J. Zhang, X. Zheng, Accurate determination of the neutron skin thickness of ^{208}Pb through parity-violation in electron scattering. Phys. Rev. Lett. **126**, 172502 (2021)

44. B.T. Reed, F.J. Fattoyev, C.J. Horowitz, J. Piekarewicz, Implications of PREX-2 on the equation of state of neutron-rich matter. Phys. Rev. Lett. **126**, 172503 (2021)

45. M. Cadeddu, C. Giunti, Y.F. Li, Y.Y. Zhang, Average CsI neutron density distribution from coherent data. Phys. Rev. Lett. **120**, 072501 (2018)

46. P. Coloma, I. Esteban, M.C. Gonzalez-Garcia, J. Menéndez, Determining the nuclear neutron distribution from coherent elastic neutrino-nucleus scattering: current results and future prospects. J. High Energy Phys. **2020**(8), 30 (2020)

47. M.H. Mahzoon, M.C. Atkinson, R.J. Charity, W.H. Dickhoff, Neutron skin thickness of ^{48}Ca from a nonlocal dispersive optical-model analysis. Phys. Rev. Lett. **119**, 222503 (2017)

48. C.M. Tarbert, D.P. Watts, D.I. Glazier, P. Aguar, J. Ahrens, J.R.M. Annand, H.J. Arends, R. Beck, V. Bekrenev, B. Boillat, A. Braghieri, D. Branford, W.J. Briscoe, J. Brudvik, S. Cherepnya, R. Codling, E.J. Downie, K. Foehl, P. Grabmayr, R. Gregor, E. Heid, D. Hornidge, O. Jahn, V.L. Kashevarov, A. Knezevic, R. Kondratiev, M. Korolija, M. Kotulla, D. Krambrich, B. Krusche, M. Lang, V. Lisin, K. Livingston, S. Lugert, I.J.D. MacGregor, D.M. Manley, M. Martinez, J.C. McGeorge, D. Mekterovic, V.

Metag, B.M.K. Nefkens, A. Nikolaev, R. Novotny, R.O. Owens, P. Pedroni, A. Polonski, S.N. Prakhov, J.W. Price, G. Rosner, M. Rost, T. Rostomyan, S. Schadmand, S. Schumann, D. Sober, A. Starostin, I. Supek, A. Thomas, M. Unverzagt, T. Walcher, L. Zana, F. Zehr, Neutron skin of ^{208}Pb from coherent pion photoproduction. Phys. Rev. Lett. **112**, 242502 (2014)

49. A. Tamii, I. Poltoratska, P. von Neumann-Cosel, Y. Fujita, T. Adachi, C.A. Bertulani, J. Carter, M. Dozono, H. Fujita, K. Fujita, K. Hatanaka, D. Ishikawa, M. Itoh, T. Kawabata, Y. Kalmykov, A.M. Krumbholz, E. Litvinova, H. Matsubara, K. Nakanishi, R. Neveling, H. Okamura, H.J. Ong, B. Özel-Tashenov, V.Y. Ponomarev, A. Richter, B. Rubio, H. Sakaguchi, Y. Sakemi, Y. Sasamoto, Y. Shimbara, Y. Shimizu, F.D. Smit, T. Suzuki, Y. Tameshige, J. Wambach, R. Yamada, M. Yosoi, J. Zenihiro, Complete electric dipole response and the neutron skin in ^{208}Pb. Phys. Rev. Lett. **107**, 062502 (2011)

50. S. Typel, Neutron skin thickness of heavy nuclei with $\alpha-particle$ correlations and the slope of the nuclear symmetry energy. Phys. Rev. C **89**, 064321 (2014)

51. S. Typel, H.H. Wolter, G. Röpke, D. Blaschke, Effects of the liquid-gas phase transition and cluster formation on the symmetry energy. Eur. Phys. J. A **50**, 17 (2014)

52. H. Hergert, A guided tour of ab initio nuclear many-body theory. Front. Phys. **8**, 379 (2020)

53. G. Hagen, A. Ekström, C. Forssén, G. R. Jansen, W. Nazarewicz, T. Papenbrock, K. A. Wendt, S. Bacca, N. Barnea, B. Carlsson, C. Drischler, K. Hebeler, M. Hjorth-Jensen, M. Miorelli, G. Orlandini, A. Schwenk, J. Simonis, Neutron and weak-charge distributions of the ^{48}Ca nucleus. Nature Phys. **12**, 186 EP (2015)

54. T. Aumann, W. Bartmann, A. Bouvard, O. Boine-Frankenheim, A. Broche, F. Butin, D. Calvet, J. Carbonell, P. Chiggiato, H. De Gersem, R. De Oliveira, T. Dobers, F. Ehm, J. Ferreira Somoza, J. Fischer, M. Fraser, E. Friedrich, M. Gomez-Ramos, J.-L. Grenard, G. Hupin, P. Indelicato, K. Johnston, Y. Kubota, R. Lazauskas, S. Malbrunot-Ettenauer, N. Marsic, W. F. O. Müller, S. Naimi, N. Nakatsuka, R. Necca, G. Neyens, A. Obertelli, Y. Ono, S. Pasinelli, N. Paul, P. Pérez, E. C. Pollacco, D. Rossi, H. Scheit, , R. Seki, A. Schmidt, L. Schweikhard, S. Sels, E. Siesling, T. Uesaka, M. Wada, F. Wienholtz, S. Wycech, S. Zacarias, PUMA : antiprotons and radioactive nuclei. Proposal SPSC-P-361, CERN (2019)

55. M. Wada, Y. Yamazaki, Technical developments toward antiprotonic atoms for nuclear structure studies of radioactive nuclei. Nucl. Instr. Methods Phys. Res. Sect. B Beam Interact. Mater. Atoms **214**, 196–200 (2004). Low Energy Antiproton Physics (LEAP'03)

56. J. Eades, F.J. Hartmann, Forty years of antiprotons. Rev. Mod. Phys. **71**, 373–419 (1999)

57. S. Wycech, J. Skalski, R. Smolańczuk, J. Dobaczewski, J.R. Rook, Antiprotonic studies of nuclear neutron halos. Phys. Rev. C **54**, 1832–1842 (1996)

58. R. Schmidt, F.J. Hartmann, B. Ketzer, T. von Egidy, T. Czosnyka, J. Jastrzębski, M. Kisieliński, P. Lubiński, P. Napiorkowski, L. Pieńkowski, A. Trzcińska, B. Kłos, R. Smolańczuk, S. Wycech, W. Pöschl, K. Gulda, W. Kurcewicz, E. Widmann, Composition of the nuclear periphery from antiproton absorption using short-lived residual nuclei. Phys. Rev. C **60**, 054309 (1999)

59. B. Kłos, A. Trzcińska, J. Jastrzkebski, T. Czosnyka, M. Kisieliński, P. Lubiński, P. Napiorkowski, L. Pieńkowski, F. J. Hartmann, B. Ketzer, P. Ring, R. Schmidt, T. v. Egidy, R. Smolańczuk, S. Wycech, K. Gulda, W. Kurcewicz, E. Widmann, B. A. Brown, Neutron density distributions from antiprotonic ^{208}Pb and ^{209}Bi atoms. Phys. Rev. C, **76**, 014311 (2007)

60. P. Lubiński, J. Jastrzębski, A. Trzcińska, W. Kurcewicz, F.J. Hartmann, W. Schmid, T. von Egidy, R. Smolańczuk, S. Wycech,

Composition of the nuclear periphery from antiproton absorption. Phys. Rev. C **57**, 2962–2973 (1998)

61. A. Trzcińska, J. Jastrzębski, P. Lubiński, F.J. Hartmann, R. Schmidt, T. von Egidy, B. Kłos, Neutron density distributions deduced from antiprotonic atoms. Phys. Rev. Lett. **87**, 082501 (2001)

62. E. Widmann, Low-energy antiprotons physics and the FLAIR facility. Phys. Scr. **T166**, 014074 (2015)

63. W. Oelert, The ELENA project at CERN. Acta Phys. Pol. B **46**(1), 181 (2015)

64. E. Kugler, D. Fiander, B. Johnson, H. Haas, A. Przewloka, H. Ravn, D. Simon, K. Zimmer, The new CERN-ISOLDE on-line mass-separator facility at the PS-booster. Nucl. Instrum. Methods Phys. Res. Sect. B **70**(1), 41–49 (1992)

65. M.J.G. Borge, B. Jonson, ISOLDE past, present and future. J. Phys. G: Nucl. Part. Phys. **44**, 044011 (2017)

66. J. Carbonell, A. Corsi, F. Flavigny, H. De Gersem, G. Hupin, Y. Kubota, R. Lazauskas, S. Malbrunot, N. Marsic, W. F. O. Muller, S. Naimi, N. Nakatsuka, A. Obertelli, P. Paul, P. Pérez, E. C. Pollacco, M. Rosenbusch, R. Seki, T. Uesaka, F. Wienholtz, PUMA : antiprotons and radioactive nuclei. Memorandum INTC-M-018, CERN (2018)

67. E. Fermi, E. Teller, V. Weisskopf, The decay of negative mesotrons in matter. Phys. Rev. **71**, 314–315 (1947)

68. J.S. Cohen, Capture of antiprotons by some radioactive atoms and ions. Phys. Rev. A **69**, 022501 (2004)

69. K. Sakimoto, Cross sections for antiproton capture by helium ions. Phys. Rev. A **82**, 012501 (2010)

70. N.H. Kwong, J.D. Garcia, J.S. Cohen, Classical-quantal coupling in the capture of muons by hydrogen atoms. J. Phys. B: At. Mol. Opt. Phys. **22**, L633–L638 (1989)

71. J.S. Cohen, Capture of negative exotic particles by atoms, ions and molecules. Rep. Prog. Phys. **67**, 1769–1819 (2004)

72. R. Schmidt, F.J. Hartmann, T. von Egidy, T. Czosnyka, J. Iwanicki, J. Jastrzębski, M. Kisieliński, P. Lubiński, P. Napiorkowski, L. Pieńkowski, A. Trzcińska, J. Kulpa, R. Smolańczuk, S. Wycech, B. Kłos, K. Gulda, W. Kurcewicz, E. Widmann, Nucleon density of ^{172}Yb and ^{176}Yb at the nuclear periphery determined with antiprotonic x rays. Phys. Rev. C **58**, 3195–3204 (1998)

73. J.S. Cohen, Capture of negative muons and antiprotons by noble-gas atoms. Phys. Rev. A **65**, 052714 (2002)

74. J.S. Cohen, Multielectron effects in capture of antiprotons and muons by helium and neon. Phys. Rev. A **62**, 022512 (2000)

75. R. Callies, H. Daniel, F. Hartmann, W. Neumann, Detection of muonic Auger electron lines from silver. Phys. Lett. A **91**(9), 441–443 (1982)

76. R. Bacher, P. Blüm, D. Gotta, K. Heitlinger, M. Schneider, J. Missimer, L.M. Simons, K. Elsener, Degree of ionization in antiprotonic noble gases. Phys. Rev. A **38**, 4395–4404 (1988)

77. D. Gotta, K. Rashid, B. Fricke, P. Indelicato, L.M. Simons, X-ray transitions from antiprotonic noble gases. Eur. Phys. J. D **47**(1), 11–26 (2008)

78. M. Leon, R. Seki, Determination of the neutron halo from antiproton absorption. Phys. Lett. B **48**(3), 173–175 (1974)

79. J. Desclaux, Relativistic multiconfiguration Dirac-Fock package, Methods an Techniques in Computational Chemistry (1993)

80. T. Ishiwatari, G. Beer, A. Bragadireanu, M. Cargnelli, C. C. (Petrascu), J.-P. Egger, H. Fuhrmann, C. Guaraldo, P. Kienle, T. Koike, M. Iliescu, K. Itahashi, M. Iwasaki, B. Lauss, V. Lucherini, L. Ludhova, J. Marton, F. Mulhauser, T. Ponta, L. Schaller, R. Seki, D. Sirghi, F. Sirghi, P. Strasser, J. Zmeskal, Kaonic nitrogen x-ray transition yields in a gaseous target. Phys. Lett. B **593**(1), 48–54 (2004)

81. E. Friedman, A. Gal, J. Mareš, Antiproton-nucleus potentials from global fits to antiprotonic X-rays and radiochemical data. Nucl. Phys. A **761**(3), 283–295 (2005)

82. C. Dover, T. Gutsche, M. Maruyama, A. Faessler, The physics of nucleon-antinucleon annihilation. Prog. Part. Nucl. Phys. **29**, 87–173 (1992)

83. G. Ghesquière, An inclusive view on $\bar{p}p \to \pi$ at rest. In *Symposium on Antinucleon-Nucleon Interactions* (1974)

84. S. Orfanidis, V. Rittenberg, Nucleon-antinucleon annihilation into pions. Nucl. Phys. B **59**(2), 570–582 (1973)

85. D. Mancusi, S. Lo-Meo, N. Colonna, A. Boudard, M.A. Cortés-Giraldo, J. Cugnon, J.-C. David, S. Leray, J. Lerendegui-Marco, C. Massimi, V. Vlachoudis, On the role of secondary pions in spallation targets. Eur. Phys. J. A **53**, 80 (2017)

86. J. Cugnon, S. Wycech, J. Jastrzębski, P. Lubiński, Geometrical effects in antiproton annihilation on nuclei. Phys. Rev. C **63**, 027301 (2001)

87. S. Wycech, Nuclear structure studies with low energy $\bar{p}$. AIP Conf. Proc. **793**(1), 201–213 (2005)

88. M. Wada, Y. Yamazaki, Antiprotonic radioactive atom for nuclear structure studies. AIP Conf. Proc. **793**(1), 233–241 (2005)

89. Y. Kubota et al., *in preparation* (2022)

90. C.B. Dover, J. Richard, Elastic, charge exchange, and inelastic $\bar{p}$p cross sections in the optical model. Phys. Rev. C **21**(4), 1466 (1980)

91. M. Kohno, W. Weise, Proton-antiproton scattering and annihilation into two mesons. Nucl. Phys. A **454**(3–4), 429–452 (1986)

92. B. El-Bennich, M. Lacombe, B. Loiseau, S. Wycech, Paris n$\bar{n}$ potential constrained by recent antiprotonic-atom data and $\bar{n}$p total cross sections. Phys. Rev. C **79**(5), 054001 (2009)

93. L.-Y. Dai, J. Haidenbauer, U.-G. Meißner, Antinucleon-nucleon interaction at next-to-next-to-next-to-leading order in chiral effective field theory. J. High Energy Phys. **2017**(7), 1–48 (2017)

94. J. Carbonell, G. Ihle, J.M. Richard, Protonium annihilation in optical models. Zeitschr. für Phys. A Atomic Nuclei **334**(3), 329–341 (1989)

95. E. Ydrefors, J. Carbonell, Protonium annihilation densities in a unitary coupled channel model. Eur. Phys. J. A **2021**, 1 (2021)

96. R. Lazauskas, J. Carbonell, Testing nonlocal nucleon-nucleon interactions in four-nucleon systems. Phys. Rev. C **70**(4), 044002 (2004)

97. R. Lazauskas, Solution of the n-^{4}He elastic scattering problem using the faddeev-yakubovsky equations. Phys. Rev. C **97**(4), 044002 (2018)

98. R. Lazauskas, J. Carbonell, Antiproton-deuteron hydrogenic states in optical models. Phys. Lett. B **820**, 136573 (2021)

99. T.L. Trueman, Energy level shifts in atomic states of strongly-interacting particles. Nucl. Phys. **26**(1), 57–67 (1961)

100. J. Carbonell, J.-M. Richard, S. Wycech, On the relation between protonium level shifts and nucleon-antinucleon scattering amplitudes. Zeitschr. für Phys. A Hadrons Nuclei **343**(3), 325–329 (1992)

101. P. Navrátil, S. Quaglioni, G. Hupin, C. Romero-Redondo, A. Calci, Unified ab initio approaches to nuclear structure and reactions. Phys. Scr. **91**(5), 053002 (2016)

102. G. Hupin, J. Langhammer, P. Navrátil, S. Quaglioni, A. Calci, R. Roth, Ab initio many-body calculations of nucleon-4 he scattering with three-nucleon forces. Phys. Rev. C **88**(5), 054622 (2013)

103. G. Hupin, S. Quaglioni, P. Navrátil, Unified description of ^{6}Li structure and deuterium-^{4}He dynamics with chiral two-and three-nucleon forces. Phys. Rev. Lett. **114**(21), 212502 (2015)

104. A. Calci, P. Navrátil, R. Roth, J. Dohet-Eraly, S. Quaglioni, G. Hupin, Can ab initio theory explain the phenomenon of parity inversion in ^{11}Be?? Phys. Rev. Lett. **117**(24), 242501 (2016)

105. K. Kravvaris, S. Quaglioni, G. Hupin, P. Navratil, Ab initio framework for nuclear scattering and reactions induced by light projectiles. Phys. Rev. C: Lett. (2020). arXiv:2012.00228

106. C. Romero-Redondo, S. Quaglioni, P. Navrátil, G. Hupin, How many-body correlations and α clustering shape ^{6}He. Phys. Rev. Lett. **117**(22), 222501 (2016)

107. 3-D QUENCH Module of OPERA 3D documentation by Vector Field Limited in the United Kingdom (2020)

108. C. H. Storry, M. Aggarwal, A. Akbari, F. Al-Rahawi, C. Amole, A. Batrachenko, A. Bebko, A. Carew, M. Chalfin, D. Comeau, G. Gabrielse, F. Garofalo, M. C. George, F. Goldenbaum, D. Grzonka, N. Guise, Y. Gura, T. Hänsch, E. A. Hessels, D. Kolbe, S. Kotlhammer, I. Kuljanishvili, P. Larochelle, D. Lesage, D. Levitt, K. Lewis, B. Lishak, F. Markert, F. Nillius, W. Oelert, S. Patel, P. Popescu, M. Scheid, T. Sefzick, A. Speck, D. Swierad, J. Walz, M. Weel, J. Wrubel, and Z. Zang, ATRAP antihydrogen experiments. Phys. stat. sol. **4**, 3437 (2007)

109. ALPHA Collaboration (2020), http://alpha.web.cern.ch

110. AEgIS Collaboration (2020), https://aegis.web.cern.ch/aegis

111. X.-P. Huang, F. Anderegg, E.M. Hollmann, C.F. Driscoll, T.M. O'Neil, Steady-state confinement of non-neutral plasmas by rotating electric fields. Phys. Rev. Lett. **78**, 875–878 (1997)

112. S. Aghion, C. Amsler, G. Bonomi, R.S. Brusa, M. Caccia, R. Caravita, F. Castelli, G. Cerchiari, D. Comparat, G. Consolati, A. Demetrio, L. Di Noto, M. Doser, C. Evans, M. Fanì, R. Ferragut, J. Fesel, A. Fontana, S. Gerber, M. Giammarchi, A. Gligorova, F. Guatieri, S. Haider, A. Hinterberger, H. Holmestad, A. Kellerbauer, O. Khalidova, D. Krasnický, V. Lagomarsino, P. Lansonneur, P. Lebrun, C. Malbrunot, S. Mariazzi, J. Marton, V. Matveev, Z. Mazzotta, S.R. Müller, G. Nebbia, P. Nedelec, M. Oberthaler, N. Pacifico, D. Pagano, L. Penasa, V. Petracek, F. Prelz, M. Prevedelli, B. Rienaecker, J. Robert, O.M. Røhne, A. Rotondi, H. Sandaker, R. Santoro, L. Smestad, F. Sorrentino, G. Testera, I.C. Tietje, E. Widmann, P. Yzombard, C. Zimmer, J. Zmeskal, N. Zurlo, M. Antonello, Compression of a mixed antiproton and electron non-neutral plasma to high densities. Eur. Phys. J. D **72**, 76 (2018)

113. G. Testera, S. Aghion, C. Amsler, A. Ariga, T. Ariga, A. Belov, G. Bonomi, P. Braunig, J. Bremer, R. Brusa, L. Cabaret, M. Caccia, R. Caravita, F. Castelli, G. Cerchiari, K. Chlouba, S. Cialdi, D. Comparat, G. Consolati, S. Curreli, A. Demetrio, H. Derking, L.D. Noto, M. Doser, A. Dudarev, A. Ereditato, R. Ferragut, A. Fontana, S. Gerber, M. Giammarchi, A. Gligorova, S. Gninenko, S. Haider, S. Hogan, H. Holmestad, T. Huse, E.J. Jordan, J. Kawada, A. Kellerbauer, M. Kimura, D. Krasnický, V. Lagomarsino, S. Lehner, C. Malbrunot, S. Mariazzi, V. Matveev, Z. Mazzotta, G. Nebbia, P. Nedelec, M. Oberthaler, N. Pacifico, L. Penasa, V. Petracek, C. Pistillo, F. Prelz, M. Prevedelli, L. Ravelli, C. Riccardi, O.M. Røhne, S. Rosenberger, A. Rotondi, H. Sandaker, R. Santoro, P. Scampoli, L. Semeria, M. Simon, M. Spacek, J. Storey, I.M. Strojek, M. Subieta, E. Widmann, P. Yzombard, S. Zavatarelli, J. Zmeskal, (AEgIS Collaboration), The AEgIS experiment. Hyperfine Interact. **233**, 13–20 (2015)

114. T. Mohamed, Compression features of high density electron plasma in a long harmonic trap using a rotating wall technique. Phys. Lett. A **382**, 2459–2463 (2018)

115. F. Anderegg, E.M. Hollmann, C.F. Driscoll, Rotating field confinement of pure electron plasmas using trivelpiece-gould modes. Phys. Rev. Lett. **81**, 4875–4878 (1998)

116. F. Anderegg, *Trapped Charged Particles*. World Scientific (2016)

117. J.M.A. Repp, The setup of the high-precision Penning trap mass spectrometer PENTATRAP and first production studies of highly charged ions. PhD thesis, Ruprecht-Karls-Universität Heidelberg (2012)

118. Z. Andelkovic, Setup of a Penning trap for precision laser spectroscopy at HITRAP. PhD thesis, Johannes Gutenberg-Universität Mainz (2012)

119. C.S. Weimer, J.J. Bollinger, F.L. Moore, D.J. Wineland, Electrostatic modes as a diagnostic in Penning-trap experiments. Phys. Rev. A **49**, 3842–3853 (1994)

120. G.W. Hart, The effect of a tilted magnetic field on the equilibrium of a pure electron plasma. Phys. Fluids B **3**(11), 2987–2993 (1991)

121. F. Ziegler, D. Beck, H. Brand, H. Hahn, G. Marx, L. Schweikhard, A new pulse-pattern generator based on Labview FPGA. Nucl. Instrum. Methods Phys. Res. Sect. A **679**, 1–6 (2012)

122. D. Neidherr, H. Brand (2020), https://git.gsi.de/EE-LV/CSPP/CSPP

123. D. Neidherr, H. Brand (2020), https://wiki.gsi.de/cgi-bin/view/CSframework/WebHome

124. J. Dilling, D. Ackermann, J. Bernard, F.P. Hessberger, S. Hofmann, W. Hornung, H.J. Kluge, E. Lamour, M. Maier, R. Mann, G. Marx, R.B. Moore, G. Münzenberg, W. Quint, D. Rodriguez, M. Schädel, J. Schönfelder, G. Sikler, C. Toader, L. Vermeeren, C. Weber, G. Bollen, O. Engels, D. Habs, P. Thirolf, H. Backe, A. Dretzke, W. Lauth, W. Ludolphs, M. Sewtz, The SHIPTRAP project: a capture and storage facility at GSI for heavy radionuclides from SHIP. Hyperfine Interact. **127**, 491–496 (2000)

125. M. Mukherjee, D. Beck, K. Blaum, G. Bollen, P. Delahaye, J. Dilling, S. George, C. Guénaut, F. Herfurth, A. Herlert, A. Kellerbauer, H.J. Kluge, U. Köster, D. Lunney, S. Schwarz, L. Schweikhard, C. Yazidjian, Mass measurements and evaluation around A = 22. Eur. Phys. J. A **35**(1), 31–37 (2008)

126. R. Ringle, G. Bollen, A. Prinke, J. Savory, P. Schury, S. Schwarz, T. Sun, The LEBIT 9.4T penning trap mass spectrometer. Nucl. Instr. Methods Phys. Res. Sect. A: Accelerat. Spectrometers Detect. Assoc. Equipm. **604**(3), 536–547 (2009)

127. U. Bergner, S. Wolfgramm, S. Gottschall, C. Worsch, M. Flämmich, Vakuumkomponenten für uhv und xhv aus aluminium. Vak. Forsch. Prax. **27**(2), 26–29 (2015)

128. A.L. Woodcraft, Predicting the thermal conductivity of aluminium alloys in the cryogenic to room temperature range. Cryogenics **45**(6), 421–431 (2005)

129. K.-P. Weiss, S. Westenfelder, A. Jung, N. Bagrets, W. Fietz, Determination of mechanical and thermal properties of electrical insulation material at 4.2 K. AIP Conf. Proc. **1435**(1), 148–155 (2012)

130. P. Micke, J. Stark, S.A. King, T. Leopold, T. Pfeifer, L. Schmöger, M. Schwarz, L.J. Spieß, P.O. Schmidt, J.R. Crespo López-Urrutia, Closed-cycle, low-vibration 4 K cryostat for ion traps and other applications. Rev. Sci. Instrum. **90**(6), 065104 (2019)

131. S. Ulmer, First observation of spin flips with a single proton stored in a cryogenic Penning Trap. PhD thesis, Ruperto-Carola University of Heidelberg (2011)

132. R.A. Nevshupa, E. Roman, J.L. de Segovia, Origin of hydrogen desorption during friction of stainless steel by alumina in ultrahigh vacuum. J. Vacuum Sci. Technol. A **26**(5), 1218–1223 (2008)

133. M. Amoretti, C. Amsler, G. Bonomi, A. Bouchta, P.D. Bowe, C. Carraro, C.L. Cesar, M. Charlton, M. Doser, V. Filippini, A. Fontana, M.C. Fujiwara, R. Funakoshi, P. Genova, J.S. Hangst, R.S. Hayano, L.V. Jørgensen, V. Lagomarsino, R. Landua, D. Lindelöf, E.L. Rizzini, M. Macrí, N. Madsen, G. Manuzio, P. Montagna, H. Pruys, C. Regenfus, A. Rotondi, G. Testera, A. Variola, D.P. van der Werf, Positron plasma diagnostics and temperature control for antihydrogen production. Phys. Rev. Lett. **91**, 055001 (2003)

134. M. Amoretti, G. Bonomi, A. Bouchta, P. D. Bowe, C. Carraro, C. L. Cesar, M. Charlton, M. Doser, A. Fontana, M. C. Fujiwara, R. Funakoshi, P. Genova, J. S. Hangst, R. S. Hayano, L. V. Jørgensen, L. V.rgensen, V. Lagomarsino, R. Landua, E. L. Rizzini, M. Macrí, M., N. Madsen, G. Manuzio, G. Testera, A. Variola, D. P. van der Werf, Complete nondestructive diagnostic of non-neutral plasmas based on the detection of electrostatic modes. Phys. Plasmas **10**(8), 3056–3064 (2003)

135. A. Speck, G. Gabrielse, P. Larochelle, D.L. Sage, B. Levitt, W. Kolthammer, R. McConnell, J. Wrubel, D. Grzonka, W. Oelert, T. Sefzick, Z. Zhang, D. Comeau, M. George, E. Hessels, C. Storry, M. Weel, J. Walz, Density and geometry of single component plasmas. Phys. Lett. B **650**(2), 119–123 (2007)

136. M. Amoretti, C. Amsler, G. Bonomi, A. Bouchta, P. Bowe, C. Carraro, M. Charlton, M. Collier, M. Doser, V. Filippini, K. Fine, A. Fontana, M. Fujiwara, R. Funakoshi, P. Genova, A. Glauser, D. Grögler, J. Hangst, R. Hayano, H. Higaki, M. Holzscheiter, W. Joffrain, L. Jørgensen, V. Lagomarsino, R. Landua, C.L. Cesar, D. Lindelöf, E. Lodi-Rizzini, M. Macri, N. Madsen, D. Manuzio, G. Manuzio, M. Marchesotti, P. Montagna, H. Pruys, C. Regenfus, P. Riedler, J. Rochet, A. Rotondi, G. Rouleau, G. Testera, D.P. van der Werf, A. Variola, T. Watson, T. Yamazaki, Y. Yamazaki, The ATHENA antihydrogen apparatus. Nucl. Instrum. Methods Phys. Res. Sect. A **518**(3), 679–711 (2004)

137. P. Richerme, Trapped antihydrogen in its ground state. PhD thesis, Harvard University, Cambridge, Massachusetts, USA (2012)

138. D.H.E. Dubin, Theory of electrostatic fluid modes in a cold spheroidal non-neutral plasma. Phys. Rev. Lett. **66**, 2076–2079 (1991)

139. H. Higaki, A. Mohri, Wall and temperature effects on electrostatic oscillations of spheroidal non-neutral electron plasmas in the multi-ring electrode trap. Jpn. J. Appl. Phys. **36**, 5300–5305 (1997)

140. A.V. Crewe, D.N. Eggenberger, J. Wall, L.M. Welter, Electron gun using a field emission source. Rev. Sci. Instrum. **39**(4), 576–583 (1968)

141. M. Redshaw, A.L. Benjamin, G. Bollen, R. Ferrer, D.L. Lincoln, R. Ringle, S. Schwarz, A.A. Valverde, Fabrication and characterization of field emission points for ion production in Penning trap applications. Int. J. Mass Spectrom. **379**, 187–193 (2015)

142. J. Fischer et al., in preparation (2021)

143. A.W. Trivelpiece, R.W. Gould, Space charge waves in cylindrical plasma columns. J. Appl. Phys. **30**(11), 1784–1793 (1959)

144. E.M. Hollmann, F. Anderegg, C.F. Driscoll, Confinement and manipulation of non-neutral plasmas using rotating wall electric fields. Phys. Plasmas **7**(7), 2776–2789 (2000)

145. R.G. Greaves, C.M. Surko, Inward transport and compression of a positron plasma by a rotating electric field. Phys. Rev. Lett. **85**, 1883–1886 (2000)

146. J.R. Danielson, C.M. Surko, Torque-balanced high-density steady states of single-component plasmas. Phys. Rev. Lett. **94**, 035001 (2005)

147. G.B. Andresen, W. Bertsche, P.D. Bowe, C.C. Bray, E. Butler, C.L. Cesar, S. Chapman, M. Charlton, J. Fajans, M.C. Fujiwara, R. Funakoshi, D.R. Gill, J.S. Hangst, W.N. Hardy, R.S. Hayano, M.E. Hayden, R. Hydomako, M.J. Jenkins, L.V. Jørgensen, L. Kurchaninov, R. Lambo, N. Madsen, P. Nolan, K. Olchanski, A. Olin, A. Povilus, P. Pusa, F. Robicheaux, E. Sarid, S. Seif El Nasr, D.M. Silveira, J.W. Storey, R.I. Thompson, D.P. van der Werf, J.S. Wurtele, Y. Yamazaki, Compression of antiproton clouds for antihydrogen trapping. Phys. Rev. Lett. **100**, 203401 (2008)

148. G. Gabrielse, W.S. Kolthammer, R. McConnell, P. Richerme, J. Wrubel, R. Kalra, E. Novitski, D. Grzonka, W. Oelert, T. Sefzick, M. Zielinski, J.S. Borbely, D. Fitzakerley, M.C. George, E.A. Hessels, C.H. Storry, M. Weel, A. Müllers, J. Walz, A. Speck, Centrifugal separation of antiprotons and electrons. Phys. Rev. Lett. **105**, 213002 (2010)

149. C. Smorra, A. Mooser, K. Franke, H. Nagahama, G. Schneider, T. Higuchi, S. Gorp, K. Blaum, Y. Matsuda, W. Quint, J. Walz, Y. Yamazaki, S. Ulmer, A reservoir trap for antiprotons. Int. J. Mass Spectrom. **389**, 10–13 (2015)

150. G. Gabrielse, J. Estrada, J. Tan, P. Yesley, N. Bowden, P. Oxley, T. Roach, C. Storry, M. Wessels, J. Tan, D. Grzonka, W. Oelert, G. Schepers, T. Sefzick, W. Breunlich, M. Cargnelli, H. Fuhrmann, R. King, R. Ursin, J. Zmeskal, H. Kalinowsky, C. Wesdorp, J. Walz, K. Eikema, T. Hänsch, First positron cooling of antiprotons. Phys. Lett. B **507**(1), 1–6 (2001)

151. D.S. Hall, G. Gabrielse, Electron cooling of protons in a nested penning trap. Phys. Rev. Lett. **77**, 1962–1965 (1996)

152. J.H. Malmberg, J.S. deGrassie, Properties of nonneutral plasma. Phys. Rev. Lett. **35**, 577–580 (1975)

153. G.-Z. Li, S. Guan, A.G. Marshall, Sympathetic cooling of trapped negative ions by self-cooled electrons in a Fourier transform ion cyclotron resonance mass spectrometer. J. Am. Soc. Mass Spectrom. **8**(8), 793–800 (1997)

154. J. Bernard, J. Alonso, T. Beier, M. Block, S. Djekić, H.-J. Kluge, C. Kozhuharov, W. Quint, S. Stahl, T. Valenzuela, J. Verdú, M. Vogel, G. Werth, Electron and positron cooling of highly charged ions in a cooler penning trap. Nucl. Instrum. Methods Phys. Res. Sect. A Acceler. Spectrom. Detect. Assoc. Equip. **532**(1), 224–228 (2004) (International Workshop on Beam Cooling and Related Topics)

155. M. Bohman, A. Mooser, G. Schneider, N. Schön, M. Wiesinger, J. Harrington, T. Higuchi, H. Nagahama, C. Smorra, S. Sellner, K. Blaum, Y. Matsuda, W. Quint, J. Walz, S. Ulmer, Sympathetic cooling of protons and antiprotons with a common endcap penning trap. J. Mod. Opt. **65**(5–6), 568–576 (2018)

156. G. Cierchiari, Laser spectroscopy of La$^-$ and anion trapping with a view to laser cooling. PhD thesis, University of Heidelberg (2018)

157. G.B. Andresen, M.D. Ashkezari, M. Baquero-Ruiz, W. Bertsche, P.D. Bowe, E. Butler, P.T. Carpenter, C.L. Cesar, S. Chapman, M. Charlton, J. Fajans, T. Friesen, M.C. Fujiwara, D.R. Gill, J.S. Hangst, W.N. Hardy, M.E. Hayden, A.J. Humphries, J.L. Hurt, R. Hydomako, S. Jonsell, N. Madsen, S. Menary, P. Nolan, K. Olchanski, A. Olin, A. Povilus, P. Pusa, F. Robicheaux, E. Sarid, D.M. Silveira, C. So, J.W. Storey, R.I. Thompson, D.P. van der Werf, J.S. Wurtele, Y. Yamazaki, Autoresonant excitation of antiproton plasmas. Phys. Rev. Lett. **106**, 025002 (2011)

158. Y. Hahn, Electron–ion recombination processes—an overview. Rep. Prog. Phys. **60**, 691–759 (1997)

159. G. Zwicknagel, Electron cooling of highly charged ions in Penning traps. AIP Conf. Proc. **862**(1), 281–291 (2006)

160. G. Gabrielse, S. Rolston, L. Haarsma, W. Kells, Antihydrogen production using trapped plasmas. Phys. Lett. A **129**(1), 38–42 (1988)

161. H. Himura, Recent experiments with lithium ion and electron plasmas in the BX-U linear trap. AIP Conf. Proc. **1928**(1), 020005 (2018)

162. G.B. Andresen, M.D. Ashkezari, M. Baquero-Ruiz, W. Bertsche, P.D. Bowe, E. Butler, C.L. Cesar, S. Chapman, M. Charlton, A. Deller, S. Eriksson, J. Fajans, T. Friesen, M.C. Fujiwara, D.R. Gill, A. Gutierrez, J.S. Hangst, W.N. Hardy, M.E. Hayden, A.J. Humphries, R. Hydomako, S. Jonsell, N. Madsen, S. Menary, P. Nolan, A. Olin, A. Povilus, P. Pusa, F. Robicheaux, E. Sarid, D.M. Silveira, C. So, J.W. Storey, R.I. Thompson, D.P. van der Werf, J.S. Wurtele, Y. Yamazaki, Centrifugal separation and equilibration dynamics in an electron-antiproton plasma. Phys. Rev. Lett. **106**, 145001 (2011)

163. L. Suess, Y. Liu, F.B. Dunning, Selective removal of electrons from a penning trap for negative ion autodetachment studies. Rev. Sci. Instrum. **76**(2), 026116 (2005)

164. H. Imajo, K. Hayasaka, R. Ohmukai, U. Tanaka, M. Watanabe, S. Urabe, Spatial separation of ion clouds between sympathetically laser-cooled Cd$^+$ -ion isotopes in a Penning trap. Phys. Rev. A **55**, 1276–1280 (1997)

165. M. Amoretti, C. Canali, C. Carraro, V. Lagomarsino, A. Odino, G. Testera, S. Zavatarelli, Centrifugal separation of ions and an oppositely charged non-neutral plasma. Phys. Plasmas **13**(1), 012308 (2006)

166. S. Agostinelli et al., GEANT4—a simulation toolkit. Nucl. Instrum. Meth. **506**(3), 250–303 (2003)

167. R. Brun, F. Rademakers, Root—an object oriented data analysis framework, in *Proceedings AIHENP'96 Workshop Lausanne, Sep. 1996*, Nucl. Inst. & Meth. in Phys. Res. A **389**, 81–86 (1997)

168. C. Ghesquiere, An inclusive view on $p\bar{p} \to n\pi$ at rest (Symposium on Antinucleon-Nucleon Interactions, CERN, 1974)

169. S. Biagi, Monte carlo simulation of electron drift and diffusion in counting gases under the influence of electric and magnetic fields. Nucl. Instrum. Meth. Res. Sect. A: Accel. Spectr. Detect. Assoc. Equip. **421**(1), 234–240 (1999)

170. A. Obertelli et al., MINOS: a vertex tracker coupled to a thick liquid-hydrogen target for in-beam spectroscopy of exotic nuclei. Eur. Phys. J. A **50**, 8 (2014)

171. C. Santamaria, A. Obertelli, S. Ota, M. Sasano, E. Takada, L. Audirac, H. Baba, D. Calvet, F. Château, A. Corsi, A. Delbart, P. Doornenbal, A. Giganon, A. Gillibert, Y. Kondo, Y. Kubota, C. Lahonde-Hamdoun, V. Lapoux, D. Leboeuf, C. Lee, H. Liu, M. Matsushita, T. Motobayashi, M. Niikura, M. Kurata-Nishimura, H. Otsu, A. Peyaud, E. Pollacco, G. Prono, H. Tokieda, T. Uesaka, J. Zenihiro, Tracking with the MINOS time projection chamber. Nucl. Instrum. Methods Phys. Res. Sect. A **905**, 138–148 (2018)

172. F. James, M. Winkler, MINUIT User's Guide, *INSPIRE* (2004)

173. C. Geuzaine, J.-F. Remacle, GMSH: a 3-D finite element mesh generator with built-in pre- and post-processing facilities. Int. J. Numer. Meth. Eng. **79**(11), 1309–1331 (2009)

174. P. Raback, Elmer finite element software homepage (2020)

175. H. Schindler, Garfield++ (2020)

176. C. Hagmann, D. Lange, D. Wright, Cosmic-ray shower generator (CRY) for Monte Carlo transport codes, in *2007 IEEE Nuclear Science Symposium Conference Record*, vol. 2, pp. 1143–1146 (2007)

177. Y. Giomataris, P. Rebourgeard, J. Robert, G. Charpak, MICROMEGAS: a high-granularity position-sensitive gaseous detector for high particle-flux environments. Nucl. Instrum. Meth. Phys. Res. Sect. A Accel. Spectrometers, Detect. Assoc. Equip. **376**(1), 29–35 (1996)

178. M.S. Dixit, J. Dubeau, J.P. Martin, K. Sachs, Position sensing from charge dispersion in micro-pattern gas detectors with a resistive anode. Nucl. Instrum. Meth. Phys. Res. Sect. A Accel. Spectrometers Detect. Assoc. Equip. **518**(3), 721–727 (2004)

179. E. Dietz-Laursonn, T. Hebbeker, A. Künsken, M. Merschmeyer, S. Nieswand, T. Niggemann, GODDeSS: a GEANT4 extension for easy modelling of optical detector components. J. Instrum. **12**, P04026–P04026 (2017)

180. P. Baron, E. Delagnes, *STAGE, a Front End ASIC for Active Time Projection Chamber Data Sheet*. Irfu/CEA Saclay (2019)

181. P. Baron et al., After, an asic for the readout of the large T2K time projection chambers, in *2007 IEEE Nuclear Science Symposium Conference Record*, vol. 55, pp. 1865–1872 (2008)

182. S. Anvar et al., AGET, the GET front-end ASIC, for the readout of the time projection chambers used in nuclear physic experiments, in *2011 IEEE Nuclear Science Symposium Conference Record*, pp. 745–749 (2011)

183. D. Calvet, Trigger & data concentrator module reference manual, *CEA Saclay* (2019)

184. Enclustra, Mercury ZX1 SoC module user manual, *Enclustra, FPGA solutions* (2018)

185. D. Calvet, A versatile readout system for small to medium scale gaseous and silicon detectors. IEEE Trans. Nucl. Sci. **61**, 675–682 (2014)

186. TRB website, (2020), http://trb.gsi.de. Accessed 12 Dec 2020

187. C. Ugur, W. Koening, J. Michel, M. Palka, M. Traxler, Field programmable gate array based data digitisation with commercial elements. J. Instrum. **8**, C01035–C01035 (2013)

188. C. Ugur, S. Linev, J. Michel, T. Schweitzer, M. Traxler, A novel approach for pulse width measurements with a high precision (8 ps RMS) TDC in an FPGA. J. Instrum. **11**, C01046–C01046 (2016)

189. C. Ugur, E. Bayer, N. Kurz, M. Traxler, A 16 channel high resolution ($\leq$11 ps RMS) time-to-digital converter in a field programmable gate array. J. Instrum. **7**, C02004–C02004 (2012)

190. M. Traxler, E. Bayer, M. Kajetanowicz, G. Korcyl, L. Maier, J. Michel, M. Palka, C. Ugur, A compact system for high precision time measurements ($\leq$ 14 ps RMS) and integrated data acquisition for a large number of channels. J. Instrum. **6**, C12004–C12004 (2011)

191. J. Michel, M. Böhmer, M. Kajetanowicz, G. Korcyl, L. Maier, M. Palka, J. Stroth, A. Tarantola, M. Traxler, C. Ugur, S. Yurevich, The upgraded HADES trigger and data acquisition system. J. Instrum. **6**, C12056–C12056 (2011)

192. BASE Collaboration (2020), http://base.web.cern.ch

193. C.H. Tseng, G. Gabrielse, Portable trap carries particles 5000 kilometers. Hyperfine Interact. **76**, 381–386 (1993)

194. L. Bracci, G. Fiorentini, O. Pitzurra, Protonium formation in flight. Phys. Lett. B (Netherl.) **85**, 2–3 (1979)

195. X. Fei, in *Trapping Low Energy in an Ion Trap*. PhD thesis, Harvard University (1990)

196. E. Butler, in *Antihydrogen formation, dynamics and trapping*. PhD thesis, Swansea University (2011)

197. C. Benvenuti, Extreme vacua: achievements and expectations. Phys. Scr. **T22**, 48–54 (1988)

198. R. Salemme, V. Baglin, G. Bregliozzi, P. Chiggiato, in *Vacuum performance of amorphous carbon coating at cryogenic temperature with presence of proton beams*, 05 (2016)

199. F. Chill, S. Wilfert, L. Bozyk, Cryopumping of hydrogen on stainless steel in the temperature range between 7 and 18 K. J. Vacuum Sci. Technol. A **2019**, 37 (2019)

200. P.A. Redhead, J.P. Hobson, E.V. Kornelsen, *The Physical Basis of Ultrahigh Vacuum*, 1st edn. (AIP-Press, New York, 1993)

201. K. Jousten, *Handbook of Vacuum Technology* (Wiley-VCH, Berlin, 2016)

202. H. Freundlich, *Kapillarchemie (Leipizig)*, vol. I (1930)

203. S. Brunauer, P.H. Emmett, E. Teller, Adsorption of gases in multimolecular layers. Am. Chem. Soc. **60**, 309–319 (1938)

204. D.M. Young, A.D. Crowell, *Physical Adsorption of Gases* (Butterworths, London, 1962)

205. M.M. Dubinin, Contemporary state of the theory of volume filling of micropores of adsorbents in the adsorption of gases and vapors on carbon adsorbents. Russ. J. Phys. Chem. **39**, 487 (1965)

206. M. Dubinin, Adsorption in micropores. J. Colloid Interface Sci. **23**(4), 487–499 (1967)

207. M.M. Dubinin, L.V. Radushkevich, Equation of the characteristic curve of activated charcoal. Proc. USSR Acad. Sci. **55**, 327 (1947)

208. M.G. Kaganer, A method for determining the specific surface from the adsorption of gases in the monomolecular region. Proc. Acad. Sci. USSR **116**, 603 (1957)

209. M. Polanyi, Causes of forces of adsorption. Z. Electrochem. **26**, 370 (1920)

210. R.A. Haefer, *Cryopumping: Theory and Practice (Monographs on Cryogenics, 4)* (Oxford University Press, Oxford, 1989)

211. E. Wallén, Adsorption isotherms of He and H_2 at liquid He temperatures. J. Vacuum Sci. Technol. A **15**(2), 265–274 (1997)

212. CERN, in *Basics and applications of cryopumps*, CAS - CERN Accelerator School and ALBA Synchrotron Light Facility: Course on Vacuum in Accelerators (2007)

213. A. Güntherschulze, H. Betz, H. Kleinwächter, Die diffusion von wasserstoff und deuterium durch eisen. Z. Phys. **111**, 657–679 (1939)

214. K. Kiuchi, R. McLellan, The solubility and diffusivity of hydrogen in well-annealed and deformed iron. Acta Metall. **31**(7), 961–984 (1983)

215. COMSOL Multiphysics: a finite element analysis, solver and multiphysics simulation software developed by COMSOL Inc (2020)

216. COMSOL Multiphysics: model low-pressure gas flow in vacuum systems with the molecular flow module (2020), https://www.comsol.com/molecular-flow-module

217. COMSOL Multiphysics user manual, included in the software (2020)

218. F. Celestini, F. Mortessagne, Cosine law at the atomic scale: toward realistic simulations of Knudsen diffusion. Phys. Rev. E Stat. Nonlinear Soft Matter Phys. **77**, 021202 (2008)

219. P. Ossipov, The angular coefficient method for calculating the stationary molecular gas flow for arbitrary reflection law. Vacuum **48**(5), 409–412 (1997)

220. J.N. Chubb, L. Gowland, I.E. Pollard, Condensation pumping of hydrogen and deuterium on to liquid-helium-cooled surfaces. J. Phys. D Appl. Phys. **1**(3), 361–370 (1968)

221. P. Chiggiato, Materials and properties iv - outgassing. CERN Accelerator School 2017 (2017)

222. C. Benvenuti, R. Calder, The desorption of condensed hydrogen from various substrates by infrared thermal radiation. Phys. Lett. A **35**(4), 291–292 (1971)

223. A. Husson, in *Deceleration of antiprotons from CERN's ELENA synchrotron and transport of antimatter beams through the GBAR experiment*. PhD thesis, CSNSM, Université de Paris-Sud, 2018. Thèse de doctorat dirigée par Lunney, David Physique Paris Sud-Paris Saclay (2018)

224. D. Lunney, C. Bachelet, C. Guénaut, S. Henry, M. Sewtz, COLETTE: A linear Paul-trap beam cooler for the on-line mass spectrometer mistral. Nucl. Instrum. Methods Phys. Res. Sect. A **598**(2), 379–387 (2009)

225. F. Herfurth et al., A Linear radiofrequency ion trap for accumulation, bunching, and emittance improvement of radioactive ion beams. Nucl. Instrum. Meth. **A469**, 254–275 (2001)

226. R. Wolf, F. Wienholtz, D. Atanasov, D. Beck, K. Blaum, C. Borgmann, F. Herfurth, M. Kowalska, S. Kreim, Y.A. Litvinov, D. Lunney, V. Manea, D. Neidherr, M. Rosenbusch, L. Schweikhard, J. Stanja, K. Zuber, ISOLTRAP's multi-reflection time-of-flight mass separator/spectrometer. Int. J. Mass Spectrometry **349-350**, 123–133 (2013) (100 years of Mass Spectrometry)

227. S. Sels, P. Fischer, H. Heylen, V. Lagaki, S. Lechner, F.M. Maier, P. Plattner, M. Rosenbusch, F. Wienholtz, R.N. Wolf, W. Nörtershäuser, L. Schweikhard, S. Malbrunot-Ettenauer, First steps in the development of the multi ion reflection apparatus for collinear laser spectroscopy. Nucl. Instrum. Methods Phys. Res. B **463**, 3010 (2020)

228. E. Mané, J. Billowes, K. Blaum, P. Campbell, B. Cheal, P. Delahaye, K.T. Flanagan, D.H. Forest, H. Franberg, C. Geppert, T. Giles, A. Jokinen, M. Kowalska, R. Neugart, G. Neyens, W. Nörtershäuser, I. Podadera, G. Tungate, P. Vingerhoets, D.T. Yordanov, An ion cooler-buncher for high-sensitivity collinear laser spectroscopy at ISOLDE. Eur. Phys. J. A **42**, 503–507 (2009)

229. F. Herfurth, J. Dilling, A. Kellerbauer, G. Bollen, S. Henry, H.-J. Kluge, E. Lamour, D. Lunney, R. Moore, C. Scheidenberger, S. Schwarz, G. Sikler, J. Szerypo, A linear radiofrequency ion trap for accumulation, bunching, and emittance improvement of radioactive ion beams. Nucl. Instrum. Methods Phys. Res. Sect. A **469**(2), 254–275 (2001)

230. T. Aumann, W. Bartmann, A. Bouvard, O. Boine-Frankenheim, A. Broche, F. Butin, D. Calvet, J. Carbonell, P. Chiggiatto, H. D. Gersem, R. D. Oliveira, T. Dobers, F. Ehm, J. F. Somoza, J. Fischer, M. Fraser, E. Friedrich, J.-L. Grenard, G. Hupin, K. Johnston, Y. Kubota, M. Gomez-Ramos, P. Indelicato, R. Lazauskas, S. Malbrunot-Ettenauer, N. Marsic, W. Müller, S. Naimi, N. Nakatsuka, R. Necca, G. Neyens, A. Obertelli, Y. Ono, S. Pasinelli, N. Paul, E. C. Pollacco, D. Rossi, H. Scheit,

R. Seki, A. Schmidt, L. Schweikhard, S. Sels, E. Siesling, T. Uesaka, M. Wada, F. Wienholtz, S. Wycech, S. Zacarias, Experiment proposal for PUMA: antiprotons and radioactive nuclei (2019)

231. Molflow+: A test-particle Monte-Carlo simulator for ultra-high-vacuum systems developed at CERN (2019), https://molflow.web.cern.ch/. Accessed 1 Aug 2019

232. M. Saitoh, K. Shimura, T. Iwata, T. Momose, H. Ishimaru, Influence of vacuum gauges on outgassing rate measurements. J. Vacuum Sci. Technol. A **11**(5), 2816–2821 (1993)

233. J.A. Fedchak, J. Scherschligt, D. Barker, S. Eckel, A.P. Farrell, M. Sefa, Vacuum furnace for degassing stainless-steel vacuum components. J. Vacuum Sci. Technol. A Vacuum Surf. Films **36**, 5 (2018)

234. F.M. Maier, P. Fischer, H. Heylen, V. Lagaki, S. Lechner, P. Plattner, S. Sels, F. Wienholtz, W. Nörtershäuser, L. Schweikhard, S. Malbrunot-Ettenauer, Simulations of a proof-of-principle experiment for collinear laser spectroscopy within a multi-reflection time-of-flight device. Hyperfine Interact. **240**, 54 (2019)

235. I. Podadera, T. Fritioff, A. Jokinen, J.F. Kepinski, M. Lindroos, D. Lunney, F. Wenander, Preparation of cooled and bunched ion beams at ISOLDE-CERN. Eur. Phys. J. A Hadrons Nucl. **25**, 743–744 (2005)

236. S. Malbrunot-Ettenauer et al., in *Miracls the multi ion reflection apparatus for collinear laser spectroscopy of radionuclei* (2020). Addendum to the INTC, MIRACLS Collaboration

237. M.J.G. Borge, B. Jonson, ISOLDE past, present and future. J. Phys. G: Nucl. Part. Phys. **44**(4), 044011 (2017)

238. M.J.G. Borge, K. Blaum, Focus on exotic beams at ISOLDE: a laboratory portrait. J. Phys. G: Nucl. Part. Phys. **45**, 010301 (2017)

239. F. Wenander, J. Lettry, M. Lindroos, Transverse emittance investigation of the ISOLDE target-ion sources. Nucl. Instr. Methods Phys. Res. Sect. B Beam Interact. Mater. Atoms **204**, 261–266 (2003). (14th international conference on electromagnetic isotope separators and techniques related to their applications)

240. E. Kugler, The ISOLDE facility. Hyperfine Interact. **129**, 23–42 (2000)

241. B. Vosicki, T. Björnstad, L. Carraz, J. Heinemeier, H. Ravn, Intense beams of radioactive halogens produced by means of surface ionization. Nucl. Instrum. Methods Phys. Res. **186**(1), 307–313 (1981)

242. A.S. Schlachter, Formation of negative ions by charge transfer: He to Cl. AIP Conf. Proc. **111**(1), 300–332 (1984)

243. J.R. Beene, D.W. Bardayan, A.G. Uribarri, C.J. Gross, K.L. Jones, J.F. Liang, W. Nazarewicz, D.W. Stracener, B.A. Tatum, R.L. Varner, ISOL science at the holifield radioactive ion beam facility. J. Phys. G: Nucl. Part. Phys. **38**, 024002 (2011)

244. Y. Liu, D.W. Stracener, T. Stora, Production of negatively charged radioactive ion beams. New J. Phys. **19**, 085005 (2017)

245. S. Rothe, in *Preparation of negative ion beams for the determination of the electron affinity of polonium and astatine by laser photodetachment*, Tech. Rep. CERN-INTC-2013-037. INTC-I-148, CERN, Geneva. Topics: Atomic Physics and Physical Chemistry Requested beams: Po and At (2013)

246. S. Rothe, J. Champion, K. Chrysalidis, T. Day Goodacre, V. Fedosseev, N. Galland, D. Hanstorp, R. Heinke, U. Köster, T. Kron, Y. Liu, B. Marsh, G. Montavon, E. Renault, A. Ringwall-Moberg, R. Rossel, C. Seiffert, J. Sundberg, J. Welander, K. Wendt, in *Determination of the electron affinity of astatine and polonium by laser photodetachment*, Tech. Rep. CERN-INTC-2016-017. INTC-P-462, CERN, Geneva (2016)

247. D. Leimbach, J. Karls, Y. Guo, R. Ahmed, J. Ballof, L. Bengtsson, F. Boix Pamies, A. Borschevsky, K. Chrysalidis, E. Eliav, D. Fedorov, V. Fedosseev, O. Forstner, N. Galland, R. F. Garcia Ruiz, C. Granados, R. Heinke, K. Johnston, A. Koszorus, U. Köster, M. K. Kristiansson, Y. Liu, B. Marsh, P. Molkanov,

L. F. Pašteka, J. P. Ramos, E. Renault, M. Reponen, A. Ringvall-Moberg, R. E. Rossel, D. Studer, A. Vernon, J. Warbinek, J. Welander, K. Wendt, S. Wilkins, D. Hanstorp, S. Rothe, The electron affinity of astatine. Nature Commun. **11**, 3824 (2020)

248. S. Knauer, P. Fischer, G. Marx, M. Müller, M. Rosenbusch, B. Schabinger, L. Schweikhard, R. Wolf, A multi-reflection time-of-flight setup for the improvement and development of new methods and the study of atomic clusters. Int. J. Mass Spectrom. **446**, 116189 (2019)

249. P. Fischer, (2020). Private communication

250. P. Fischer, L. Schweikhard, Decay-rate power-law exponent as a link between dissociation energy and temperature. Phys. Rev. Res. **2**, 043177 (2020)

251. P. Fischer, S. Knauer, G. Marx, L. Schweikhard, In-depth study of in-trap high-resolution mass separation by transversal ion ejection from a multi-reflection time-of-flight device. Rev. Sci. Instrum. **89**(1), 015114 (2018)

252. P. Fischer, L. Schweikhard, Photofragmentation of Bi clusters in an electrostatic ion beam trap. Eur. Phys. J. D **73**, 105 (2019)

253. R. Catherall, W. Andreazza, M. Breitenfeldt, A. Dorsival, G.J. Focker, T.P. Gharsa, G.T. Jrenard, J.-L. Grenard, F. Locci, P. Martins, S. Marzari, J. Schipper, A. Shornikov, T. Stora, The ISOLDE facility. J. Phys. G: Nucl. Part. Phys. **44**, 094002 (2017)

254. ISOLDE collaboration, HIE-ISOLDE: the technical options, report CERN-2006-013, CERN (2006)

255. A. Herlert, The ISOLDE facility. Nucl. Phys. News **20**(4), 5–12 (2010)

256. R.N. Wolf, G. Marx, M. Rosenbusch, L. Schweikhard, Static-mirror ion capture and time focusing for electrostatic ion-beam traps and multi-reflection time-of-flight mass analyzers by use of an in-trap potential lift. Int. J. Mass Spectrom. **313**, 8–14 (2012)

257. S. Knauer, P. Fischer, G. Marx, B. Schabinger, L. Schweikhard, R. Wolf, Multi-reflection time-of-flight mass spectrometry with combined in-trap lift capture and mirror-switch ejection. Int. J. Mass Spectrom. **423**, 46–53 (2017)

258. MIRACLS collaboration, Benchmarking of a multi ion reflection apparatus for collinear laser spectroscopy of radionuclides, in *Letter of Intent to the ISOLDE and Neutron Time-of-Flight Committee* (2017)

259. E. Wallén, Adsorption isotherms of H_2 and mixtures of H_2, CH_4, CO, and CO_2 on copper plated stainless steel at 4.2 K. J. Vacuum Sci. Technol. A **14**(5), 2916–2929 (1996)

260. P. Kienle, Medium energy antiproton absorption, a tool to study neutron halo nuclei. Nucl. Instr. Methods Phys. Res. Sect. B Beam Interact. Mater. Atoms **214**, 191–195 (2004) (Low Energy Antiproton Physics (LEAP'03))